DOI: 10.14750/ME.2022.008

MIKOVINY SÁMUEL DOCTORAL SCHOOL OF EARTH SCIENCES

UNIVERSITY OF MISKOLC

Head of the Doctoral School
Prof. Dr. Péter Szűcs

COMPLEX ELECTROMAGNETIC RESEARCH INTO MAGNETOTELLURIC AND GPR METHODS

PHD THESIS

by

ENDRE NÁDASI

Scientific supervisor:

Dr. Endre Turai

Miskolc, 2021

HUNGARY

DOI: 10.14750/ME.2022.008

SUPERVISORS STATEMENT FOR PHD THESIS

Endre Nádasi's dissertation presents new scientific results in the development of two electromagnetic geophysical methods, Magnetotellurics and Ground-Penetrating Radar (GPR). The new scientific results are presented in seven thesis groups.

The first group of three subtheses presents the new results obtained by processing medium-depth magnetotelluric measurements in Cserehát, near Irota and Gadna, determining the spatial position of the Paleozoic basement and the vertical-horizontal extent of the good conducting geological formation.

The second group of theses presents the distribution of 1D and multidimensional geological structures in the research area, as well as the dominant fault direction in two subtheses, using correlation and cluster analysis.

The third group of theses presents the structural anisotropy at a depth of hundreds of km in the Western Superior province of Canada based on the results of magnetotellutic measurements.

Based on the result obtained by 3D inversion of 92 MT measurement points, the fourth thesis proves elongated conductive anomalies between 100 km and 300 km depth in the Western Superior region.

In the fifth group of theses, we can see the differences between dielectrics and lossy media in terms of propagation velocity, vertical resolution, wavelength, horizontal resolution, skin depth, and reflection depth for the GPR method.

The sixth thesis gives new results for the parameter sensitivities of GPR measurements.

The last (seventh) group of theses investigates the imaging of rebar structures using GPR measurements.

The dissertation is based on 8 years of own development work. This development work covers measurement planning, field measurement execution, measurement processing and interpretation, and numerical modelling for which the candidate also wrote self-developed software.

A major advantage of the dissertation is that it can be used to study a wide depth range, from a few meters to hundreds of kilometers. The new scientific results can be applied to small, medium and deep depths in the fields of mineral resources exploration and environmental protection.

DOI: 10.14750/ME.2022.008

The thesis written by Endre Nádasi is a valuable work that can be used in practice, it fulfils all the requirements set by Mikoviny Sámuel Doctoral School of Earth Sciences. The presented results are representing the Candidate's own work, so I deeply recommend it for the final open debate.

Scientific supervisor

Private Prof. Dr. Endre Turai

Sign……..

Date: 24/08/2021, Miskolc

DOI: 10.14750/ME.2022.008

CONTENT

DOI: 10.14750/ME.2022.008

DOI: 10.14750/ME.2022.008

1. Introduction

Electromagnetic (EM) techniques play a unique role among geophysical methods. They are able to gain information from the shallow subsurface until the deep crust and upper mantle. Thanks to the huge depth interval they can reach, the use of EM methods is very widespread. Environmental, civil engineering, hydrogeological, archeological and mineral exploration tasks are all typical applications.

If we compare the basic equations of the electromagnetic methods with the equations of the gravitational and magnetic methods, then in addition to the many formal similarities, we can also observe a fundamental difference. While for the latter two methods the key parameter is the rock characteristic itself (density and volumetric magnetization), in EM geophysics, in addition to the rock characteristics, electric charges (spatial and surface electric charge density) and currents (spatial electric current density) are included (Szarka, 1990). This means that compared to the other two methods in geoelectrics we can infer 'indirectly' our parameters to be determined.

Although research has for decades focused on determining the direct relationship between anomalies and geoelectric parameters, the real sources of anomalies are induced interfacial and polarization charges. Although the calculation of the resulting electric field using charging systems is much more difficult, they still play an important role in understanding geoelectric anomalies.

The significant part of my PhD research work is linked to the magnetotelluric (MT) and ground penetrating radar (GPR) methods which is summarized in this dissertation. In case of my MT research, I dealt with two datasets from two different area. One of them is a smaller dataset from the Cserehát region, North Eastern Hungary. I took part in the survey program of all the 24 MT stations. The relatively high frequency (0.01 – 1 Hz) MT data were collected in order to get more information about the sulphide mineralization of the area. Because of the massive presence of the sulphide, the dataset is assumed to contain the IP (induced polarization) effect. The dataset was cleaned, interpolated and prepared for inversion. 2D and 3D inversion algorithms were also applied to create resistivity models. Beside producing inversion models, I also performed statistical investigations on the MT sounding curves to draw conclusions on the dimensionality of the resistivity structure. The other dataset is from the Western Superior region, North America. This is a subset of Lithoprobe and EarthScope MT data which cover this region. I present the anisotropy study and the large-scale 3D inversion of these data.

DOI: 10.14750/ME.2022.008

In case of my GPR research, I introduced a new approach for parameter estimation. In the industrial practice of GPR, the velocity of the radar waves is expressed by the equation for dielectrics. This approximation is correct in case of low-conductivity media, but sometimes, GPR sounding should be performed in lower resistivity (10–100 Ωm) environment. In this case, based on the equation for dielectrics calculated wave propagation velocities can differ from the real propagation velocities of materials, which behave as lossy media in fact.

I introduced the parameter sensitivity approach for the GPR method. I investigated the GPR parameter sensitivities for the EM petrophysical parameter changes. This approach and the sensitivity analysis were tested on synthetic models as well.

The development and application of different EM methods has always been in the focus at the Department of Geophysics, University of Miskolc. My aim was to do applied research into this field, especially in MT and GPR.

1.1. EM geophysics

Electromagnetic (EM) geophysics is a very important family of applied geophysics that can provide information on the spatial distribution of the Earth's electromagnetic rock characteristics from a depth of hundreds of kilometers to the surface. Their use is based on the measurement of the EM space of natural and artificial sources, which is distorted compared to the normal space (homogeneous, isotropic half-space) due to the inhomogeneity or anisotropy of the EM parameters.

Electromagnetic research methods can be grouped in several ways, based on the source used, we can distinguish between natural and artificial source methods, and we can talk about DC and AC methods.

The basic correlations of the electromagnetic method family are the Maxwell equations (1-4) of classical electrodynamics (two scalar, two vector equations), the material equations for electromagnetic rock properties (5-6), and the differential Ohm's law (7). The aim of the set of methods is to determine the spatial distribution of these three petrophysical characteristics (σ: electrical conductivity, μ: magnetic permeability, ε: dielectric constant, or permittivity).

$$1.\ \mathrm{rot}\,\bar{\mathbf{H}} = \bar{\mathbf{j}} + \frac{\partial \bar{\mathbf{D}}}{\partial t} \qquad \textit{Ampère's law (with Maxwell's addition of displacement current),} \quad (1)$$

where H is the magnetic field strength, j is current density, D is the electric displacement field, t is time. Both the displacement current and the conduction current create a magnetic vortex field.

DOI: 10.14750/ME.2022.008

2. $\mathrm{rot}\,\bar{\mathbf{E}} = -\frac{\partial \bar{\mathbf{B}}}{\partial t}$ *Faraday's law of induction,* (2)

where E is electric field strength, B is magnetic field. A change in magnetic induction over time creates an electric vortex field.

3. $\mathrm{div}\bar{\mathbf{B}} = 0$ *Gauss's law for magnetism* (3)

The magnetic induction vector is source-free because there are no real separable magnetic charges (there is no magnetic monopole).

4. $\mathrm{div}\bar{\mathbf{D}} = \rho_v$ *Gauss's law,* (4)

where ρ_v is the volume charge density. The sources of shear current are real charges.
Material equations:

$\bar{\mathbf{D}} = \varepsilon\bar{\mathbf{E}}$ (5)

$\bar{\mathbf{B}} = \mu\bar{\mathbf{H}}$ (6)

$\bar{\mathbf{j}} = \sigma\bar{\mathbf{E}}$ *differential Ohm's law* (7)

When a material is located in an electromagnetic wave field, conduction and displacement currents are generated in it. The conduction currents are responsible for the attenuation of the waves, the wave gradually releases its energy on the ohmic member of the impedance of the material. The media can be grouped in this way in terms of EM energy absorption, which is determined by the relationship between the conduction and displacement currents:

- *ideal insulators (ideal dielectrics):* $\bar{\mathbf{J}}_\mathbf{c} = 0$ (8)
- *insulators (dielectrics*): $\bar{\mathbf{J}}_\mathbf{c} \ll \bar{\mathbf{J}}_\mathbf{d};\ \sigma \ll \varepsilon\omega$ (9)
- *lossy media: energy loss cannot be neglected*

  good conductors $\bar{\mathbf{J}}_\mathbf{c} \gg \bar{\mathbf{J}}_\mathbf{d};\ \sigma \gg \varepsilon\omega$ (10)

  ideally good conductors $\sigma = \infty,$ (11)

where ω is the angular frequency, j_c is the conduction current density, j_d is the displacement current density.

Crustal rocks - and certainly mantle and core materials - almost always behave as lossy media, usually in the category of good conductors. The air layer above the earth's surface (up to the ionosphere) can be considered a dielectric.

DOI: 10.14750/ME.2022.008

1.2. Magnetotellurics

Magnetotellurics (MT) is a passive (natural source) electromagnetic geophysical method. Its use is based on the physical principle that the electromagnetic field (secondary field) formed in the rocks of the Earth under the influence of the natural electromagnetic field (primary field) is a function of the resistivity (conductivity) and geometry of the rock layers. The electromagnetic (EM) field is described by the change in electric and magnetic field strength vectors over time. When applying the MT method, the change of the sum of the primary and secondary EM space over time is recorded on the Earth's surface (Novák, 2010). The method was first described by Tikhonov (1950) and Cagniard (1953), and its domestic introduction was by Antal Ádám (1956, 1958, Ádám and Bencze, 1961) and Ernő Takács (Takács, 1957, 1960, 1968, Csókás and Takács, 1964). Thanks to the development of instrumentation, data processing and interpretation techniques, MT has now become a suitable method for solving a wide range of geological tasks.

The Earth's natural electromagnetic field is the result of the combined action of internal and external forces. According to dynamo theory, the source of the Earth's own magnetic field is to be found in the outer core in the fluid state. The resulting dipole-like magnetic field is distorted by the flow of corpuscular particles ("solar wind") from the Sun, creating a characteristically elongated shape of the magnetosphere.

The frequency range used in magnetotelluric exploration is usually between 10^{-4} and 10^{4} Hz. Signals from remote radio transmitters are also used in shallow research, including the 10^{5} Hz (a few hundred kHz) signal range in radio magnetototellurics (RMT). The electromagnetic signals used can be divided into two main groups based on their origin. Micropulsions between about 0.001 and 1 Hz occur from the interaction of the magnetosphere and the solar wind. The other group of signals with a frequency greater than 1 Hz comes from terrestrial thunderstorm activity. Lightning-generated waves, which form the latter group, propagate in the waveguide between the earth's surface and the ionosphere (Simpson and Bahr, 2005).

Taking into account the nature of the electromagnetic sources used, the properties of the materials of the Earth's crust and the depth of the study, two important assumptions and simplifications are usually used in magnetotellurics:

- quasi-stationary approximation: in the range of 10^{-5}–10^{5} s of period time, in the case of non-extremely low conductivities, the displacement currents are negligible compared to the conduction currents. Consequently the propagation of electromagnetic waves in the Earth can be described as a diffusion process (the relationships of quasi-stationary

spatial change can be transformed into a diffusion equation), which makes it possible to extract information on the conductivity of rocks in the form of volume averages.

- plane wave assumption: since electromagnetic waves, which can be considered as the source of magnetotellurics, are generated relatively far from the Earth's surface in the ionosphere, they can be considered as distant sources, so they can be considered uniformly plane polarized waves moving vertically downwards to Earth.

Electromagnetic waves propagate attenuated in all media except vacuum. The degree of attenuation depends on the circular frequency (ω) and the electromagnetic properties of the medium (ε: permittivity, μ: magnetic permeability, σ: conductivity). It is important to know the ranges of these electromagnetic material properties for Earth's rocks. The permittivity of the vacuum to that of water is about 80 times that of the relative permittivity of the minerals, mostly less than twenty. Since the displacement current at the frequencies used in magnetotellurics is negligible, the dielectric constant does not play a role. The value of magnetic permeability in vacuum for most rocks is the absolute magnetic permeability. Second-order magnetic phase transitions can also occur in the Earth's crust. The phenomenon, also known as the Hopkinson effect, involves a significant change in magnetic susceptibility, which can cause magnetic and magnetotelluric anomalies that can also be observed on the surface. In this case, with the assumption $\mu_r = 1$ (μ_r: relative magnetic permeability), the magnetotelluric inversion gives an erroneous result.

The resistivity of the rocks that make up the Earth's crust varies over a wide range, covering roughly eight orders of magnitude. The resistivity of a rock is determined in part by the resistivity of the minerals that make it up, and is fundamentally influenced by porosity, the degree of pore saturations, the quality and concentration of dissolved salts, the degree of decay, and temperature. Most rock-forming minerals are considered to be practically insulating, as their resistivity is millions of ohms. The current thus actually flows in the solutions filling the rock cracks, the resistivity of which is orders of magnitude lower than that of the minerals, thus determining the resulting resistivity of the rocks. Exceptions are rocks containing large amounts of metallically conductive minerals (pyrite, marcasite, pyrrhotite, iron mica, magnetite, chalcopyrite, graphite).

When the waves reach the surface of the Earth, they are partly reflected and partly penetrate below the surface by a diffusion process (Vozoff 1972). Due to the high resistance contrast between air and rocks, the wave travels vertically down below the surface regardless of the angle of incidence it reaches the solid crust. However, in the new medium, the energy and amplitude of the wave begin to decrease exponentially, and the degree of attenuation can

DOI: 10.14750/ME.2022.008

be expressed by the absorption factor (a), which can be calculated from Equation (12). The reciprocal of this is the skin depth (d_s), which expresses the depth (13) at which the energy of the electromagnetic wave decreases to 1/e of its surface value:

$$a = \sqrt{\frac{\mu\sigma\omega}{2}}, \tag{12}$$

$$d_s = \sqrt{\frac{2}{\mu\sigma\omega}} \cong 500\sqrt{\rho T}, \tag{13}$$

where T is the period and $\rho=1/\sigma$ is the resistivity.

The relationship of horizontal electrical (E_x and E_y) and magnetic (H_x and H_y) field components to a given frequency (3) is described by a 2x2 complex tensor, the impedance tensor (Cantwell, 1960). This quantity carries information about the subsurface specific conductivity distribution. Since at a given frequency it depends only on the electromagnetic properties of the medium and is independent of the source of the electromagnetic field, it can be considered as a response function of the magnetotelluric method:

$$\overline{E} = \underline{\underline{Z}} \cdot \overline{H} \;\; ; \quad \begin{bmatrix} E_x \\ E_y \end{bmatrix} = \begin{bmatrix} Z_{xx} Z_{xy} \\ Z_{yx} Z_{yy} \end{bmatrix} \cdot \begin{bmatrix} H_x \\ H_y \end{bmatrix}. \tag{14}$$

The apparent resistivity can then be calculated using the following formula:

$$\rho_a = \frac{1}{\mu\omega}\left|Z_{ij}\right|^2 \text{ [}\Omega\text{m] (i,j = x,y).} \tag{15}$$

For more information, see the impedance tensor phase:

$$\varphi_{ij}(\omega) = \text{arctg}\left(\frac{\text{Im}(Z_{ij}(\omega))}{\text{Re}(Z_{ij}(\omega))}\right) \text{ [rad] (i,j = x,y).} \tag{16}$$

The geomagnetic induction vector (T), also known as the “tipper”, specifies the relationship between the horizontal and vertical components of the magnetic field strength vector. It is also called an induction arrow, a complex vector quantity. It is suitable for detecting changes in lateral conductivity (Novák, 2010):

$$2H_z = \left[T_x T_y\right] \cdot \begin{bmatrix} H_x \\ H_y \end{bmatrix}. \tag{17}$$

Using the above tools, MT provides an opportunity to get an idea of the resistivity distribution of subsurface rocks, which can be used to obtain geological information. According to the spatial extent of the geological structure, we distinguish between one-dimensional (1D),

two-dimensional (2D), and three-dimensional (3D) models. The impedance tensor varies according to the dimension number. The calculation of different rotational invariants of the impedance tensor offers further possibilities to analyze MT data (Szarka and Menvielle 1997, Szarka et al. 2000).

Issues of magnetotelluric interpretation in the case of dispersion (IP) effects

To the best of our current knowledge, in magnetotellurics we have to reckon with the regular occurrence of the effects of the frequency dispersion of the resistivity caused by induced polarization (IP) anomalies. It is likely that IP effects are expected to appear in magnetotelluric data primarily in geological environments for which sulfide ore minerals occur in sprinkled or concentrated form. Typically, such a model can be geothermal reservoirs, especially high-enthalpy hydrothermal systems connected to the fracture zones of the basin floor. A similar model could also be the immediate environment of hydrocarbon occurrences with the so-called pyrite chimneys. Frequency dispersion effects are also expected in the presence of graphitic formations. There are domestic examples for each of the three model types, which have been verified by MT measurements.

It is still true that the specific electrical conductivity is considered frequency independent when processing and interpreting the applied electromagnetic data, so the IP phenomenon is not taken into account. This assumption is acceptable for the most part, but not in some cases.

Zoltán Nagy (2003) published an algorithm for calculating the MT resistivity and phase curves of a horizontally layered (1D) geoelectric model that also takes into account the IP effect. The Cole-Cole model (18) was used to describe the frequency dispersion:

$$\rho(\omega) = \rho_{DC}\left\{1 - m\left[1 - \frac{1}{1 + (j\omega\tau)^c}\right]\right\}. \qquad (18)$$

He produced three-layer models in which, in addition to the DC resistivity (ρ_{DC}), he gave the dispersion (IP) parameters (m: chargeability; τ: time constant; c: frequency dependence factor). Based on the equivalent effects studied in dispersion and non-dispersion models, it was concluded that the recognition of IP effects from the data of individual MT probes is possible only in exceptional cases, with favorable model parameters, but the existence of the effect cannot be ruled out in any case. In practice, the recognition and evaluation of dispersion effects can only be expected from the combined use of TM-mode resistivity and phase data in the possession of accurate phase measurement data.

DOI: 10.14750/ME.2022.008

1.3. GPR (Ground Penetrating Radar)

Ground Penetrating Radar (GPR) is an active source electromagnetic geophysical method. It can be used effectively in shallow depth exploration, since the waves emitted from the antenna attenuate relatively quickly when they reach the studied medium (soil, rock, concrete, etc.). The frequency range used is wide, ranging from about 10 MHz to 2 GHz, depending on the exploration purpose. Its great advantage is the fast imaging and being non-destructive. Today, it has been applied in many fields, from cavity exploration (Lyu et al. 2020) to the study of engineering facilities (Pajewski et al. 2013) to archaeological surveys (Trinks et al. 2012).

The reflected wave response from the investigated medium depends on the EM parameters:

- permittivity (ε),
- magnetic permeability (μ),
- conductivity (σ),

and the frequency (f). All of the EM parameters are frequency dependent quantities. The magnetic permeability does not influence the radar wave propagation significantly, unless the investigated medium is ferromagnetic. Its effect is negligible in the case of materials with relative magnetic permeability value around one ($\mu_r \approx 1$). The permittivity is the key parameter in GPR measurements. It influences the wave propagation velocity and the reflection coefficients strongly, and also affects the vertical and horizontal resolution. It is a complex quantity; its real part is the relative dielectric constant. The conductivity or its reciprocal, the resistivity, plays an important role in GPR practice as well. Basically, GPR cannot be applied in a low resistivity environment successfully because of fast wave attenuation and absorption, but sometimes it can be applied under relatively low resistivity (10–100 Ωm) conditions, very low penetration in particularly, using highly sensitive instruments.

The combination of these properties for each material results in notable variations in penetration depth for GPR waves (Martinez and Byrnes 2001). These data are very useful, but all formations (and architectures) are complex mixtures of different materials and GPR parameters are sensitive to porosity, water saturation, component geometries and electrochemical interactions. The main difference between the relative dielectric constant and conductivity values of the materials is that the conductivity of rocks changes in a very wide range, many orders of magnitude, while the relative dielectric constant usually changes between 1 and 80.

DOI: 10.14750/ME.2022.008

The basic equations of GPR method can be derived from the Maxwell equations, which are considered to be the axioms of the classical electrodynamics. These are valid assuming vertically downward spreading plane waves and an isotropic half-space. Furthermore, low-loss medium is assumed in GPR practice (Jol 2008). This means that the conduction currents are negligible compared to the displacement currents ($\sigma^2 << \varepsilon^2\omega^2$), where ω is the angular frequency ($\omega=2\pi f$), f is the frequency). Hereinafter, formulas of different parameters (wavelength, resolution, skin depth) calculated for lossy media and for dielectrics are presented and compared to each other (see in Chapter 6.1).

When evaluating the GPR measurements, the determination or estimation of the wave propagation velocity plays a key role, because the depth of the reflecting object from the time slice can be obtained based on the velocity:

$$v_d = \frac{1}{\sqrt{\mu\varepsilon}} \cong \frac{c}{\sqrt{\varepsilon_r}}. \tag{19}$$

The propagation velocity of electromagnetic radar waves in an insulating (low loss) medium is described by the upper relation, where c is the speed of light in a vacuum. From this, it can be concluded that a constant increase in dielectric results in a decrease in the wave propagation velocity. In general, the propagation velocity formula calculated for a lossy medium (v_l) is more complex than in Equation (19):

$$v_l = \frac{1}{\sqrt{\frac{\mu\varepsilon}{2}\left(\sqrt{1+\frac{\sigma^2}{\varepsilon^2\omega^2}}+1\right)}}. \tag{20}$$

It already depends on the conductivity, frequency and magnetic permeability. In modeling, velocity information can be used to calculate the expected propagation time (TWT – two-way time), and in measurement to estimate the depth of reflection with knowledge of propagation time:

$$h = \frac{TWT \cdot v}{2}, \tag{21}$$

where h is the depth of the reflecting surface.

Besides propagation velocity, wavelength is also an important quantity in terms of the resolution (vertical and horizontal) of the investigation. In case of dielectrics, wavelength can

be calculated as follows:

$$\lambda_d = \frac{2\pi}{\omega}\sqrt{\mu\varepsilon}, \tag{22}$$

but assuming lossy medium, the formula of the wavelength is more complex, the conductivity appears in the equation as well:

$$\lambda_l = \frac{2\pi}{\omega}\sqrt{\frac{\mu\varepsilon}{2}\left(\sqrt{1+\frac{\sigma^2}{\varepsilon^2\omega^2}}+1\right)}. \tag{23}$$

A priori information of resolution is crucial in GPR survey design. Vertical and horizontal resolution can be distinguished. Vertical resolution (R_v) is the shortest distance, where reflections from two different layer boundaries can be separated distinctly on radargram, therefore they fulfill the Rayleigh criterion (Pethő 2009). It is expressed as a quarter of the wavelength:

$$R_v = \frac{\lambda}{4}. \tag{24}$$

Horizontal resolution (R_h) has several existing definitions. One of the most frequently used formulas can be found in Rial et al. (2009), which expresses the quantity with the diameter of the first Fresnel zone:

$$R_h = \sqrt{\frac{\lambda^2}{4}+d\lambda}, \tag{25}$$

where d is the vertical distance between the transmitter antenna and the reflecting surface.

When GPR waves reach the Earth's surface (or the investigated solid material), they propagate by diffusion. The energy and the amplitude of the EM waves attenuate exponentially in the ground. The magnitude of this can be expressed by the attenuation constant:

$$a = \omega\left\{\frac{\mu\varepsilon}{2}\left[\left(1+\frac{\sigma^2}{\varepsilon^2\omega^2}\right)^{\frac{1}{2}}-1\right]\right\}^{\frac{1}{2}}. \tag{26}$$

The skin depth (d_s) is defined as the depth at which the intensity or power of the field decays to 1/e of its surface value. It can be calculated as the reciprocal of the attenuation coefficient (26). It is identical to the penetration depth:

$$d_s = \frac{1}{a}. \tag{27}$$

DOI: 10.14750/ME.2022.008

2. Statistical analysis of MT data

In this chapter I present the statistical analysis of a previously processed MT dataset from Northeastern Hungary. I applied classical and modern statistical tools as well. The goal of this investigation was to clarify the dimensionality of the geological structure station by station. Besides, the calculated average sounding curves served as a start model for the inversion (Chapter 3). The sounding curve-based clustering also helped the interpretation of the conductivity structure. The description of the exploration area including geological and geophysical aspects is presented in Chapter 3.

2.1. Classical statistical analysis

Average (28) and standard deviation (29) of apparent resistivity and phase values (TE and TM) were calculated to each frequency:

$$\rho_{a,avg}(f) = \frac{\sum_{i=1}^{n} \rho_{a,i}}{n}, \qquad \varphi_{avg}(f) = \frac{\sum_{i=1}^{n} \varphi_i}{n}, \tag{28}$$

$$\rho_{a,dev}(f) = \sqrt{\frac{\sum_{i=1}^{n} (\rho_{a,i} - \rho_{a,avg})^2}{n-1}}, \qquad \varphi_{a,dev}(f) = \sqrt{\frac{\sum_{i=1}^{n} (\varphi_{a,i} - \varphi_{a,avg})^2}{n-1}}. \tag{29}$$

These values were plotted in the function of period (Figure 1). Log-log scale was used for the resistivity data and semilog scale for the phase values.

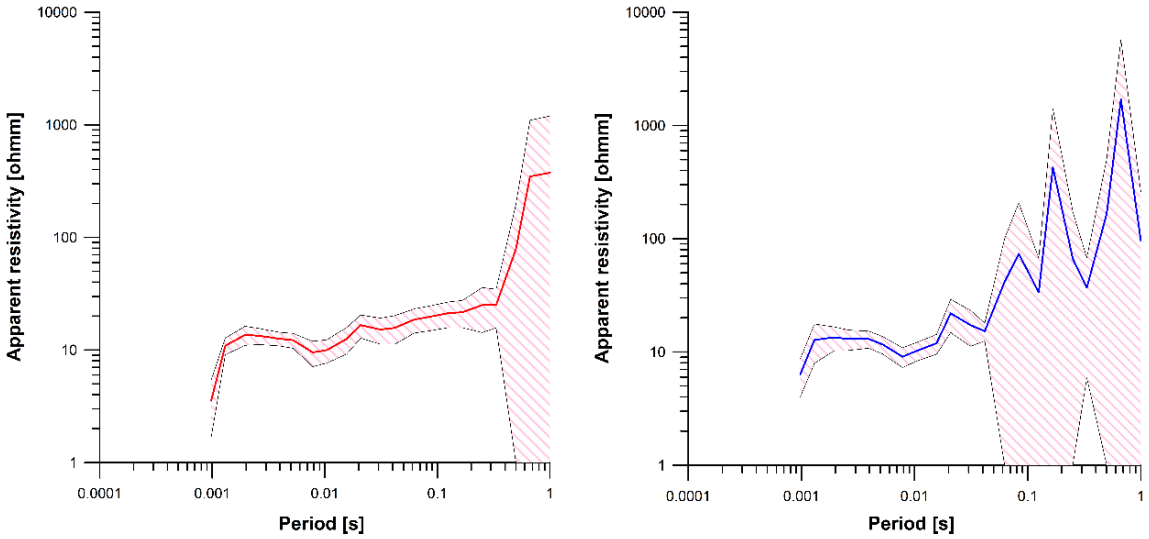

DOI: 10.14750/ME.2022.008

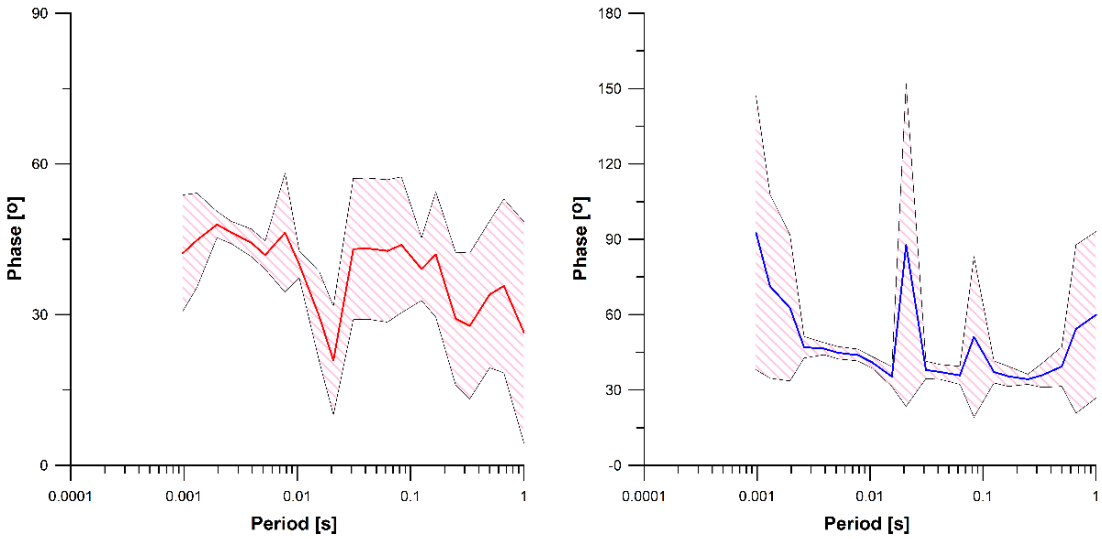

Figure 1. The expected MT sounding curves in the area, showing the standard deviation intervals. Red curves indicate the TE mode, blue ones the TM mode. The upper two graphs show the resistivity while below the phase curves can be seen.

It can be concluded that the standard deviation of apparent resistivity is small at high frequencies. This is true above 3Hz in TE mode and above 50 Hz in TM mode. In case of phase curves, – especially in TM mode – significant standard deviation can be observed at high frequencies as well.

Based on the Pearson correlation coefficients between the TE and TM sounding curves, correlation maps were edited (Nádasi et al. 2017). The dimensionality (1D or more dimensions) of the geological structure can be concluded based on these (Figure 2). The higher is the correlation coefficient, the more we can expect 1D structure at a given station.

The correlation map determined for the apparent resistivity shows that strong correlation values were obtained for the ir32, ir06, ir07, and ir10 MT stations. The lowest correlation coefficient values can be observed at stations ir30, ir31, and ir34. Since negative values also occur at the phase, negative correlation values also appear there. It can be observed that in the case of the stations in the eastern part of the measurement area, positive, in some places strong correlation coefficient values occur on the map defined for the phase. Based on the correlation maps, it can be stated that the geological structure is 1D with a good approximation below the measurement points ir6, ir7, ir9, ir10 and ir12.

DOI: 10.14750/ME.2022.008

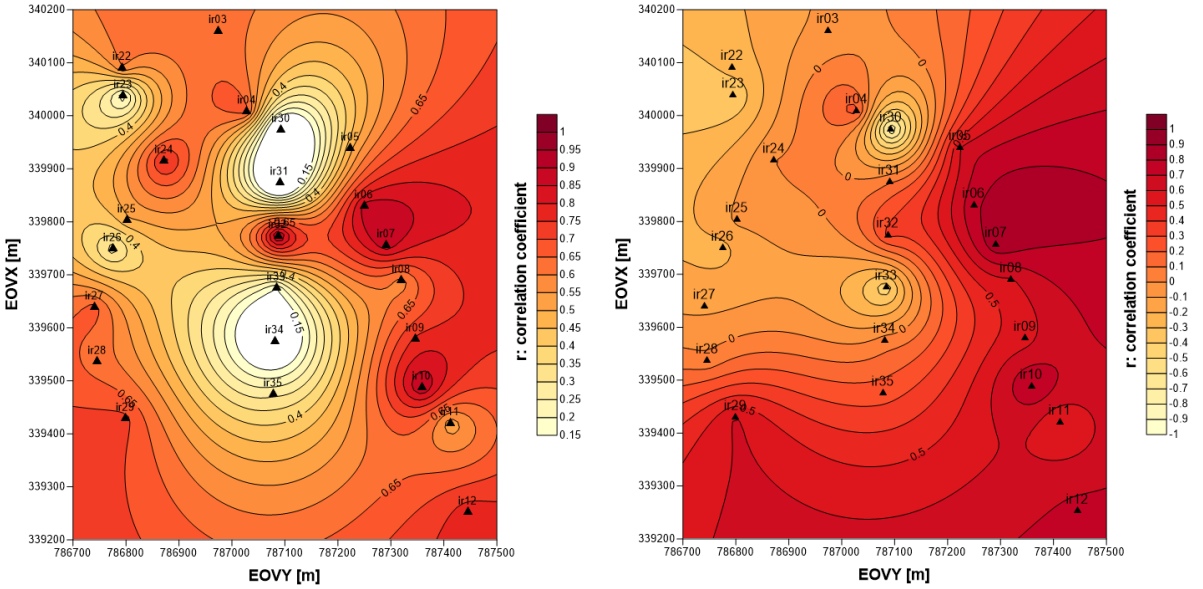

Figure 2. Correlation maps defined for the area, for parameter ρ_a - on the left, for phase - on the right.

2.2. Cluster analysis

Each measurement station was grouped based on their associated probing curves using non-hierarchical clustering. Of the non-hierarchical clustering methods, the most commonly used K-means method was used (MacQueen, 1967). Clustering was also performed based on the L2 norm-based Euclidean and L1 norm-based city-block distance definitions interpreted between the data objects (Figure 3).

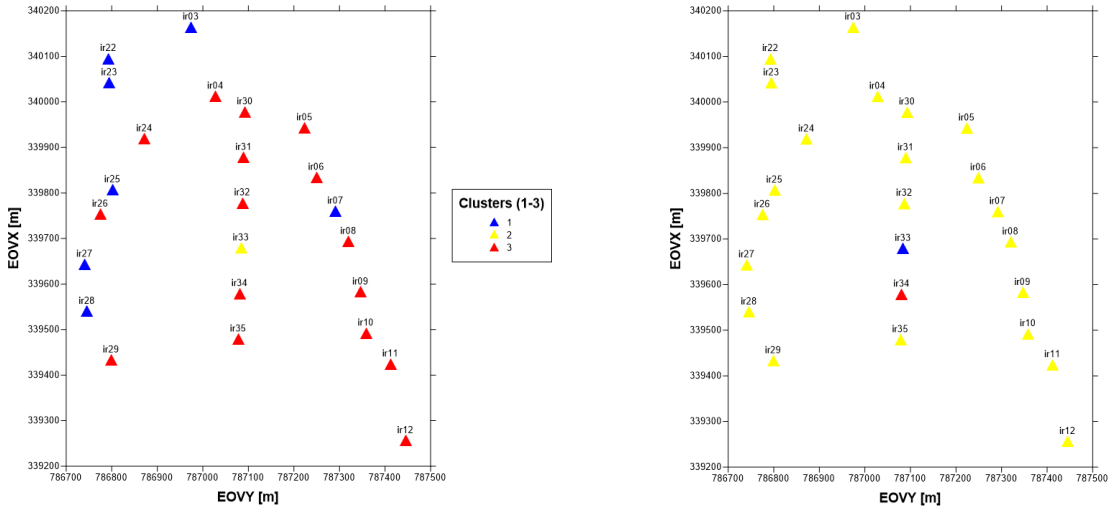

Figure 3. Result of K-means clustering based on city-block (left) and Euclidean (right) distances.

DOI: 10.14750/ME.2022.008

A feature of non-hierarchical clustering techniques is that the cluster number must be specified in advance. In the case of MT stations, I considered the formation of 3 groups to be appropriate, but I also created different group numbers (2, 4, or 5) which did not show better result. Because Euclidean distance-based clustering is more sensitive to outlier elements, we obtained a more realistic group classification using city-block distance training. Using this scale, I created a kriging-interpolated cluster map (Figure 4), on which a low cluster number anomaly is drawn in the area marked with an ellipse.

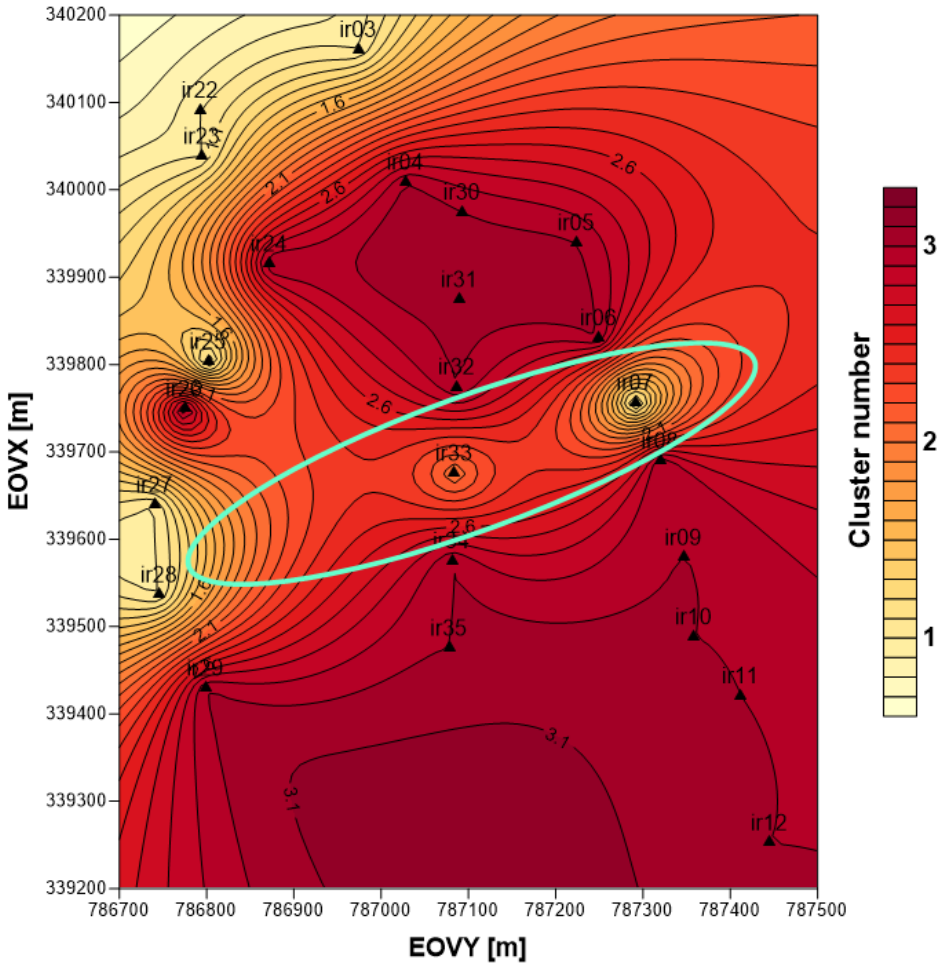

Figure 4. Interpolated (kriging) map of the group numbers of MT stations clustered using the K-median method based on city-block distance.

The statistical investigation of the MT sounding curves proved to be highly important in the treatment of outliers. It could help in the quality control of the data and getting rid of possible bad data. Performing these operations is an important step before starting inversion processes.

Based on the expected apparent resistivity and phase, as well as the associated standard deviation curves, it can be concluded that the upper sedimentary units show a nearly 1D

DOI: 10.14750/ME.2022.008

character. The curves for the TE and TM modes usually begin to separate at periods greater than 1 second (frequencies less than 1 Hz). By calculating the average curves, an area-specific resistivity probing curve was generated for frequencies greater than 1 Hz. The correlation map shows well the areas where electromagnetically multidimensional (2D, 3D) structures appear. This is because the lower the correlation coefficient, the less one-dimensional the geoelectric structure. The lowest correlation coefficients occurred for stations ir30, ir31, and ir34.

The cluster analysis showed that the previously assumed WSW-ENE oriented structural elements (faults, fault zone) can be really present in this area. Along the strike direction drawn by station ir07 and ir33, a negative anomaly appears on the contour map (Figure 4) of the cluster numbers. This direction coincides with the assumed structural strike direction.

Overall, it can be stated that statistical analysis of MT sounding curves from the same area can provide useful information that helps to establish both a more accurate geophysical model and geological interpretation.

Thesis 1.

Field MT measurements were processed by correlation analysis and cluster analysis.

Thesis 1. a Using correlation analysis, I showed that the layer sequence is 1D below the eastern part of the Cserehát research area, while it is multidimensional (2D or 3D) below the central and western part.

Thesis 1. b With the non-hierarchical cluster analysis of the MT measurements, I proved the existence of WSW-ENE directional structural lineaments (faults).

DOI: 10.14750/ME.2022.008

3. Inversion of local, high frequency MT data

In the Cserehát region (NE Hungary), in the vicinity of Irota and Gadna villages an indication of sulfide mineralization is well-known (Csáki 1976, Németh 2012, Czeglédi 2013). In order to delineate the ore mineralization, magnetotelluric (MT) measurements were performed which proved the presence of conductive anomaly. The MT measurements were performed along three nearly parallel profiles, at 24 stations altogether (Figure 5). This anomaly can only be interpreted reliably with the survey results of other geophysical methods. The potential field methods demonstrated gravity and magnetic anomalies, the seismic survey pointed out important structural elements, mainly faults (Szalai et al. 1987). After data processing and statistical analysis (Chapter 2), the MT data were processed by 2D and 3D inversion techniques, which I present in this chapter.

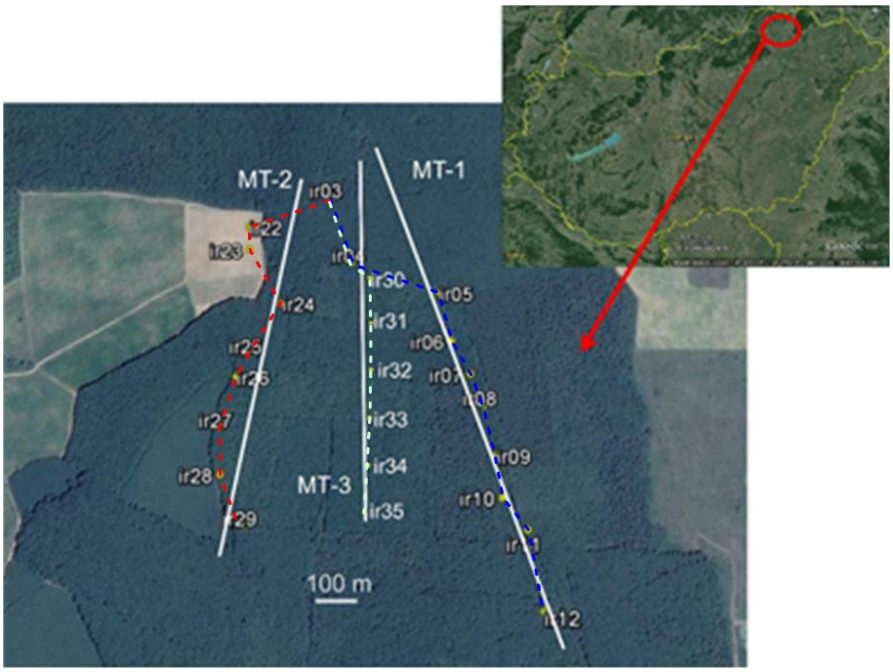

Figure 5. The satellite picture of the exploration area with the location of the measured points (ir03–ir12, ir22–ir29, ir30–ir35) and profiles of 2D inversions (MT-1, MT-2 and MT-3). Dashed lines indicate the original profile tracks.

3.1. Geological background and earlier geophysical surveys

The Cserehát consists of metamorphosed Paleozoic rocks and Cenozoic sediments. A major sedimentary hiatus (Devonian–Miocene) is observable between them. The Paleozoic formations consist of mainly limestone and shale with notable graphite content. They

DOI: 10.14750/ME.2022.008

underwent a low-grade (greenschist facies) metamorphism in the Cretaceous (Árkai 1977). The Miocene-Pliocene sediments involve alternating sandstone, clay and silt layers.

A considerable geomagnetic anomaly was explored in the middle of the last century, in the vicinity of Irota. Uranium exploration has started in the sixties with a detailed exploration drilling program. However, uranium was not found in significant amount, the exploration generated a lot of important geological information. The analysis of core samples proved the presence of mostly pyrrhotite containing sulphide mineralization (Csáki 1976). In addition, as a result of new geological observations, it is known, that the area is dissected by Neogene faults with significant downthrows. Based on previous information the area is prospected for base and precious mineralization. Furthermore, REE minerals (monacite, xenotime) were described in the near-surface young sediments.

From the data of the gravity base network with a density of 5 points / km^2, a Bouger anomaly map and a residual anomaly map series were calculated (Szalai et al. 1987). The gravitational field is constantly decreasing north of the southeastern edge of the Szendrői Mountains (towards the Paleozoic outcrops). The positive anomaly is also called the Irota gravitational maximum line.

A geomagnetic anomaly also became known near Irota as early as the 1950s, as a result of which ore exploration began in the area later. For more accurate localization, helicopter gamma spectrometry and aeromagnetic measurements were performed in 1986 by the Bulgarian Air Geophysical Service. As a result of the measurement, a magnetic field was determined with $k = 21.4*10^{-3}$ [SI] susceptibility. This partly coincides with the Irota gravitational maximum line (Szalai et al. 1987).

In order to better understand the known Irota magnetic anomaly, detailed surface magnetic measurements were made in the area in 2011, along 12 profiles, at a total of 1625 measurement points (Czeglédi 2013). After interpolation of the measurement data, 11 parallel, N-S directional sections were generated, which were processed by 2D inversion with the mag2dc software, and a pole-reduced magnetic anomaly map was created.

Two 2D reflection seismic sections pass through the area, which were also measured in the 1980s. The WSW-ENE strike Sze-1 and the NW-SE strike Sze-4 sections intersect near the Felsővadász-1 (FV-1) borehole. On the Sze-4 section, a fault zone near the FV-1 well can be interpreted. Taking into account the larger-scale seismic measurements and structural geological research, it can be stated that the main direction of the structural lines is WSW – ENE. Presumably, the Paleozoic basement may have broken along these lines and sank step by

step into the deep (Szalai et al. 1987). The basement depth map and the gravitational anomaly map also support this.

3.2. MT data acquisition and processing

The MT measurements were carried out with Metronix GMS-06 24-Bit MT-System. The recordings were registered in three (LF1, free, LF2) frequency bands, with 4096, 512 and 64 Hz sampling frequencies. The registration time at one station was about one hour.

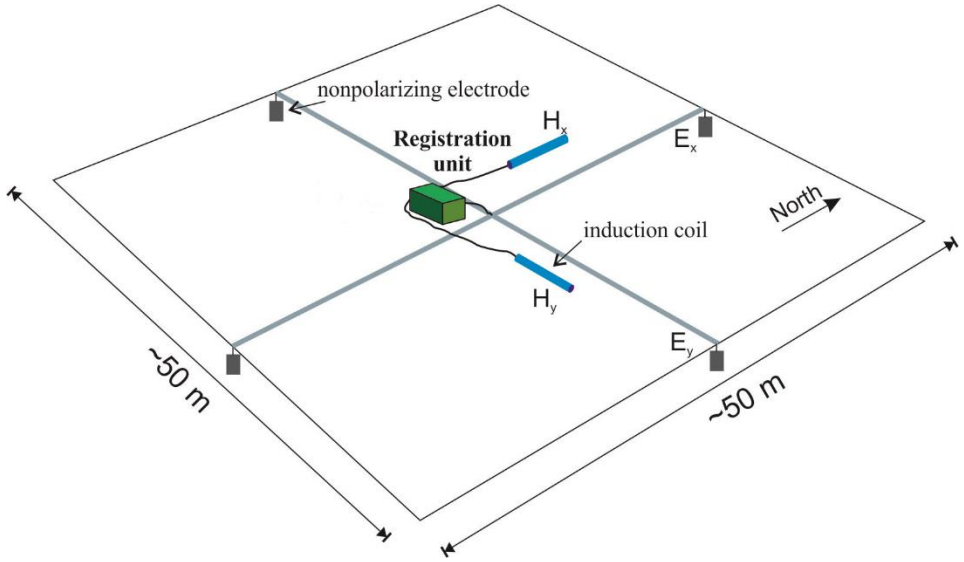

Figure 6. Simplified view of an MT station as deployed at the Irota exploration area.

The magnetic field components were registered with induction coils, the electric components with non-polarizable Pb-Pb_2Cl_2 electrodes. The layout of the MT measuring system is outlined on Figure 6.

The basic task of the MT data processing is to determine the elements of the impedance tensor. It was performed by statistical spectral (frequency) analysis (Sims et al. 1971) in WinGLink software environment.

3.3. 2D inversion

Apparent resistivity and impedance phase graphs were produced after the estimation of the impedance tensor. The impedance tensors were rotated into profile direction. These formed the input parameters for the 2D inversion. The nonlinear conjugate gradients algorithm (Rodi and Mackie, 2001) was used for the 2D inversion of the three sections.

DOI: 10.14750/ME.2022.008

It can be seen on the MT-1 section, that the Paleozoic Basement can be found in deeper and deeper position southward. In the Palezoic basement – which can be considered as an insulator – appears an extremly good conductor rock body (Figure 7). This zone probably contains sulphide mineralization according to drillhole (Fv-1) information (Földessy, 2014). The top of this conductive body can be found in 500 m depth. From the succession of the Felsővadász-1 well the depth of the Paleozoic Basement was extrapolated along the section.

As we can see, the resistivity of the Paleozoic Basement is about 100–200 Ωm on the picture of the MT-1 section. But it is decreasing below -300 m (above sea level) and can be lower than 50 Ωm.

Above the boundary of the Neogene and Paleozoic rocks, additional lower resistivity zones can be observed. They can denote shaly or weathered sedimentary units.

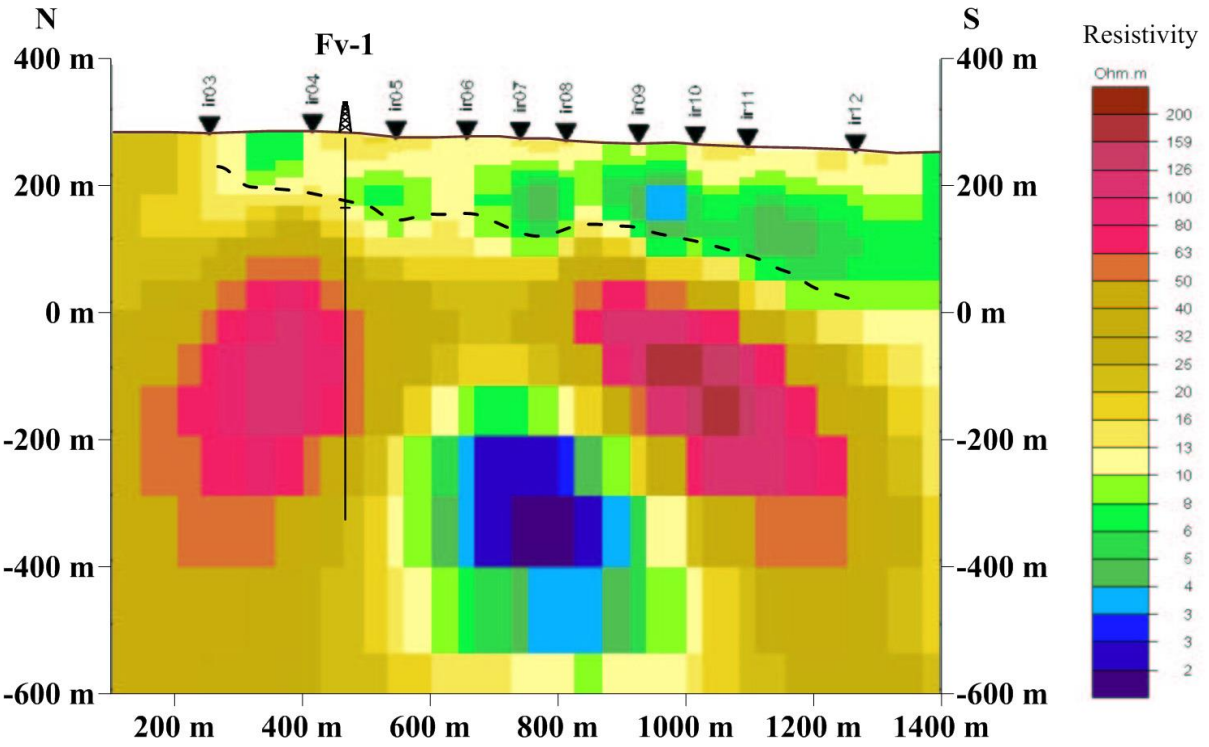

Figure 7. 2D inversion model of the MT-1 section. Fv-1 indicates a borehole, which penetrated pyrrhotite containing zones. Dashed line indicates the Paleozoic basement, the boundary of the Neogene and Paleozoic rocks.

The aim of the MT-2 (ir22-ir29) section was to find the continuation of the low resistivity zone, which was recognized in the MT-1. It was confirmed after the evaluation of MT-2, that similar well conducting zone cannot be found in the MT-2 (Figure 8). To clarify the

cause of the very different resistivity distribution under the two profiles, the MT-3 profile was measured between the two sections.

On the 2D resistivity picture of the MT-2 and MT-3 sections (Figure 8, Figure 9), a relatively high resistive (above 100 Ωm) and thick (200–300 m) body appears. It means, that the low resistivity zone of the MT-1 section does not have continuity towards west.

The northern part of the MT-2 and MT-3 sections was complemented with the ir03 and ir04 stations. These belong originally to the MT-1 profile (Nádasi et al 2015).

It can be observed that the deepening of the basement southward is not so characteristic, as in the case of the MT-1 section. It is very interesting to investigate Figure 10. That horizontal resistivity map raises the possibility of a SSW-NNE direction fault zone.

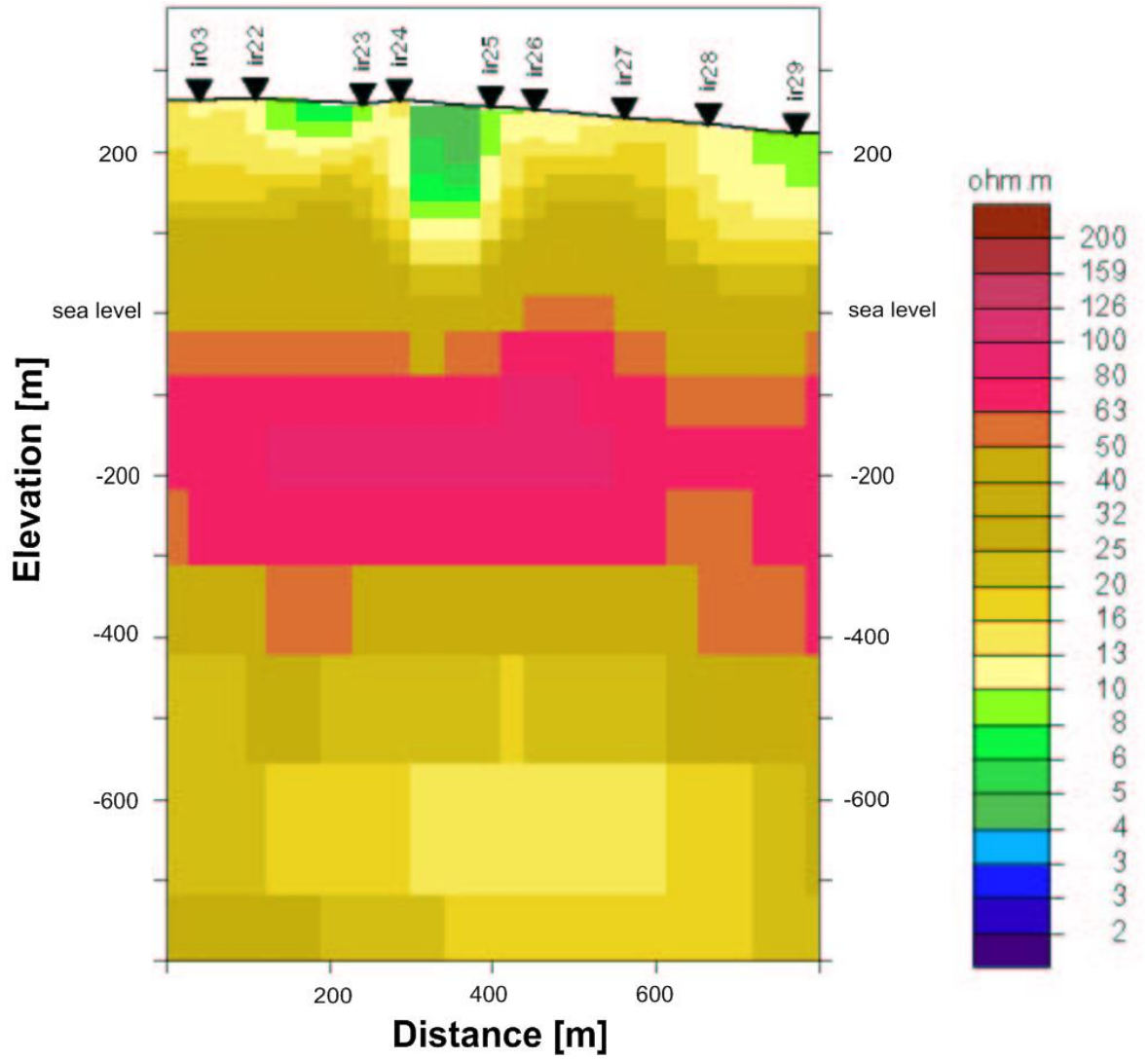

Figure 8. 2D inversion model of the MT-2 section.

DOI: 10.14750/ME.2022.008

A significant low resistivity zone appears obviously on the image of the MT-1 profile, at a depth of about 400–500 meters under the stations ir06, ir07 and ir08. The image of the middle (MT-3) section is quite different, a relatively high resistivity zone is observable.

Since the low resistivity zone does not appear on the 2D inversion image of the western (MT-2, MT-3) profiles, the anomaly can continue towards east. It is also conceivable, that the anomaly does not link to a structural fault, but is the manifestation of a local post volcanic effect. In this case, the extension of the low resistivity unit can be not so significant.

To find the geological cause (sulphide, graphite, clay mineralization) of this anomaly (MT-1) and to clarify the geometry of the low resistivity body, further geophysical and geological investigations (especially exploration drilling) are needed. In addition, the application of the induced polarization (IP) method has to be taken into consideration, because of the presence of pyrrhotite. With the measuring of the MT-3 profile, it became possible to build a 3D geophysical model. It has a great importance, because the geoelectric structure of the exploration area shows significant 3D effect, therefore the 2D approximation is uncertain.

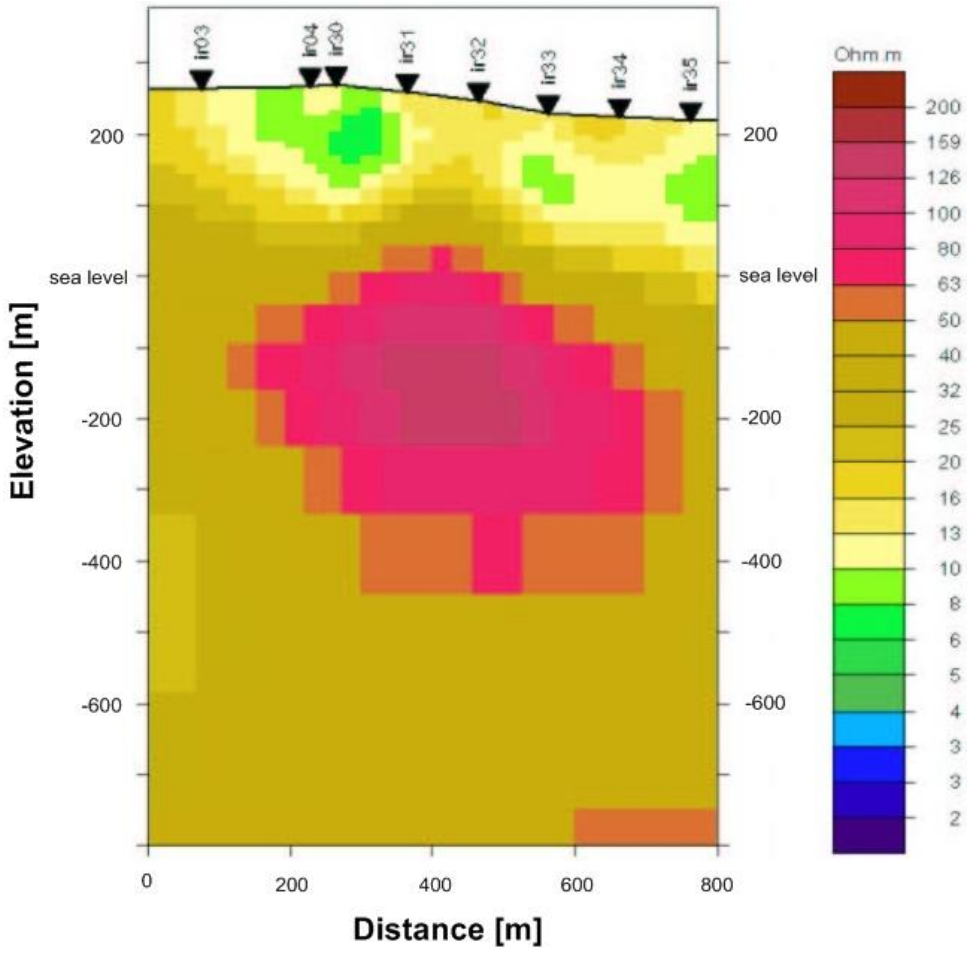

Figure 9. 2D inversion model of the MT-3 section.

DOI: 10.14750/ME.2022.008

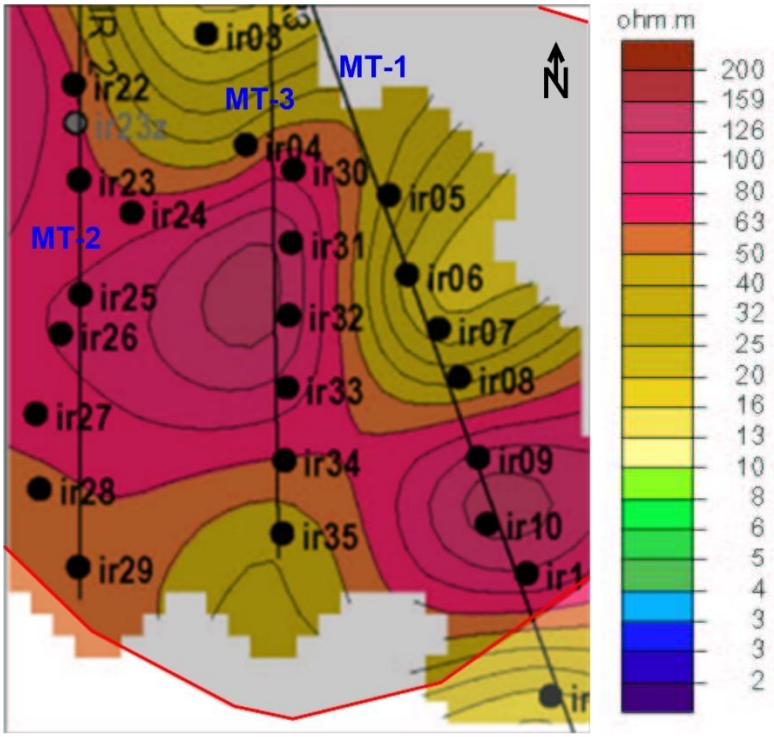

Figure 10. Map of the MT stations and sections. The horizontal distribution of the resistivity, 100 m below sea level. The magnetic anomaly (bordered with red line) covers almost the whole MT exploration area.

The assumed hydrothermal system can modify the physical parameters of the rocks strongly. In this case, the magnetic susceptibility has been increased (pyrrhotite enrichment), and the resistivity has been increased (silification) or decreased (clay mineralization). In the inversion, we could not take into consideration the induced polarization phenomenon. Furthermore, our model supposes an isotrope medium, but the succession has petrological anisotropy, which influences the electromagnetic wave propagation.

These factors increase the uncertainty of the interpretation. To create more reliable geological model, further information (IP, seismic and drilling) should be taken into consideration (Nádasi 2021). The next key step of this MT project is to make 3D inversion with the 24 station data.

3.4. 3D inversion

3.4.1. Theory

Over the last decades, significant progress has been made in developing effective methods of inversion of magnetotelluric data (Constable et al. 1987, Parker 1994). Multiple 3D inversion methods and algorithms have been introduced (e.g. Newman and Alumbaugh 2000,

Sasaki 2001, Siripunvaraporn et al. 2005, Zhdanov et al. 2011ab, Kelbert et al. 2014, Avdeeva et al. 2015, Čuma et al. 2017, Varılsüha 2020), based on finite-difference (FD), finite-element (FE), and integral equation (IE) numerical modeling techniques.

The distortions of regional MT responses by local near-surface geoelectrical inhomogeneities cause major difficulties in interpretation of the MT data. In most cases, due to computational limitations, it is impossible to model the effect of these local 3D near-surface structures using a detailed enough scale. The distortion effect can be formally taken into account by representing the observed MT impedance $\mathbf{Z}^{\text{obs}}$ as a product of the undisturbed impedance tensor and a distortion matrix (Groom and Bailey, 1989):

$$\boldsymbol{Z}^{obs} = \left[c_{ij}\right]\left[\boldsymbol{Z}_{\alpha\beta}^{reg}\right], \tag{30}$$

where $[c_{ij}]$ is 2 X 2 distortion matrix, and $\left[Z_{\alpha\beta}^{reg}\right]$ is 2 X 2 matrix of the regional undisturbed impedance tensor. Magnetic tipper **W** is largely unaffected by the near-surface conductivity inhomogeneities (Chave and Jones, 2012).

Taking into account decomposition (28), the forward MT problem can be written in operator notations as follows:

$$\boldsymbol{d} = \begin{bmatrix} \boldsymbol{cZ}^{reg} \\ \boldsymbol{W} \end{bmatrix} = \boldsymbol{A}(\sigma), \tag{31}$$

where **d** stands for the observed MT data, $\mathbf{Z}^{\text{obs}}$ and $\mathbf{W}^{\text{obs}}$; **A** is a forward modeling operator based on the contraction form of the integral equation (CIE) formulation (Hursán and Zhdanov, 2002) and MT transfer functions which are used to compute the undisturbed impedance $\mathbf{Z}^{\text{reg}}$ and the tipper vector **W**; matrix **c** contains components of the distortion matrix; and **σ** is a vector of the conductivity distribution within the modeling domain.

In order to solve Equation (29) and to find the conductivity distribution and the distortion matrix from the given observed MT impedances and tippers, we follow the standard procedure of Tikhonov regularization (Tikhonov and Arsenin, 1977; Zhdanov, 2002, 2015) based on minimization of the parametric (cost) functional,

$$P(\sigma, \boldsymbol{c}) = \|\boldsymbol{r}\|^2 + \alpha\|\boldsymbol{S}\|^2, \tag{32}$$

$$\boldsymbol{r} = \boldsymbol{W}_d(\boldsymbol{cA}(\sigma) - \boldsymbol{d}), \tag{33}$$

$$\boldsymbol{S} = \begin{bmatrix} \boldsymbol{S}_{\boldsymbol{\sigma}} \\ \boldsymbol{S}_{\boldsymbol{c}} \end{bmatrix} = \begin{bmatrix} \boldsymbol{D}(\sigma - \sigma_0) \\ (c - c_0) \end{bmatrix}, \tag{34}$$

where σ_0 is a vector of a reference conductivity model; $\mathbf{c}_0$ is a 2 X 2 identity matrix, corresponding to no distortion case; and **D** represents a matrix of the finite difference first derivative operator. Matrix $\mathbf{W}_d$ is a data weighting matrix. The data weights are computed based on the noise level (variance).

The stabilizing functional, **S**, consists of two parts: regularization for the conductivity distribution $\mathbf{S}_\sigma$, and regularization for the distortion matrix, $\mathbf{S}_c$. Similarly to Avdeeva et al. (2015), our study found that no additional coefficients were required for balancing the inputs of $\mathbf{S}_\sigma$ and $\mathbf{S}_c$ in the total stabilizing functional **S**. The regularization parameter α balances the effect of the misfit and stabilizer in the parametric functional.

We used the regularized Gauss-Newton (RGN) method in data space (Gribenko and Zhdanov 2017, Siripunvaraporn et al. 2005) to minimize the parametric functional (30). A conventional model space RGN method requires the inversion of the large square Hessian matrix, which is one of the main obstacles for using the RGN method in geophysical inversion. The data space implementation involves inversion of a much smaller matrix, which makes it possible to use the RGN method with limited computer resources. The two formulations are equivalent and yield identical solutions.

An application of the Gauss-Newton method requires calculation of the Fréchet derivative or sensitivity matrix, **F**. A straightforward calculation of the sensitivity matrix requires multiple additional forward modeling solutions. One of the advantages of using the CIE method as a forward modeling engine is that an approximate but accurate Fréchet derivative, **F**, with respect to the conductivity is readily available from the solution of the forward problem. This approximation of the Fréchet derivative is called a quasi-Born approximation (Gribenko and Zhdanov, 2007; Zhdanov, 2009) due to its similarity to the classical Born approximation, where instead of the total electric field, the background field is used. A chain rule is applied to obtain the Fréchet derivatives of the impedance and tipper components, once the derivatives of the EM field components are computed. The Fréchet derivative of impedances, $\mathbf{Z}_{\alpha\beta}$, with respect to the components of the distortion matrix, c_{ij}, can be obtained directly by differentiating equations (28):

$$\boldsymbol{F}_{c}^{\boldsymbol{Z}^{obs}} = \left[\boldsymbol{Z}_{\boldsymbol{\alpha\beta}}^{reg}\right], \tag{35}$$

DOI: 10.14750/ME.2022.008

3.4.2. Data preparation

The locations of the 24 available MT stations can be seen on Figure 5. The data of one station was rejected because of poor data quality. Thus, 23 stations were utilized for the inversion. The period range for different stations was similar, most of the stations contained data for periods between approximately 10 and 0.001 sec. 2 stations contained longer periods (100 s) data but were still included in the inversion. To clean the data we examined sounding curves and removed outliers as well as points with large data errors. This cleaned data was interpolated on a common set of periods from 10 to 0.01 sec. At least six values were kept in each decade.

3.4.3. Inversion results and interpretation

We applied the joint conductivity and distortion matrix inversion to the MT impedance and tipper data. The inversion domain was extended at approximately 1.9 km in the North-South direction and in 2.1 km the East-West direction. The horizontal cell size was selected at 25 m x 25 m. The vertical discretization consisted of 36 layers with the thickness increasing logarithmically from the surface to 7090 m. Total number of discretization cells was 229,824. The best RMS misfit of 1 was reached after the 6th iteration (Figure 11). As a starting model we used a best-fitting half-space model, which was obtained by averaging the MT sounding data over all stations. The error floor for the impedance was set to 5% and 0.05 for tipper.

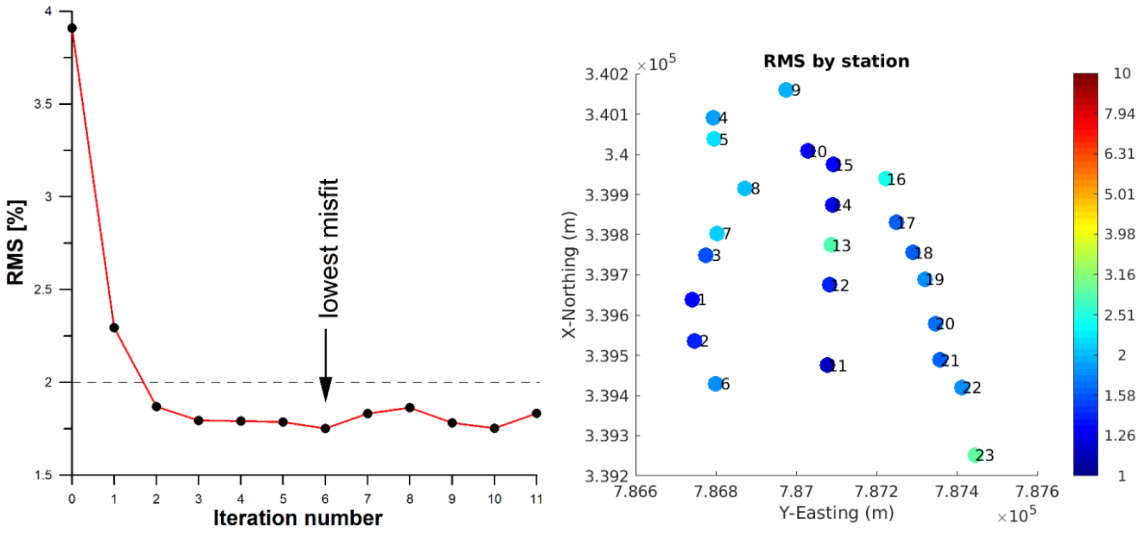

Figure 11. The RMS misfit values at the iteration steps (left) and the map of distribution of RMS by MT stations based on the inversion results (right).

DOI: 10.14750/ME.2022.008

Figure 12 shows horizontal sections of the resistivity model produced by 3D inversion at the depth from 250 m to 550 m. Two low resistivity feature can be identified inside the measurement area. The extension and position of them changes slightly with increasing depth. However, these low resistivity zones do not coincide with the ones provided by 2D inversion, they show similarities with each other. These anomalies may be caused by sulphide mineralization.

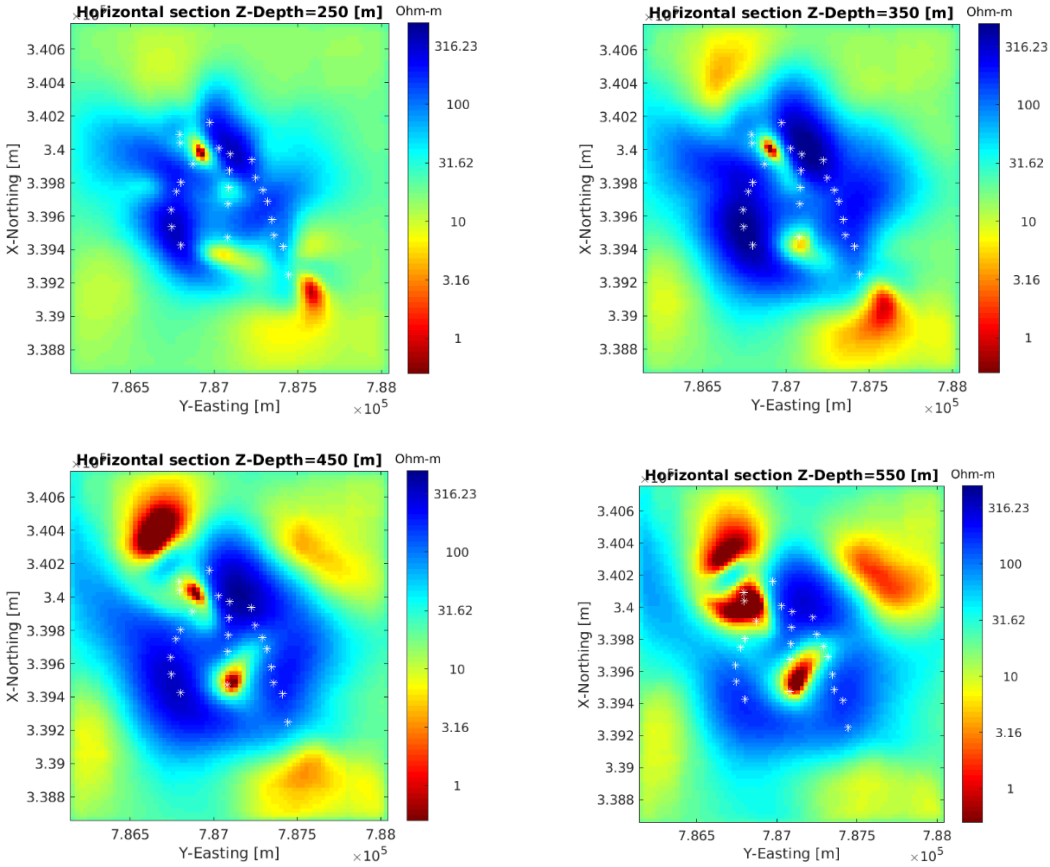

Figure 12. Horizontal slices of the recovered resistivity distribution from 250 to 550 m depth.

Summarizing the geophysical information about the Irota exploration area, a composite map has been compiled (Figure 13). The base map layer is a horizontal section of the resistivity calculated by 3D MT inversion to a depth of 550 m. This depth level is displayed because it is already certainly the range of the Paleozoic basement in most of the measurement area. Previously, the purpose of MT measurement was to detect conductive zones within a substrate. Warmer colors indicate lower, while colder colors indicate higher resistivity areas. It can be observed that two good conductive (low resistivity) zones also emerge. Two other similar zones can be seen in the NW and NE parts of the map, but they are outside the network of MT stations, so they can be considered less reliable inversion results.

Both zones are located in the area where a magnetic anomaly greater than 50 nT, this area is indicated by a blue dashed line. Isolated lines marked in a lighter color also show the value of the magnetic anomaly reduced to the pole.

The area bounded by a green solid line in the northern part of the map indicates a gravitational anomaly greater than 25 mGal. This gradually decreases towards the south, which is in line with the model that the Paleozoic basement becomes deeper and deeper to the south. The Neogene sediments covering the substrate can be characterized by a lower density.

The reflection seismic sections of Felsővadász-1 (FV-1) and Sze-1 and Sze-4 are also marked on the map, which extend far beyond the area but intersect near the FV-1 borehole. Based on Figure 13, FV-1 drilling cannot be found in the areas with the greatest magnetic or conductivity anomalies.

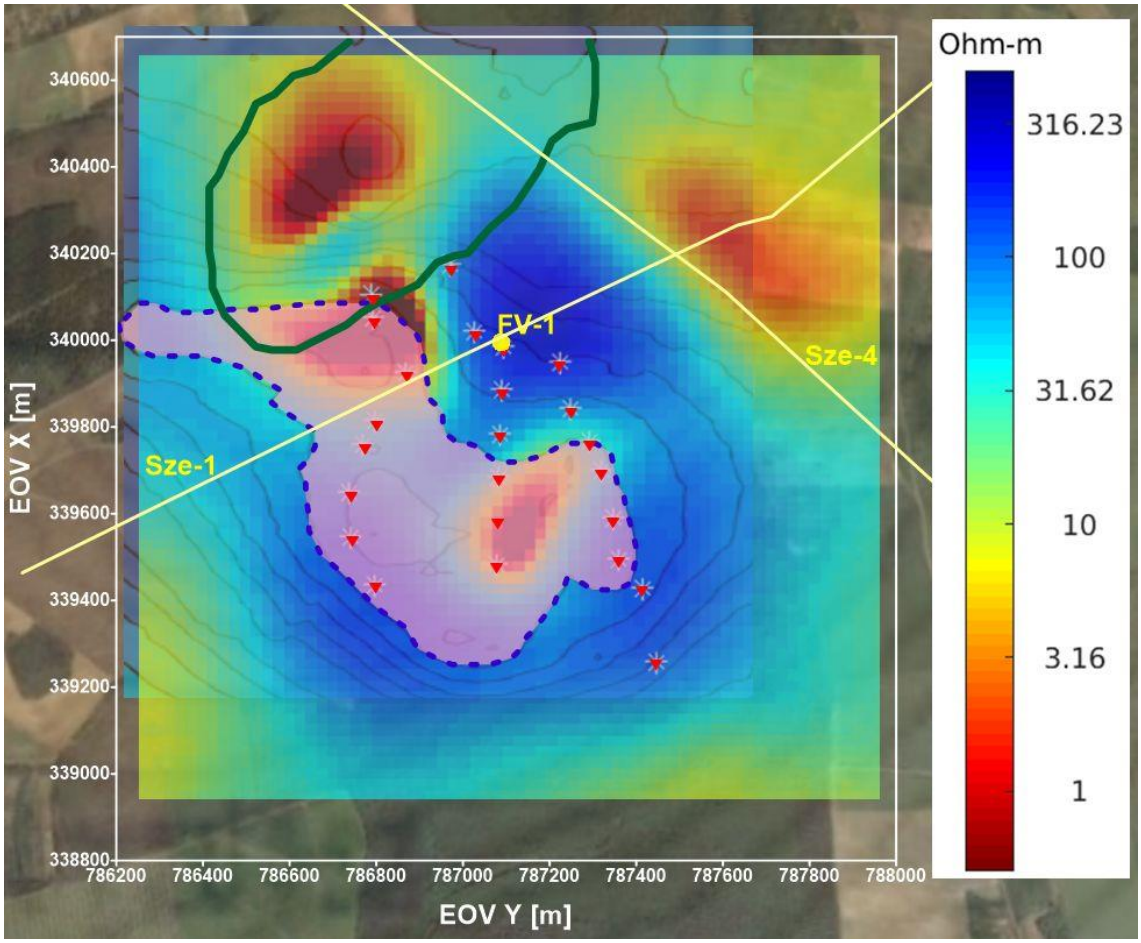

Figure 13. Satellite image of the Irota exploration area, with a resistivity obtained by 3D inversion in a horizontal section at a depth of 550 meters. The pink-colored area bounded by a blue dashed line on the magnetic map reduced to the pole indicates an anomaly greater than 50 nT. The green solid line delimits a gravitational anomaly greater than 26 mGal. The red

DOI: 10.14750/ME.2022.008

triangle shows the MT stations, the yellow circle shows the FV-1 borehole, and the yellow solid lines show the Sze-1 and Sze-4 reflection seismic profiles (Nádasi 2021).

Thesis 2.

I performed magnetotelluric (MT) measurements in the Cserehát, in the exploration area near Irota and Gadna settlements.

Thesis 2. a I have shown that under the MT-1 section, the Paleozoic basement gradually deepens to a depth of 200 m from the surface in the southern direction.

Thesis 2. b I have shown that below the Cserehát research area, between the depths of 200 m and -500 m, there is a conductive body with a resistivity of 4 Ωm, the horizontal extent of which is more than 200 m.

DOI: 10.14750/ME.2022.008

4. MT anisotropy study

Several researchers who studied geological and geophysical properties of the Western Superior province (part of the Canadian Shield) noticed the presence of anisotropy in the upper mantle (Craven et al. 2004, Musacchio et al. 2004, Percival et al. 2006). Conductivity models obtained by 2-D inversion of MT data manifested repeated patterns of conductive and resistive features in the upper mantle over a wide area in order to reproduce the large difference between long period XY and YX (J. Craven, personal communication, 2019). Musacchio et al. (2004) reported 8 % azimuthal V_p anisotropy (fast propagation normal to strike) in part of the lower crust and > 6 % azimuthal V_p anisotropy (fast propagation parallel to strike) in a 15–20 km thick layer in the upper mantle.

Before running 3D MT inversion (Chapter 5), I was searching for the evidences of conductivity anisotropy in this area. In order to do that, I made data analyses (Chapter 4.2) and anisotropy modeling (Chapter 4.3) which is presented in this chapter. The geological setting of the Western Superior region is summarized here. The location of the MT stations and the features of the dataset can be read in Chapter 5.1.

4.1. Geology of the Western Superior Region

The Superior Province, known as the nucleus of the North American continent, is the largest Archean craton of the Earth. Various types of rocks can be found there which formed and went through from low-grade to high-grade metamorphism during the Archean Eon (Whalen et al. 2003). Complex geological structure has developed during the tectonic evolution dominating with granite-greenstone and gneissic terranes. The geologic observations of the last decades have shown the elements of different orogenic processes, successive accretion of oceanic crust, island arcs, sedimentary prisms and continental fragments. The province can be divided into four separable units as Western Superior Region, the Central Superior Region, the Moyen-Nord Region and the Northeastern Superior Region (Percival et al. 2012). All regions can be divided into subprovinces based on differences in lithology, age, and metamorphic grade. The boundaries between these units can be faults and shear-zones, intrusive contrasts, uncomformities and discontinuities in metamorphic grade (Bedard and Harris 2014). In this chapter I focus on the Western Superior Region, which subprovinces are shown on Figure 14.

DOI: 10.14750/ME.2022.008

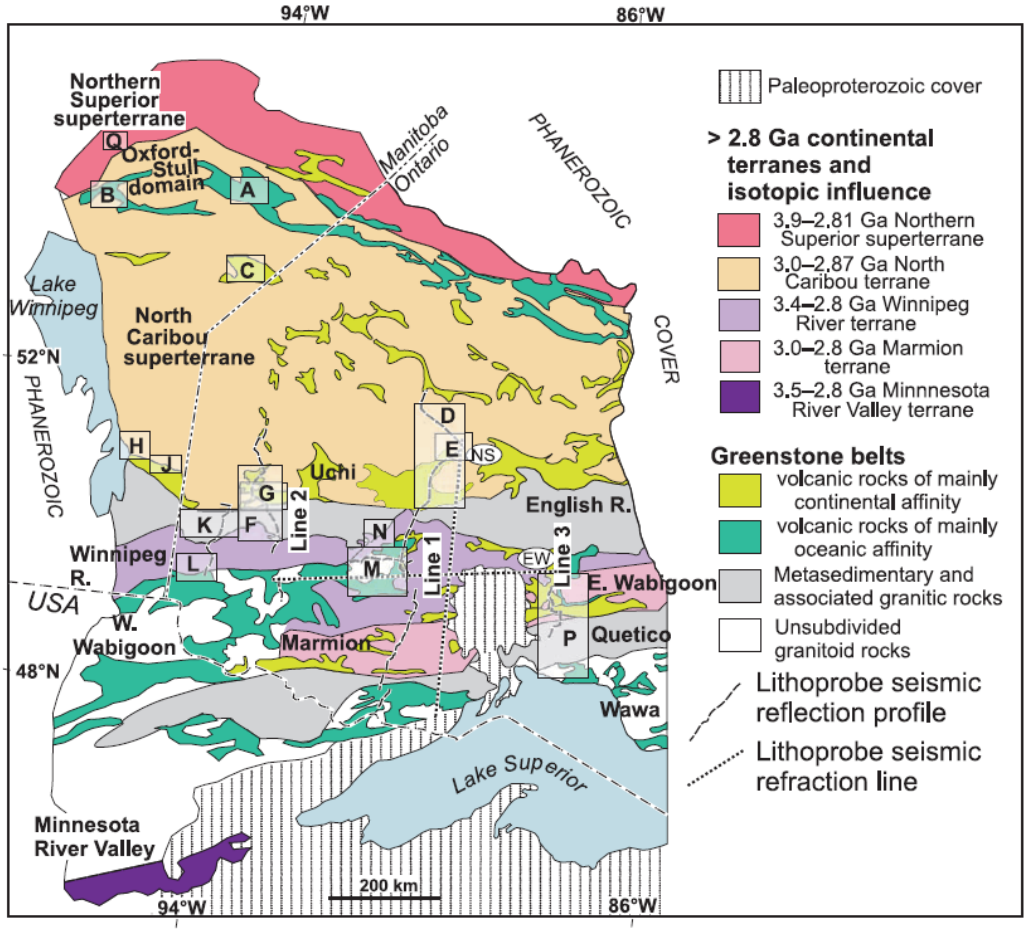

Figure 14. Geological map of the survey area (Percival et al. 2006).

4.2. Evidences of electric anisotropy in MT data

Difference between X- and Y- directed resistivities would manifest itself in different values of the observed MT apparent resistivities and phases of different observed MT impedance components. In the case of X-direction being more conductive XY apparent resistivity would be lower than YX apparent resistivity, and the opposite would be true for the corresponding phases. Apparent resistivities can be severely distorted by near-surface inhomogenities, while phases remain largely unaffected. For this reason, it is easier to compare the phases of the observed impedances in order to see any consistent differences, which may indicate anisotropy in X and Y directions. Figure 15 presents the maps of XY and YX observed phase differences at four different frequencies. It is clear from the plot that there are significant and consistent positive differences between XY and YX observed phases for the 0.001 and 0.01 Hz in central and South-West parts of the survey area. Similar differences were noted at other frequencies between 0.001 and 0.01 Hz. Larger XY phase indicates lower resistivity in X direction.

DOI: 10.14750/ME.2022.008

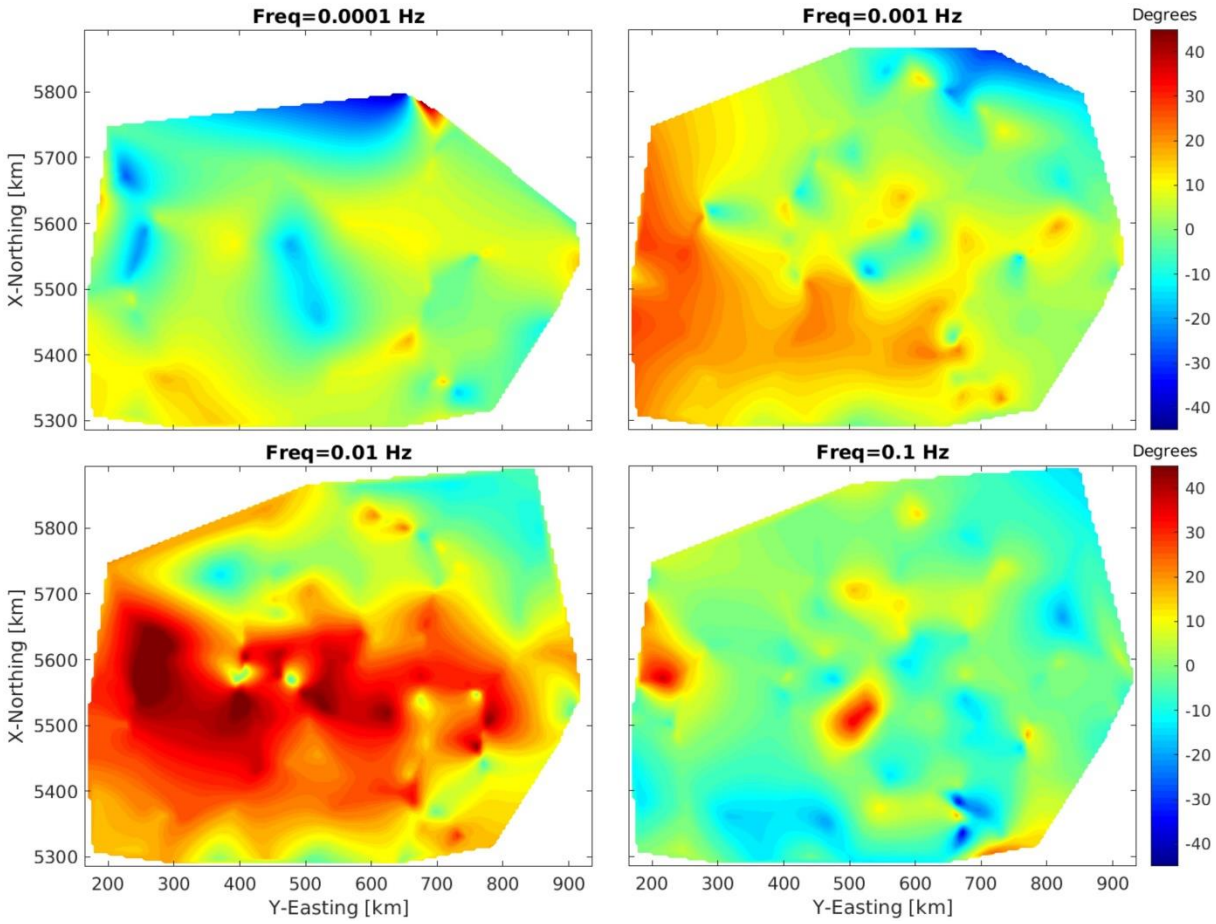

Figure 15. Maps of the phase differences between XY and YX components of the observed MT impedance. Four frequencies are shown. Consistently higher XY phase is observed in the central and South-West regions of the survey area for frequencies 0.001 and 0.01 Hz.

4.3. Anisotropic forward modeling

Our inversion code is not capable of producing models with anisotropic conductivities. We performed a synthetic study in order to understand what effect an anisotropic true model with different conductivities in X and Y directions may have on the inverse model with isotropic conductivity assumption. True model for which synthetic data were computed is shown in Figure 16. The model consists of an isotropic 1000 Ohm-m half-space with a conductive anisotropic layer between 100 and 200 km depth. The layer has lower resistivity of 10 Ohm-m in X (N-S) direction 100 Ohm-m in Y (E-W) direction. 25 receivers in a regular 100 x 100 km grid with 13 periods logarithmically spaced between 10,000 and 10 sec were modeled. Synthetic data were computed using a 3D finite element code (Cai et al. 2014), which allows arbitrary conductivity anisotropy.

DOI: 10.14750/ME.2022.008

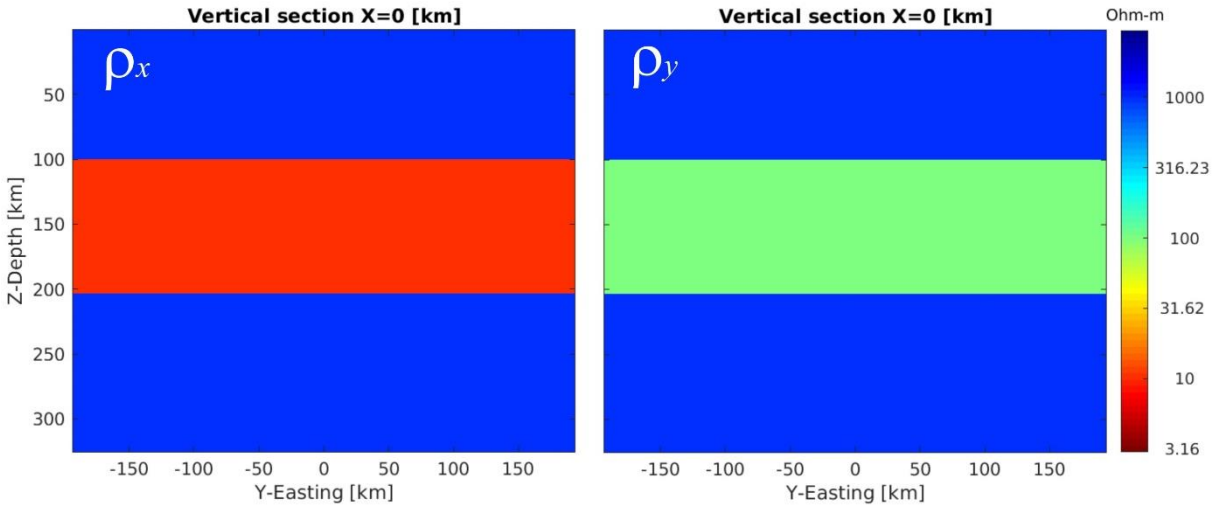

Figure 16. Vertical sections of the true anisotropic model X-directed resistivity is shown on the left, and Y-directed resistivity on the right.

The synthetic data was inverted for an isotropic resistivity model. The convergence ceased at a relatively high RMS of 1.9 for a synthetic data set. Figure 17 shows plots of the observed and predicted data for one of the stations. Poor data fit is observed for the diagonal impedance components XX and YY, and longer periods of the XY component.

DOI: 10.14750/ME.2022.008

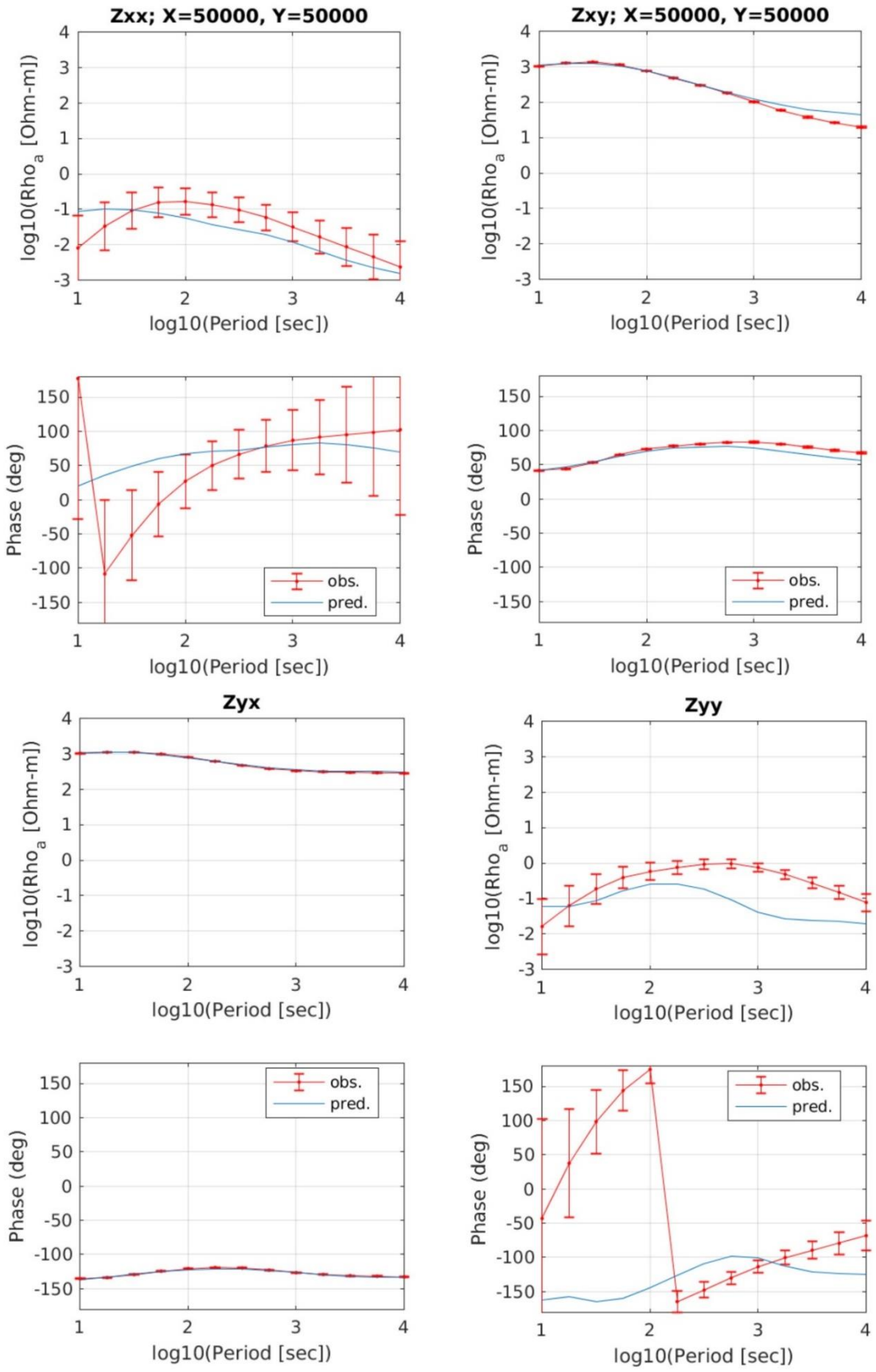

Figure 17. Observed and predicted fields for the synthetic anisotropy model.

DOI: 10.14750/ME.2022.008

Figure 18 shows horizontal and vertical sections of the isotropic resistivity model recovered by our inversion. Resistivity distribution shows interchanging conductive and resistive features elongated in X (N-S) direction. The inversion placed such features in an effort to reproduce true anisotropic model with resistivity lower in X (N-S) direction. The depth range of the observed features coincides with the true depth range of the anisotropic layer in the true model. Strong anomalies appear outside of the lateral extent of the survey layout. Similar effects were observed by several researchers and reviewed by Wannamaker (2005).

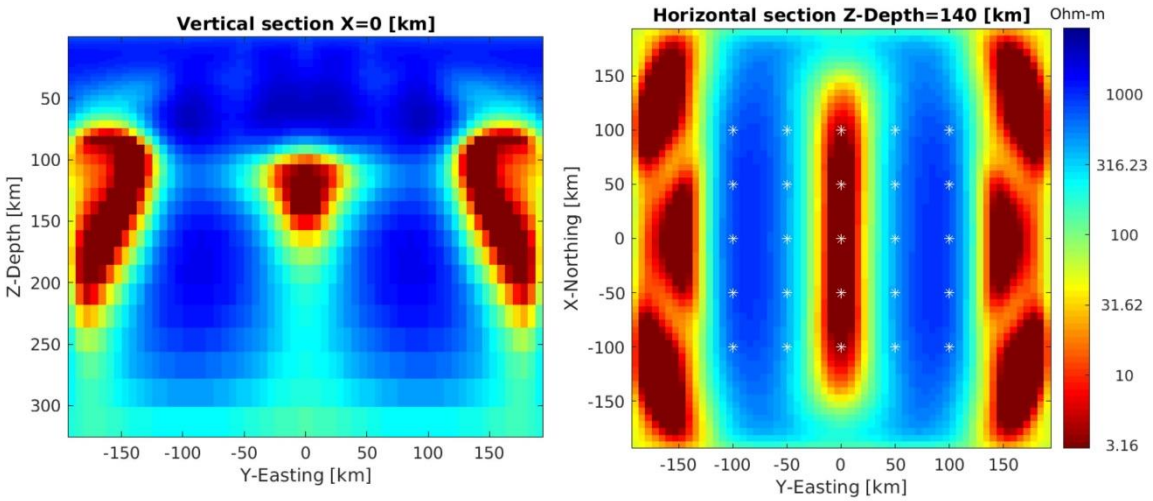

Figure 18. Vertical (left) and horizontal (right) sections of the isotropic resistivity distribution recovered by the inversion.

Thesis 3.

I calculated the phase differences between XY and YX components of the observed MT impedance. I pointed out consistently higher XY phase in the central and South-West regions of the survey area for frequencies 0.001 and 0.01 Hz. This indicates higher conductivity in the North-South direction which proves the presence of conductivity anisotropy.

DOI: 10.14750/ME.2022.008

5. 3D inversion of large-scale MT data

The Western Superior region is part of the Canadian shield and is located north from the Superior Lake. The area has huge economic significance because several gold and base metal mineral deposits can be found there. Magnetotellurics is a useful tool to investigate the deep structure of the craton and find geological connections with the existing ore deposits. In this chapter I present the results of MT inversion of a subset of Lithoprobe and EartScope MT data collection covering this region. The regularized Gauss-Newton method was used applying data-space implementation. The algorithm inverts the full MT impedance and tipper data simultaneously. Based on the results, some well conductive zones were identified. Recovered 3D conductivity model was compared with known tectonic structures, earlier geoelectric studies and seismic measurements.

The Lithoprobe project was a huge regional geophysical and geological research program and was supported by the Natural Sciences and Engineering Research Council, Canada. It covered ten specified transects in Canada, one of them is the Western Superior Region situated in western Ontario. The main goal of the project was to broaden knowledge of the structure of the crust and lithosphere. As part of the Lithoprobe project significant amount of MT data were collected. Besides MT surveys seismic reflection and refraction and teleseismic experiments were performed. In our target area, in the Western Superior Region, the MT data were collected between 1997 and 2000. These data were supplemented by Earth Scope US Array data from northern Minnesota, which were registered between 2011 and 2013 as part of the Mid-Continent Rift subproject. The observed MT data were processed and archived by IRIS (Incorporated Research Institutions for Seismology) and can be accessed via IRIS webpage (http://ds.iris.edu/spud/emtf). The results of 3D inversion of these MT data system are presented in this chapter.

Many papers dealt with the geoelectric structure of the Western Superior Province. The evaluation and interpretation of MT data can be found detailed in Ferguson et al. (2005). According to their study, the crust of the North Caribou terrane is more resistive than adjacent crust elements of the province. Based on the induction arrows they described a 600 km long west-east directional linear conductive anomaly at the southern margin of the North Caribou terrane. It can be interpreted as the metasedimentary rocks of the English River subprovince.

An interpretation of 3D MT inversion is presented by Roots and Craven (2017). They pointed out more conductivity anomalies than the previous interpretations. They found that the

DOI: 10.14750/ME.2022.008

mantle lithosphere beneath the North Caribou terrane is relatively conductive. However, the existence of the 600 km long anomaly (Ferguson et al. 2005) at its southern margin was not proved. They inverted the data from 110 sites, which are approximately the half of the available MT data in the Western Superior Region.

Seismic studies showed that the Western Superior Province is thicker than other Archean crusts (Kendall et al. 2002). Another characteristics of the province are the long uninterrupted geological belts, which are not common in case of other Archean cratons.

5.1. Data preparation

The MT data from a total of 180 MT stations were downloaded from the Incorporated Research Institutions for Seismology (IRIS) website http://ds.iris.edu/spud/emtf (last accessed on 03/07/2019). The data covered a part of the Ontario and Manitoba provinces of Canada, as well as US states Minnesota and North Dakota. The map of the study area is shown in Figure 19. Two projects contributed to the data set which I used in this chapter - LITHOPROBE and EarthScope. LITHOPROBE was a Canadian major national research project in the earth sciences. It combined multidisciplinary earth science studies of the Canadian landmass and surrounding offshore margins to determine how the northern North American continent has formed over geological time. EarthScope is a program of the National Science Foundation (NSF) that has deployed thousands of seismic, GPS, MT, and other geophysical instruments to study the structure and evolution of the North American continent and the processes that cause earthquakes and volcanic eruptions.

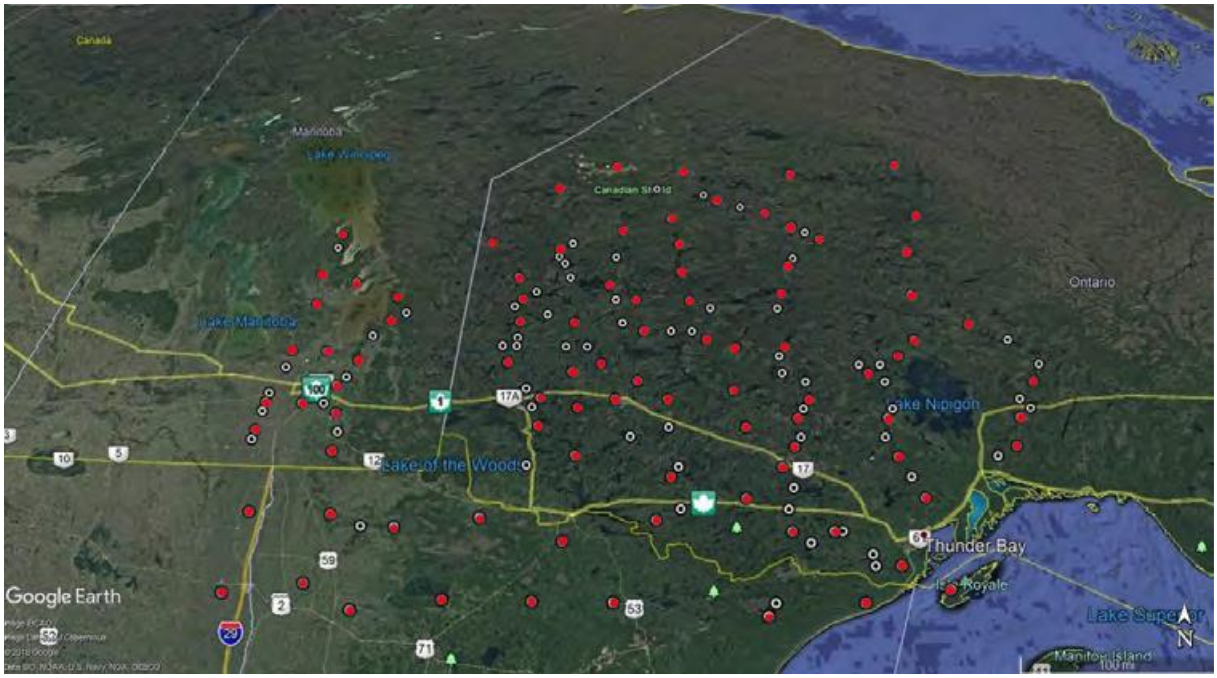

DOI: 10.14750/ME.2022.008

Figure 19. Map of the area covered by the data set used in this chapter. The locations of all available MT stations are shown by white circles and red dots. The locations of the selected MT stations used in 3D inversion are indicated by red dots.

As seen from the map in Figure 19, the spacings between MT stations are quite irregular. Due to the regional character of the investigation, 88 MT stations were rejected due to a proximity to another stations with wider period range or better data quality. In order to ensure a relatively uniform coverage of the area of investigation, we have required the minimum distance between the MT stations of about 30 km. As a result, 92 MT stations were selected for 3D inversion, 79 from LITHOPROBE project and 13 from EarthScope data base. The locations of the selected MT stations are indicated in Figure 19 by red dots. The period range for different stations varied; however, most of the stations contained the MT data for periods between approximately 4 and 10,000 sec. The pre-processing of the data involved a careful examination of the MT sounding curves and removal of the outliers and the points with the large data errors. The processed cleaned data were interpolated on the same set of periods for all stations. The range of periods extended from 10 to 10,000 sec. These periods were equaly-spaced in logarithmic space with 6 periods per decade. Figures 20 through 22 show examples of the original, pre-processed (cleaned), and interpolated principal impedances, auxiliary impedances, and tipper data for one of the stations.

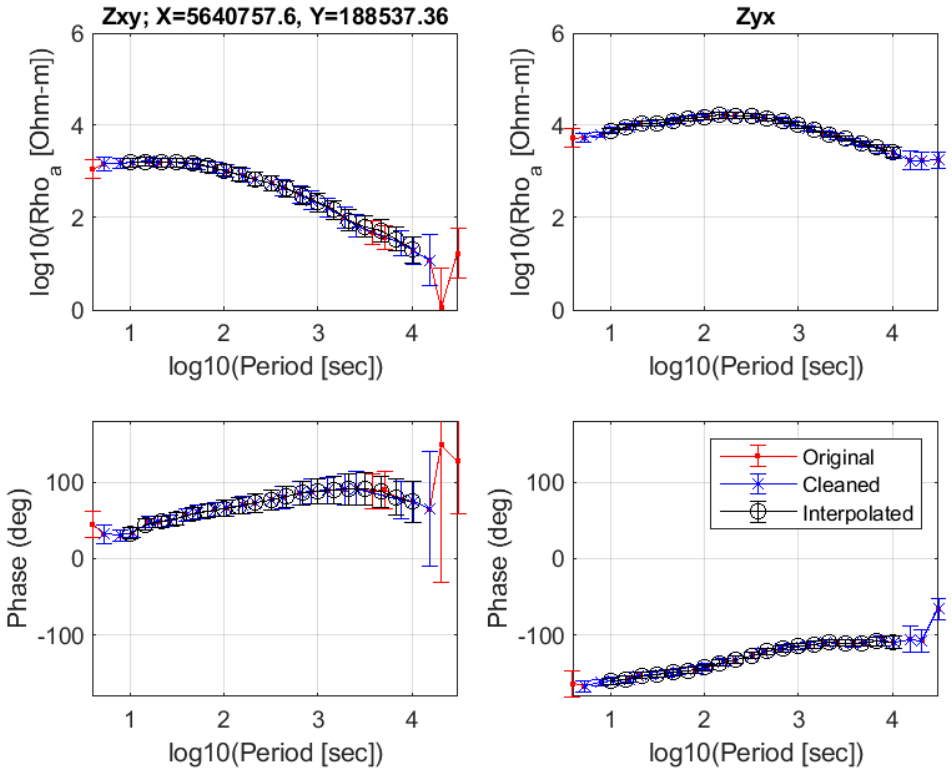

DOI: 10.14750/ME.2022.008

Figure 20. Example of the observed, cleaned, and interpolated principal impedance data for one of the stations. The top panels show apparent resistivities, while the bottom panels present phases. The left panels correspond to XY components of the data, and right panels represent the YX components.

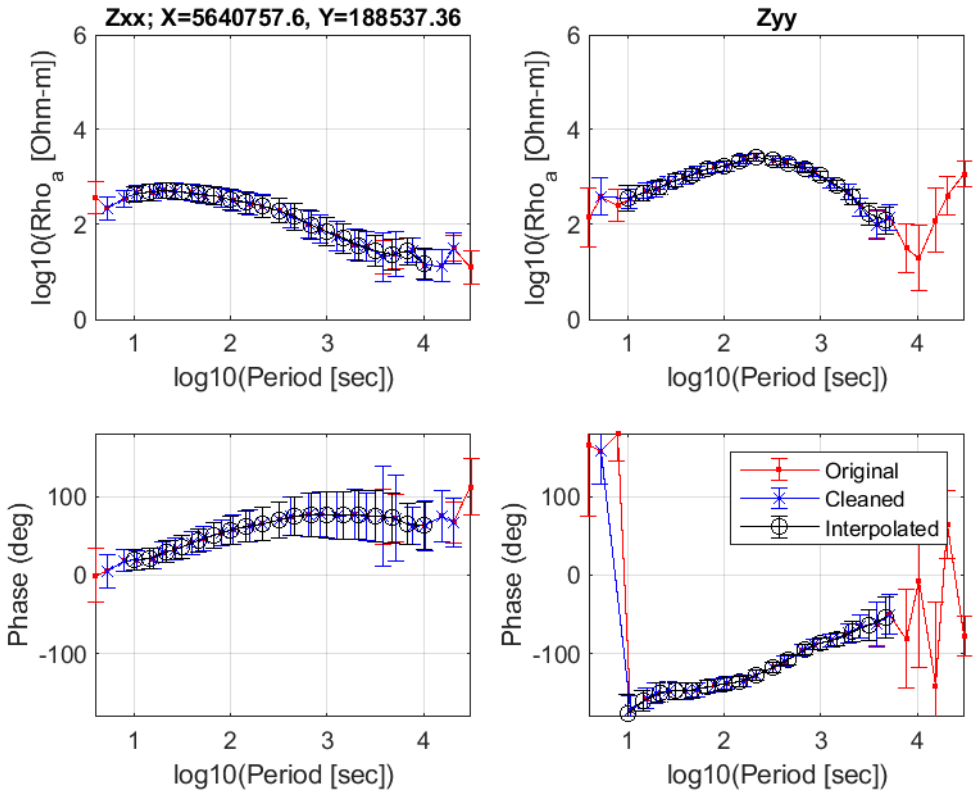

Figure 21. Example of the observed, cleaned, and interpolated auxiliary impedance data for one of the stations. The top panels show apparent resistivities, while the bottom panels present phases. The left panels correspond to XX components of the data, and right panels represent the YY components.

DOI: 10.14750/ME.2022.008

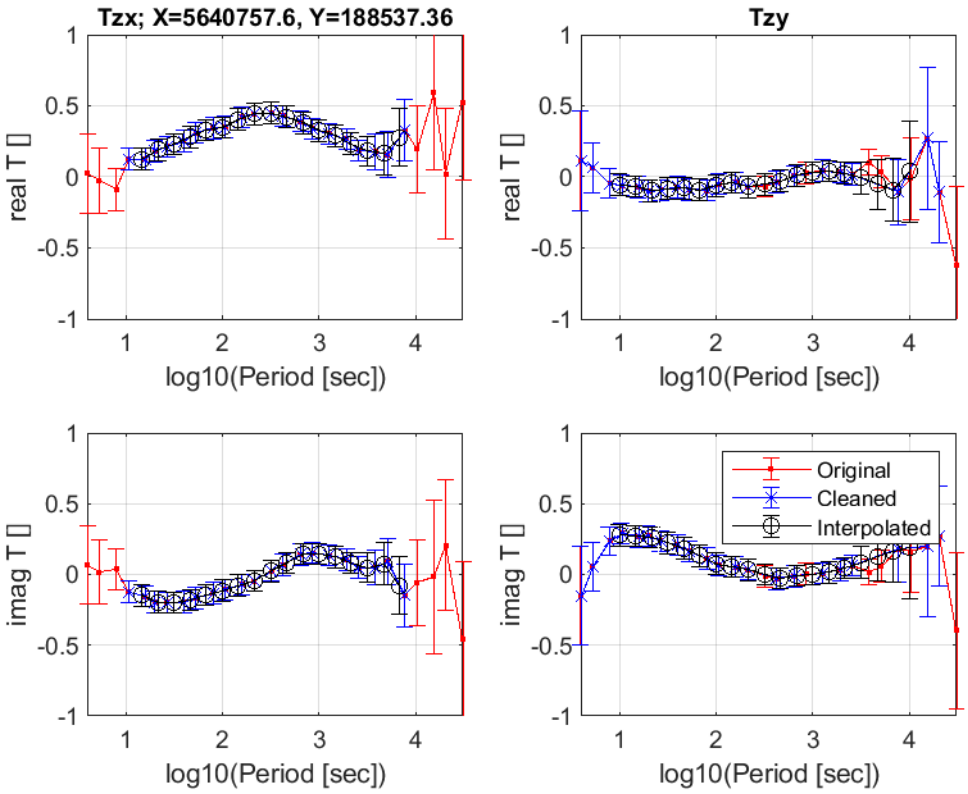

Figure 22. Example of the observed, cleaned, and interpolated tipper data for one of the stations. The top panels show real parts of the tipper, while the bottom panels present imaginary parts. The left panels correspond to ZX components of the data, and right panels represent the ZY components.

5.2. Sensitivity domain selection

In order to reduce memory requirements, we employ a method of moving sensitivity domain described by Cox et al. (2010) and Čuma et al. (2017). The method is based on a simple concept that the sensitivity of the data for a particular MT station decreases with the distance from the station. The rate of this decrease is inversely proportional to the period of the observed data. For the long periods, the sensitivity attenuates relatively slow, while for the short periods the sensitivity decays rapidly with the distance. It was demonstrated in Čuma et al. (2017) that the size of the sensitivity domain can be determined based on the skin depth of MT field for each particular station and specific period. The skin distance for the shortest period of 10 s for an average resistivity of 1,000 Ohm-m is on the order of 50 km. The skin depth for the longest period of 10,000 s is significantly larger at approximately 1,600 km. According to Čuma et al. (2017), we only compute the Fréchet derivative matrix within a volume limited in horizontal and vertical directions by a single skin depth from a particular station at every period. For this

DOI: 10.14750/ME.2022.008

particular problem, if single skin depth is used, the size of the sensitivity domain for the shortest period is on the order of 1/800 of the total size of the inversion domain. The sensitivity domain grows with the period, and for the periods of 1,000 s and above the sensitivity region covers the entire inversion domain. Using the variable sensitivity domain approach, outlined above, we were able to reduce computer memory requirements by more than 60%.

5.3. Inversion results

At the first stage of the inversion, we have run 1D inversion of the MT souding curves produced by averaging the observed MT data over all stations. The resulting 1D conductivity model was used as a starting model for 3D inversion of the entire MT dataset. Figure 23 shows this layered earth model along with the observed and predicted data used for 1D inversion.

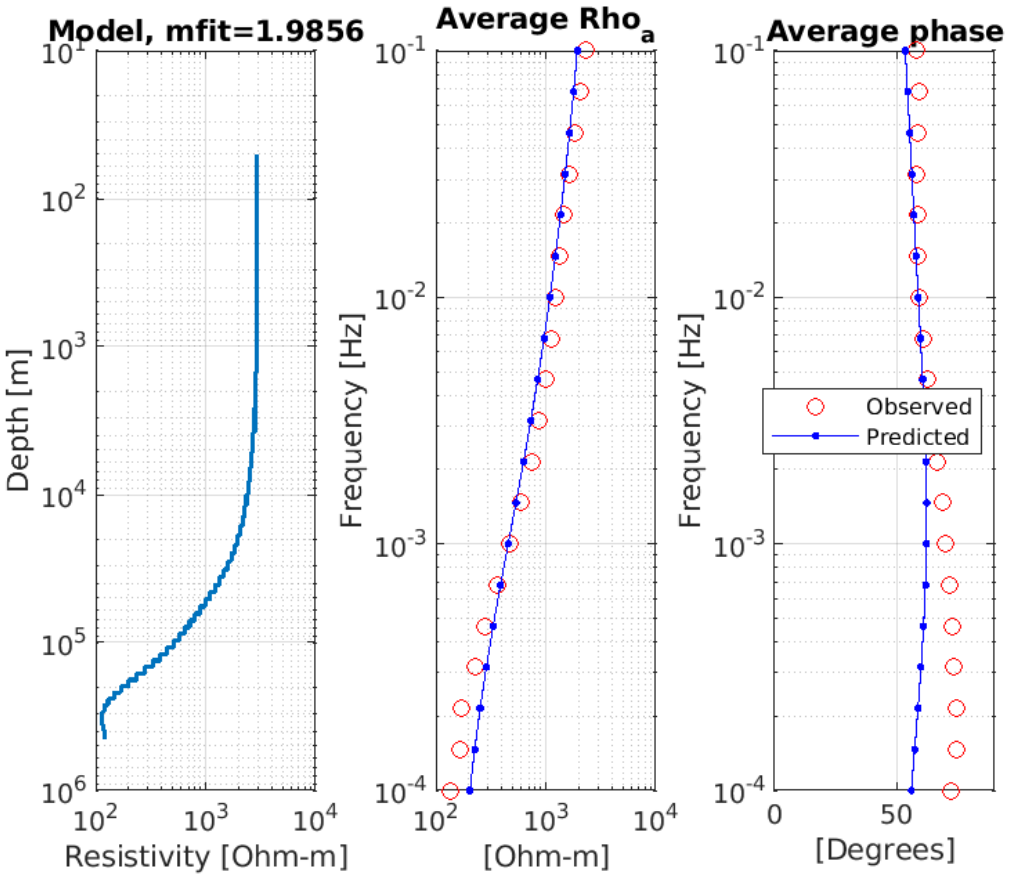

Figure 23. Result of 1D inversion of the MT sounding curves produced by averaging the observed MT data over all stations.

We applied 3D joint conductivity and distortion matrix inversion to the MT impedance and tipper data simultaneously. The inversion domain was extended at approximately 930 km in the North-South direction and in 1,157 km in the East- West direction. The horizontal cell

DOI: 10.14750/ME.2022.008

size was selected at 11.3 × 11.3 km^2. The vertical discretization consisted of 40 layers with the thickness increasing logarithmically from 1 to 40 km. The total number of discretization cells was 334,560.

The error floors were set to 7.5% for the impedance and 0.075 for the tipper. The 3D RGN inversion was run for 33 iterations until nRMS misfit reached 2.24. The nRMS was computed by the following formulas:

$$\boldsymbol{r_k = W_d(A(m_k) - d), nRMS = \sqrt{\frac{r_k^* r_k}{N_d}}}, \quad (36)$$

where A(m_k) is the vector of the predicted data at iteration number k, d is the vector of the observed data, N_d is the total number of data entries, and superscript "*" indicates a transposed complex conjugate vector. We have presented a map of the data fit (nRMS) over the survey area in different MT stations in Figure 24. One can see that, for majority of the stations the data fit is within an acceptable value of nRMS < 2.

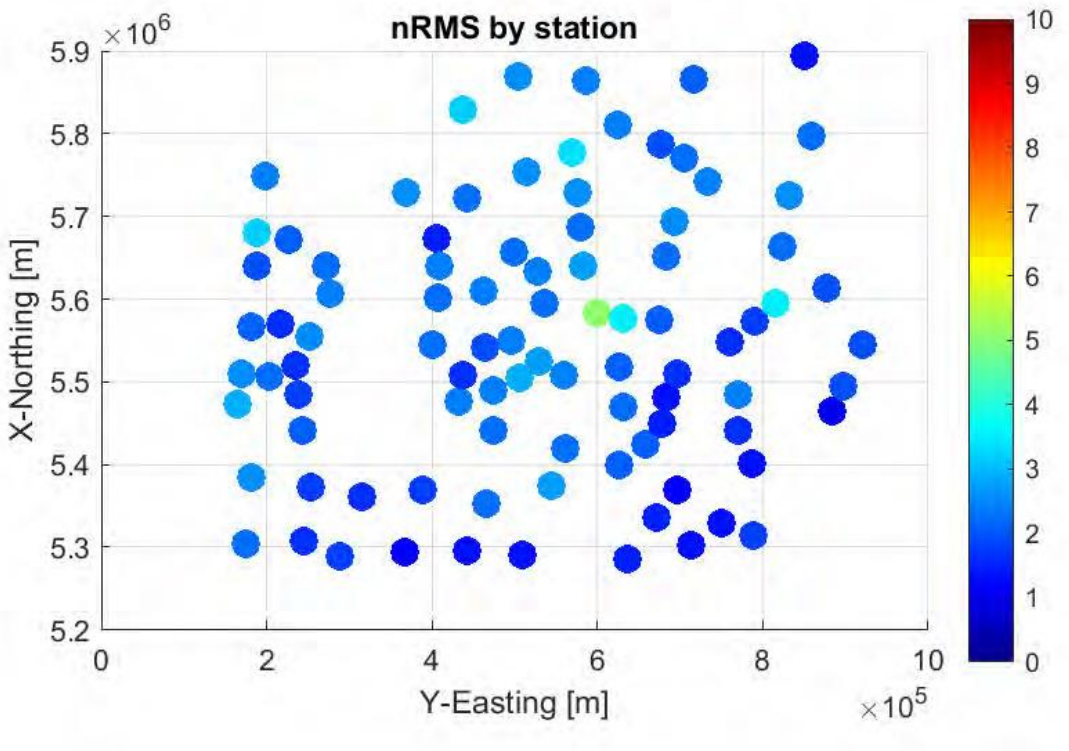

Figure 24. Map of distribution of nRMS by MT stations based on the results of simultaneous inversion for 3D conductivity distribution and the distortion matrix.

DOI: 10.14750/ME.2022.008

Figure 25 shows horizontal sections of the resistivity model produced by 3D inversion at the depths from 60 km till 380 km. In general, resistivity is relatively high to the depth of approximately 150 km, with more conductive material present at a greater depth. We have identified four prominent conductive features in the inverse resistivity model - C_d, C_1, C_2, and C_3. The deepest conductor, C_d appears below the depth of 350 km, and extends in W-E direction. The conductive features C_1, C_2, and C_3 are apparently originated from the deep conductor C_d and extended up to at least 150 km depth. These features are quite narrow and extend in the S-N direction. One interpretation of C_1- C_3 conductors could be the rise of hot conductive material from the deep mantle through the fractured zones in the extended upper mantle.

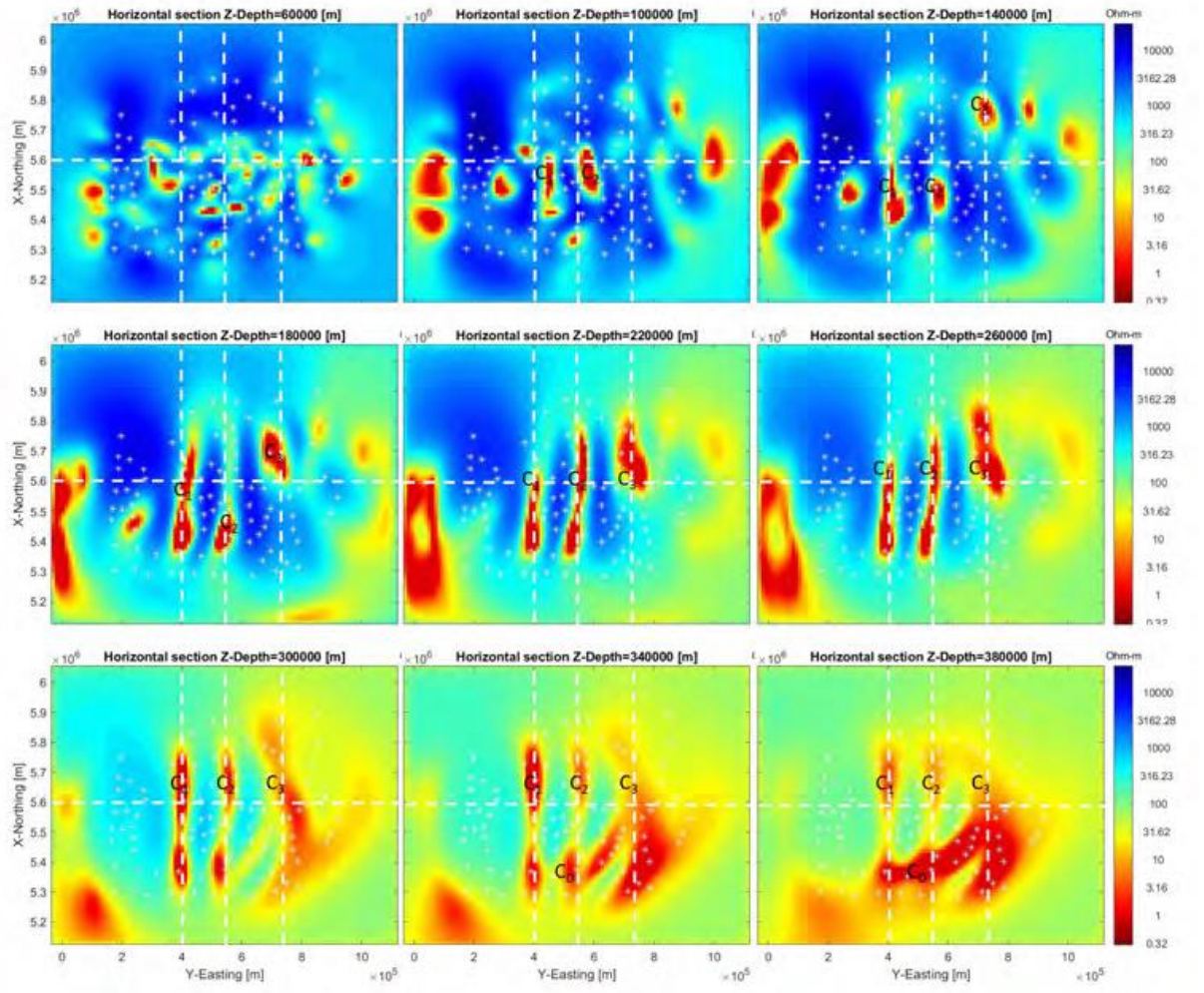

Figure 25. Horizontal sections of the recovered resistivity distribution from 60 to 380 km. Dashed lines indicate locations of the vertical sections of the inversion result. Four conductive features are labeled by C_d, C_1, C_2 and C_3.

DOI: 10.14750/ME.2022.008

Another possibility for such features is the apparent anisotropy of the upper mantle conductivity. Interchanging conductive and resistive features elongated in X (N-S) direction could be placed by the inversion in an effort to reproduce the actual anisotropic model with a low resistivity in the X (N-S) direction. Similar effects were observed and reviewed by Wannamaker (2005). Several researchers who studied geological and geophysical properties of the Western Superior province noticed the presence of anisotropy in the upper mantle (Craven et al. 2004, Musacchio et al. 2004, Percival et al. 2006).

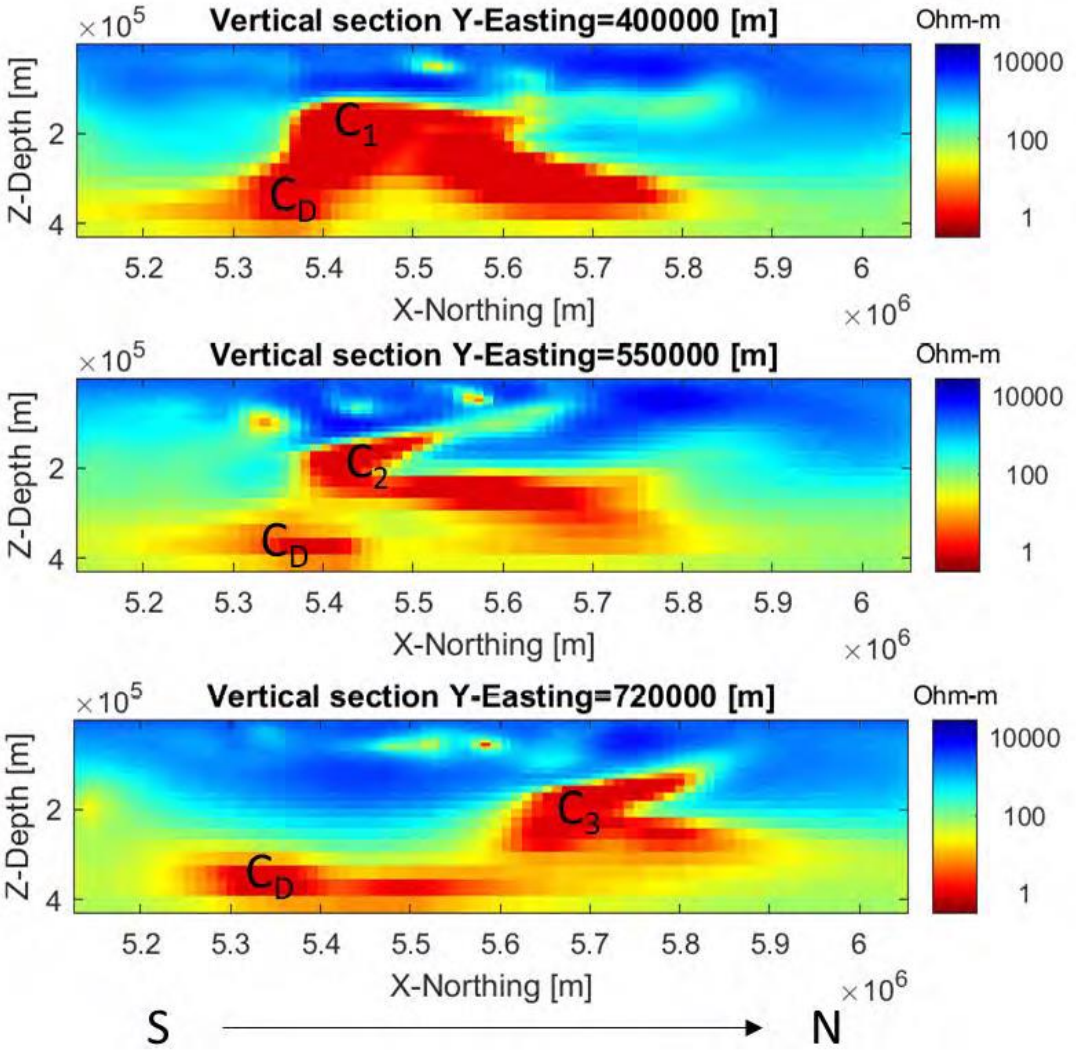

Figure 26. S-N vertical sections of inverse resistivity model along the profiles located at 400 km Easting (top panel), 550 km Easting (middle panel), and 720 km Easting (bottom panel).

In order to further examine aforementioned conductive features, we present the S-N vertical sections of the resistivity distribution in Figure 26. Locations of the vertical sections are shown in Figure 25 by white vertical dashed lines. All three conductors, C_1, C_2, and C_3

DOI: 10.14750/ME.2022.008

extend from approximately 100 km to 300 km depths. All conductors are approximately 500 km wide at the bottom. C_1 is the widest at the top, while C_2 and C_3 become thinner with the tops located towards the south of the section for C_2, and to the North for C_3. We suggest that these recovered relatively thin quasi-vertical conductive anomalies may represent the zones of partially melted material rising through the upper mantle (Gribenko et al 2021).

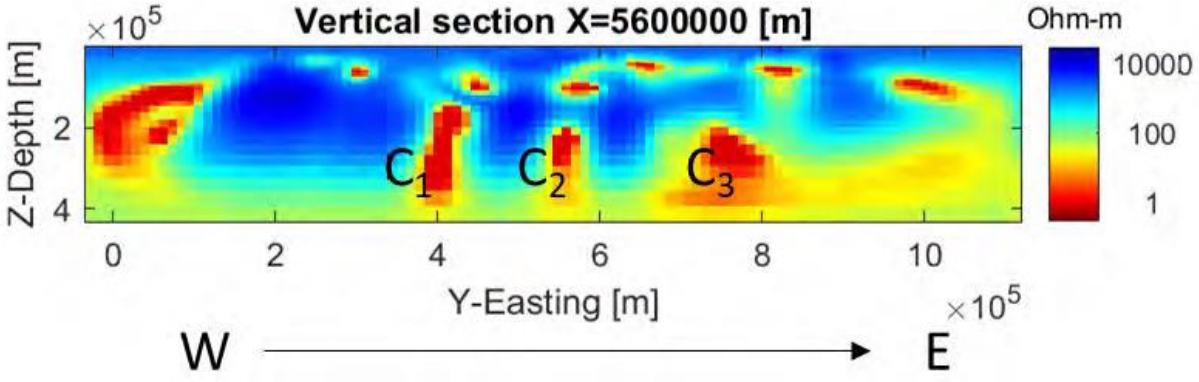

Figure 27. W-E vertical section of inverse resistivity model along a profile located at 5,600 km Northing.

Figure 27 presents the W-E vertical section at 5,600 km Northing (along the horizontal white dashed line shown in Figure 25). All three conductors are nearly vertical at the bottom with a slight westerly strike at the top. Series of shallow conductors are also visible above 100 km depth. There is a possible connection between C_1, C_1, and C_3 and these shallow conductors. I have applied the data-based RGN method for the 3D inversion of the MT data from the Western Superior region, collected by Lithoprobe and Earth- Scope projects. The results of inversion demonstrate that, inclusion of the distortion matrix provides superior data fit and recovers conductivity anomalies with greater details. A deep conductivity anomaly has been identified below 300 km depth. Three elongated conductive features are in the subsurface between 100 and 300 km depth. These anomalies can be interpreted as ascending conductive material of the mantle through the fractures of the upper mantle. They can be evidences of apparent anisotropy of the upper mantle conductivity.

Thesis 4.

In the Western Superior region, between a depth of 100 km and 300 km, I detected three conduction anomalies extended in a north-south direction, confirming the existence of the presumed deep electrical anomaly.

DOI: 10.14750/ME.2022.008

6. New approach of the EM parameter dependency of GPR measurements

6.1. Parameter differences between dielectric and lossy medium

In many cases, the knowledge of the exact response of the examined medium is not necessary. The use of the equations for dielectric can be enough when measuring in very high resistivity (ρ>100 Ωm) environment. But sometimes a complex interpretation of three-dimensional EM parameter distribution is needed, such as in the case of soils, where the resistivity can be lower, or in utility mapping, where accurate depth estimation is indispensable. This way, the precise interpretation of GPR data can have financial significance as well.

The dielectric approximation is reasonable in many cases, but the application of the equations for lossy media can facilitate the prediction of the frequency dependent EM parameters of a soil and can be useful in accurate velocity and depth estimation.

The basic idea of this chapter was to compare the calculated GPR parameters using equations for dielectrics and lossy media (see the equations in Chapter 1.3). The calculated parameters were plotted in the function of conductivity and were edited in MATLAB. In the next subchapters, six GPR parameters (wave propagation velocity, wavelength, vertical and horizontal resolution, skin depth, reflection depth) were investigated. Error quantities were introduced in order to highlight the deviation between the dielectric approximation and the real lossy medium.

Because the GPR instrument (constructed by MALA) of the Department of Geophysics at the University of Miskolc has three shielded antennas with frequencies of 100 MHz, 500 MHz and 1.2 GHz, the parameters were calculated and graphed systematically at these frequency values. Thus, the theoretical calculations can be tested with real GPR data.

The study of Thomas et al. (2006) deals with the soil response complexity and mention the conductivity dependence of EM wave velocity. In the following, I will give a full review of conductivity dependence of the most important GPR parameters.

6.1.1. Wave propagation velocity

The EM wave propagation velocities were calculated and plotted for the three antenna frequencies (100 MHz, 500 MHz and 1.2 GHz) belonging to the MALA georadar instrument of the Department of Geophysics of the University of Miskolc (Figure 28). They were displayed on a semi-logarithmic scale as a function of specific conductivity. The curves shown in the same color indicate the propagation velocity characteristics for six different relative dielectric constants (ε_r = 1; 5; 10; 20; 40; 80). The blue solid line shows the values for the lossy medium

DOI: 10.14750/ME.2022.008

(v_l) and the red dashed line shows the constant velocities (v_d) calculated for the dielectric. The latter do not depend on the specific conductivity.

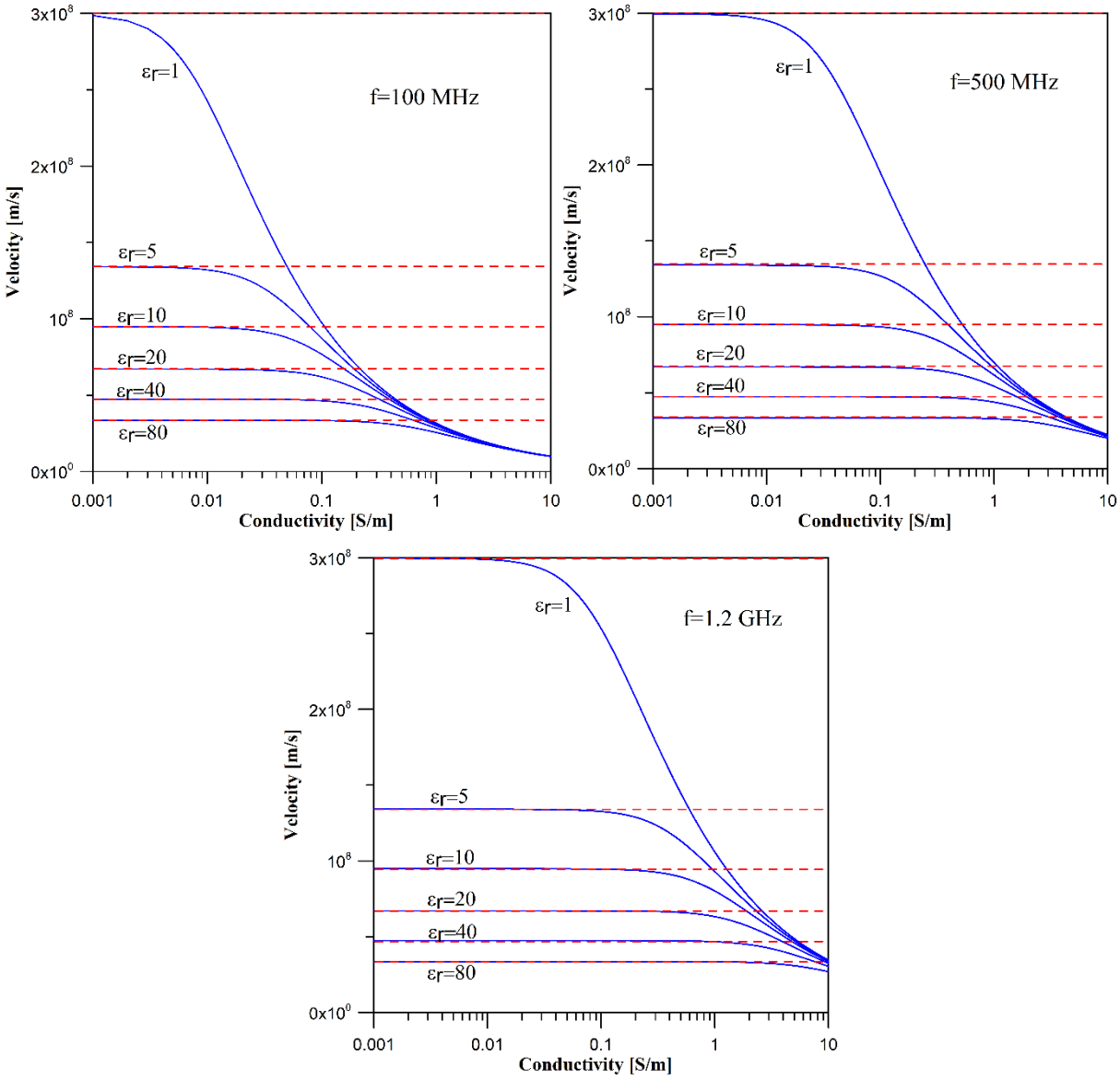

Figure 28. Comparison of wave propagation velocities in case of lossy medium (blue) and dielectric (red dashed) at 100 MHz, 500 MHz and 1.2 GHz.

In order to show the differences not only visually, I introduced an error-like quantity, which characterizes the magnitude of the difference between the values calculated on the basis of the two velocity definitions. Since in practice we would always have to calculate the propagation velocity of radar waves with the relation (20) for lossy media, let us examine what relative deviation (called relative error, denoted by H) is obtained by using the relation (19) for the dielectric to determine the propagation velocity:

DOI: 10.14750/ME.2022.008

$$H = \frac{v_d - v_v}{v_v} \cdot 100\ [\%]. \tag{37}$$

Figures 29 shows the error curves calculated from equation (37) as a function of specific conductivity in a log-log scale coordinate system for the three frequencies.

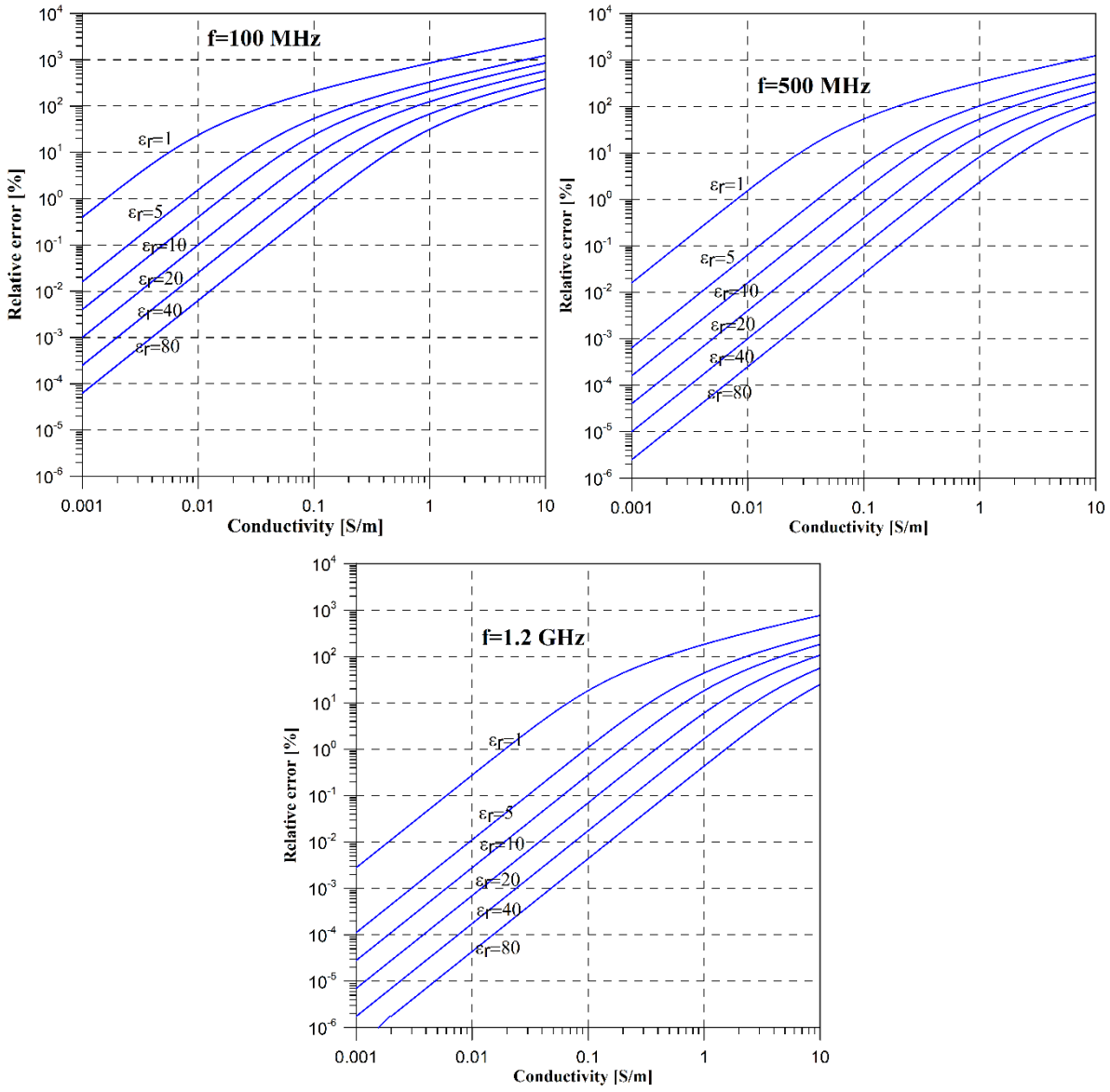

Figure 29. The relative difference between propagation velocities calculated for lossy medium and dielectric, in case of three frequencies.

It can be observed that with a constant increase in dielectric, the relative deviations decrease, regardless of the specific conductivity. As the frequency increases, the differences also become smaller. Furthermore, it is important to mention that as the conductivity increases (the resistivity decreases), the relative error increases. Assuming that our medium has an

DOI: 10.14750/ME.2022.008

average dielectric constant of at least $\varepsilon_r = 5$ and a resistivity above 100 Ωm, the relative error is below 2%. Examining the other extreme, i.e. the high conductivities ($\sigma > 0.05$ S / m), it can be stated that the relative error can be several hundred percent.

As the georadar method cannot be used effectively below a resistivity of 10 Ωm, it is worthwhile to deal in more detail with the range between 10 and 100 Ωm, where significant differences still occur, especially at 100 MHz. This is also significant from a practical point of view, as the majority of soils can be characterized by resistivity in this range. Figure 30 shows the error dependence of this range in a linear scale coordinate system at 100 MHz. It can be read from the figure that for $\varepsilon_r < 15$ and $\sigma > 0.082$ ($\rho > 12$ ohms) the relative deviation is always above 10%. If $\varepsilon_r = 10$, then the relative deviation is above 20%, while in the case of $\varepsilon_r = 5$ it already exceeds 45%.

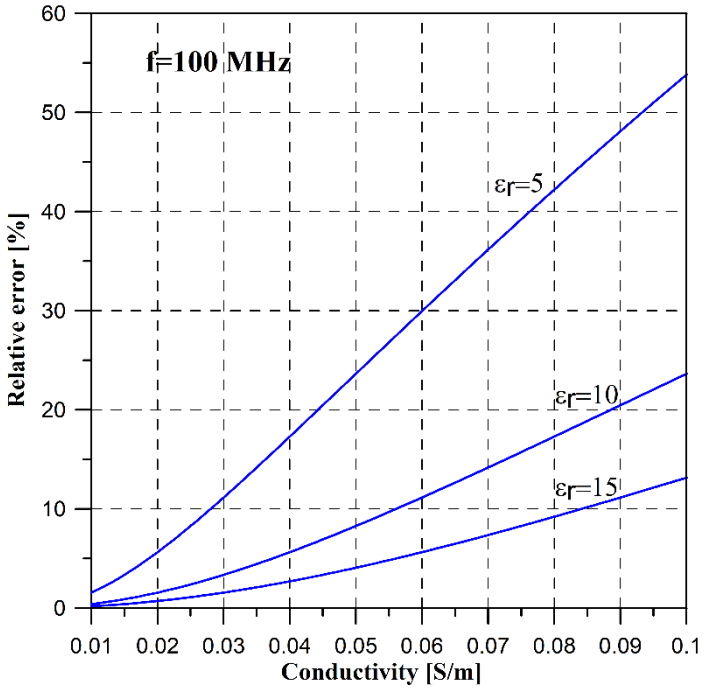

Figure 30. The relative difference between propagation velocities (and vertical resolution) calculated for lossy medium and dielectric at three different dielectric constant (ε_r= 5; 10; 15) values, in case of 100 MHz frequency.

6.1.2. Vertical resolution

The vertical resolution can be observed as a function of the specific conductivity in the case of a lossy medium, calculated for the three frequencies previously studied (Figure 31). In nature, they resemble the course of propagation velocity curves. Based on the figures, it can be

concluded that the vertical resolution improves (decreases in numerical value) with increasing frequency, relative dielectric constant, and specific conductivity. While in a medium with a measuring frequency of 100 MHz with a relative dielectric constant εr = 5 and a resistivity of 1000 Ωm, only reflecting surfaces larger than a vertical distance of 34 cm can be separated, at a frequency of 1.2 GHz objects with a depth difference of more than 3 cm can be separated. For media with a resistivity of 10 Ωm and a relative dielectric constant of εr = 5, the limits for vertical resolution are 21 cm at 100 MHz, 6 cm at 500 MHz and 2.7 cm at 1.2 GHz.

Constant vertical resolution values independent of specific conductivity calculated for the dielectric are indicated by red dashed lines. It can be deduced from the equations given in Chapter 1 that the relative differences in the vertical resolutions calculated for the two models (lossy medium and dielectric) are the same as the relative error (38) defined for the propagation velocities:

$$H = \frac{R_{vd} - R_{vv}}{R_{vv}} \cdot 100 = \frac{v_d - v_v}{v_v} \cdot 100\ [\%], \tag{38}$$

where R_{vd} is the vertical resolution calculated for the dielectric and R_{vl} is the vertical resolution calculated for the lossy medium. It follows that Figure 31 can also be used to analyze the relative error of vertical resolution values.

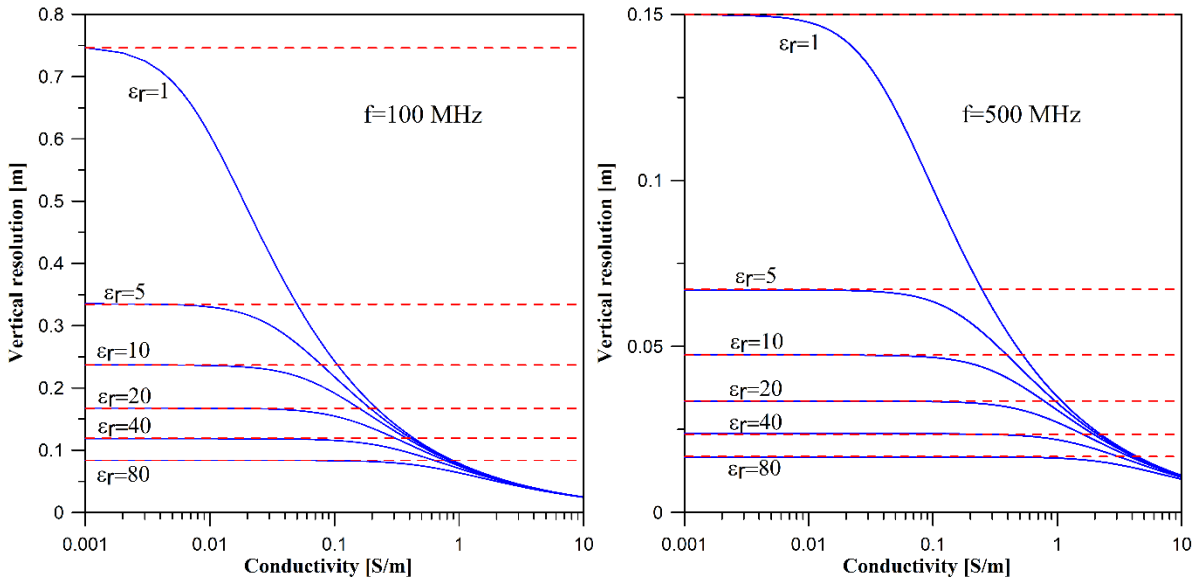

DOI: 10.14750/ME.2022.008

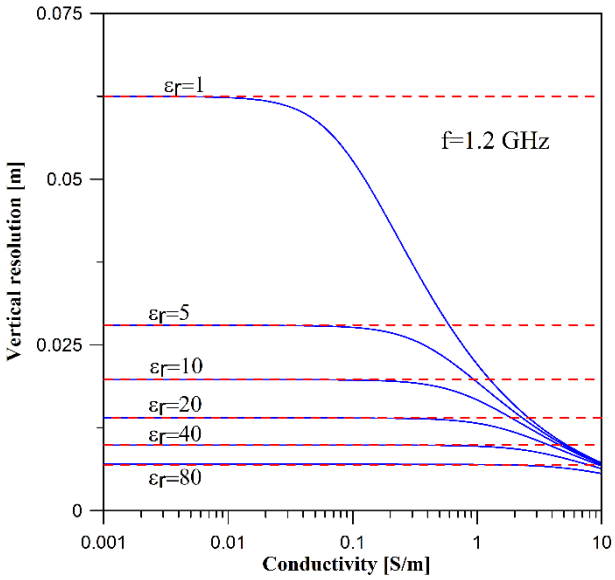

Figure 31. The vertical resolution in lossy and dielectric medium at different dielectric constant (ε_r= 1; 5; 10; 20; 40; 80) values, at 100 MHz, 500 MHz and 1.2 GHz frequency.

If we want to characterize the media in the practice of GPR measurements based on the distribution of their EM petrophysical parameters, then the most difficult thing is the resistivity, because the resistivity of the rocks and soils is about eight orders of magnitude, and depends on the quality and concentration of dissolved salts. For example, the resistivity of the same clayey, sandy soil may vary by at least (or even more) an order of magnitude (10–100 Ωm) depending on whether it is examined after a spring snowmelt or a drought period.

In the case of the dielectric constant, the situation is simpler, because the permeability of the vacuum is ε_o = 8.85 · 10-12 F / m, that of water is about 80 times that (ε_r, water ~ 80), but the relative dielectric constant of most minerals is less than twenty (ε_r, mineral <20). Some sulfides (galenite, pyrrhotine), montmorillonite, or even graphite are exceptions to the more common minerals, which have a dielectric constant of more than 80 (Olhoeft, 1989).

6.1.3. Wavelength

The wavelength (22-23) curves are visualized on a semi-logarithmic scale as a function of conductivity (Figure 32). All six curves belong to a specific dielectric constant value (ε_r= 1; 5; 10; 20; 40; 80). The blue lines indicate the values in the case of lossy medium, the dashed red lines show the constant wavelength values in dielectrics, which are independent from the conductivity.

It can be observed that the wavelength decreases with increasing conductivity and with increasing permittivity. The higher the frequency is, the higher the conductivity value, where

DOI: 10.14750/ME.2022.008

the blue and the red lines start to separate from each other. This means that in the case of lower frequency, the application of the wavelength formula for dielectrics instead of the lossy medium is not so accurate. It can be important in the survey design, when the resolution is estimated based on the wavelength. The characteristics of the wavelength curves are similar to wave propagation velocity curves discussed detailed in Nádasi and Turai (2017). The accurate estimation of wave propagation velocity is crucial in terms of the precise determination of reflection depth of an object.

Assuming the relative dielectric constant is at least five ($\varepsilon_r \geq 5$), the maximum wavelength at 100 MHz is 1.3 m, at 500 MHz it is 27 cm, and at 1.2 GHz it is 12 cm. These values start to decrease with decreasing resistivity, at 100 MHz from 100 Ωm, at 500 MHz from 30 Ωm, at 1.2 GHz from 10 Ωm.

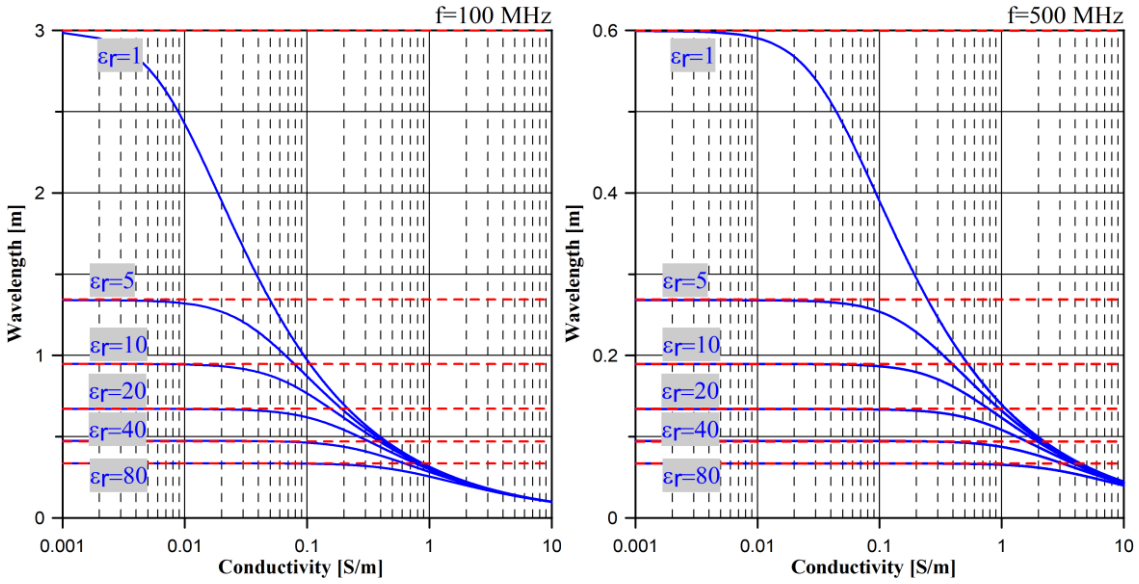

a) b)

DOI: 10.14750/ME.2022.008

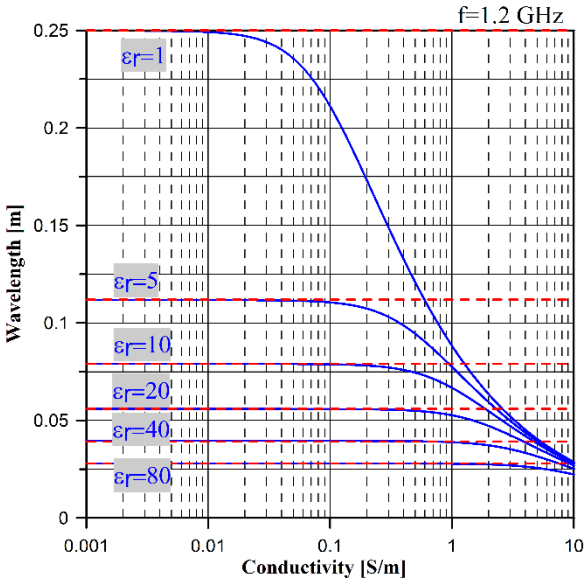

c)

Figure 32. Comparison of wavelengths on a semi-logarithmic graph for lossy medium (blue) and dielectric (red dashed) at different frequencies (a: 100 MHz, b: 500 MHz, c: 1.2 GHz).

6.1.4. Horizontal resolution

The horizontal resolution (25) is not only a function of the wavelength but also depends on the depth. In Figure 33, the horizontal resolution (R_h) is plotted on a semi-logarithmic scale. The horizontal x-axis represents the conductivity. In Figure 33.a, constant frequency (100 MHz) and depth (1 m) values are given and six horizontal resolution curves are presented connecting with six different relative dielectric constant values (ε_r= 1; 5; 10; 20; 40; 80). In figure 33.b, the relative permittivity (ε_r=10) and the frequency (100 MHz) are constant and all thirteen curves indicate a certain depth (0; 0.25; 0.5; …; 3 m). With increasing depth, the horizontal resolution is lower (expressed by number, it is higher). Figure 33.c shows the horizontal resolution values on three different frequencies, at constant relative dielectric constant (ε_r=10) and depth (d=1) value (Nádasi and Turai 2018).

DOI: 10.14750/ME.2022.008

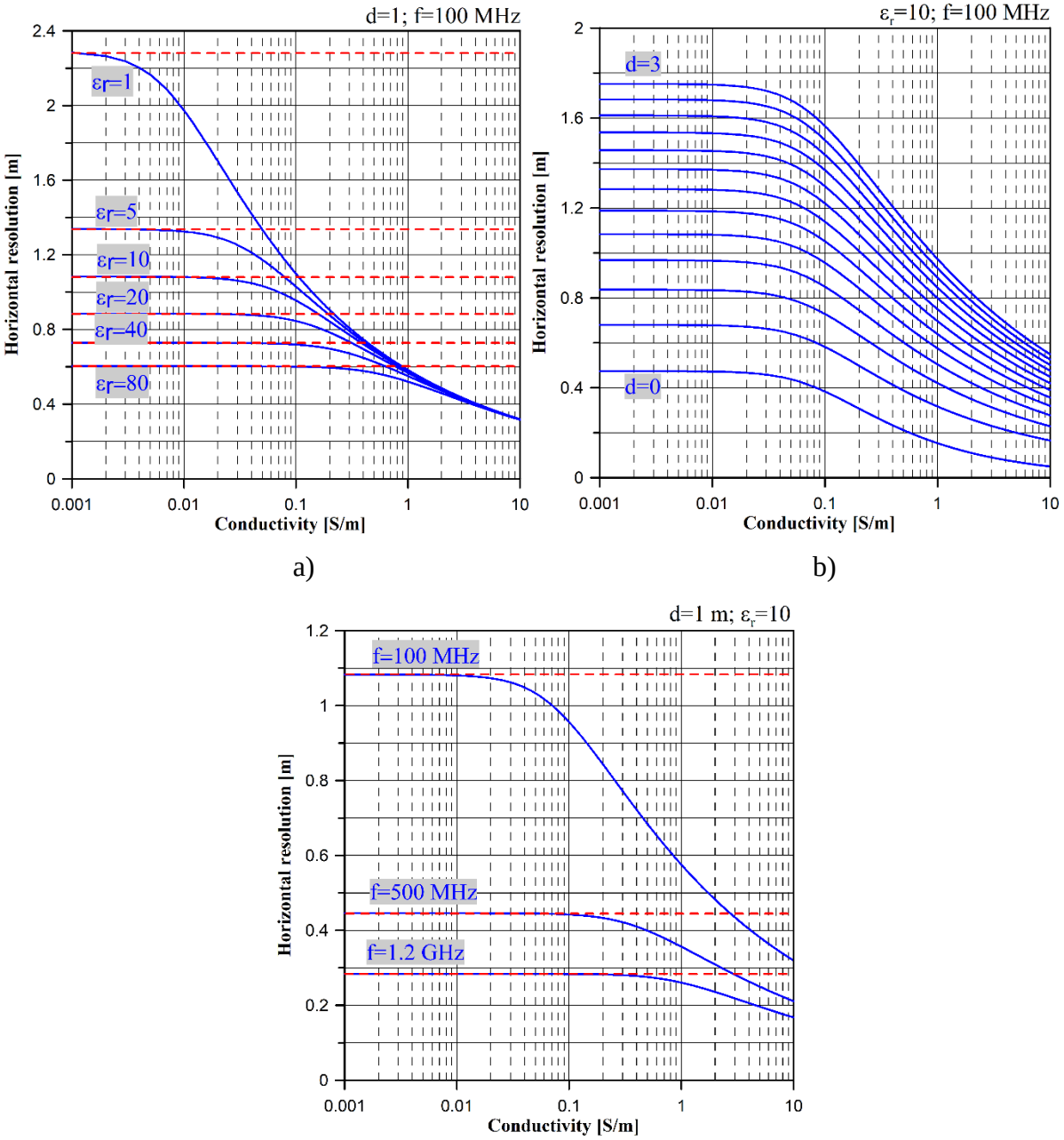

Figure 33. The horizontal resolution in lossy medium (blue) and dielectric (red dashed): a) At different relative dielectric constant values at 100 MHz frequency and d=1 m, b) At 100 MHz frequency and at ε_r=10, with changing depth values from 0 to 3 m by 0.25 m steps, c) At ε_r=10 and at d=1, with three different frequencies (100 MHz, 500 MHz, 1.2 GHz).

6.1.5. Skin depth

In Figure 34, the skin depth (27) is plotted on a log-log scale plot at three different frequencies (100 MHz, 500 MHz, 1.2 GHz). The skin depth is interpreted only in a lossy medium, since there is no attenuation of the EM wave in the dielectric, so there the penetration

DOI: 10.14750/ME.2022.008

would be infinitely large. It decreases exponentially with increasing conductivity. It can be seen that there are no remarkable differences between the three frequencies under 0.01 S/m conductivity (above 100 Ωm resistivity), but deviations increase with increasing frequency and conductivity above 0.01 S/m. If relative dielectric constant is not higher than twenty ($\varepsilon_r \leq 20$) and the resistivity is under 100 Ωm, the skin depth cannot be higher than 2.4 m.

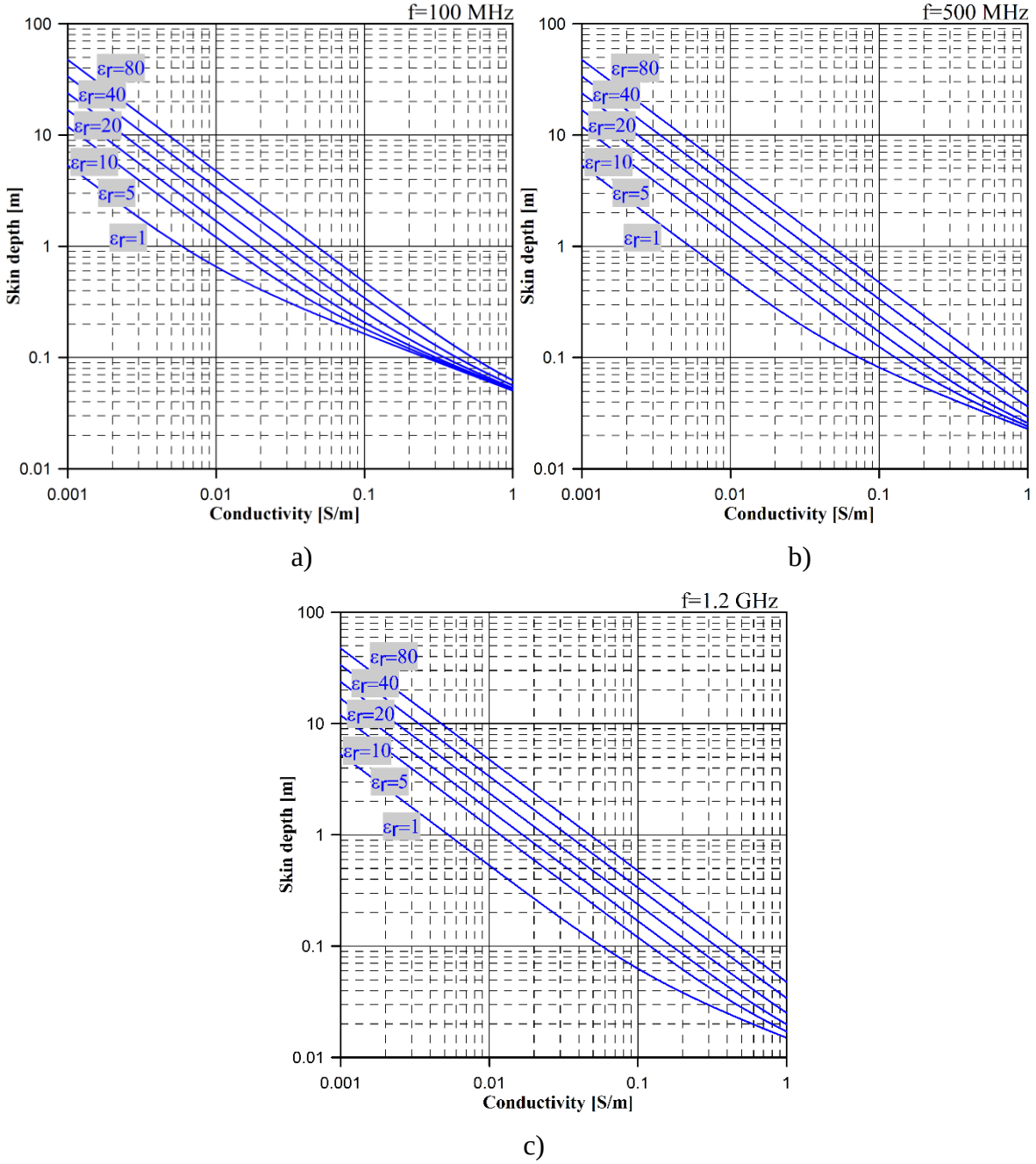

Figure 34. Skin depth on a log-log scale graph in function of conductivity at different frequencies (a: 100 MHz, b: 500 MHz, c: 1.2 GHz).

DOI: 10.14750/ME.2022.008

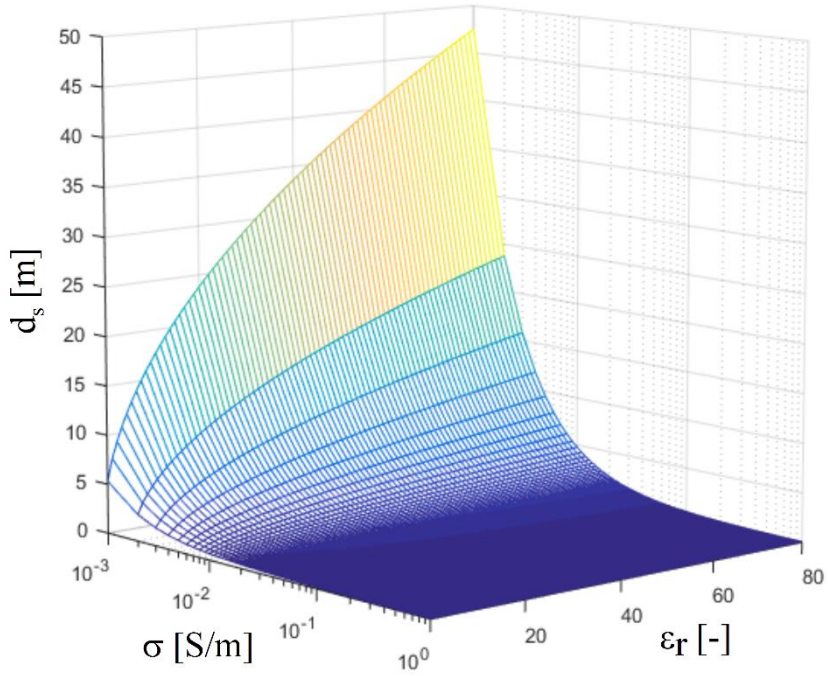

Figure 35. Change in skin depth (d_s) as a function of specific conductivity (σ) and relative dielectric constant (ε_r) at an antenna frequency of 100 MHz (Nádasi et al. 2020).

As the specific conductivity increases, the skin depth decreases significantly. With a constant increase in relative dielectric, with constant specific conductivity, the skin depth increases. The effect of these two parameters on the penetration depth is shown in Figure 35 for the 100 MHz frequency.

6.1.6. Reflection depth

Figure 36 represents the absolute depth difference. It shows the linear connection between the depth and the depth difference. Six different relative dielectric constant and resistivity pairs are demonstrated. The light green line represents a soil with ε_r=10 and ρ=20 Ωm and it can be seen that the depth difference is bigger than 15 cm even in 2 m depth. This is almost 10% error. It could increase up to 20% if the ε_r would decrease to 5 beside the same resistivity. The slope of the curves depends on the product of the relative permittivity and the resistivity. For example, a medium with ε_r=10 and ρ=50 Ωm and another one with ε_r=5 and ρ=100 Ωm have the same curve. It means that the difference between the reflection depth calculated from the equations of dielectrics and lossy media is the same. The values of both Figure 36 were calculated at 100 MHz frequency and μ_r=1.

DOI: 10.14750/ME.2022.008

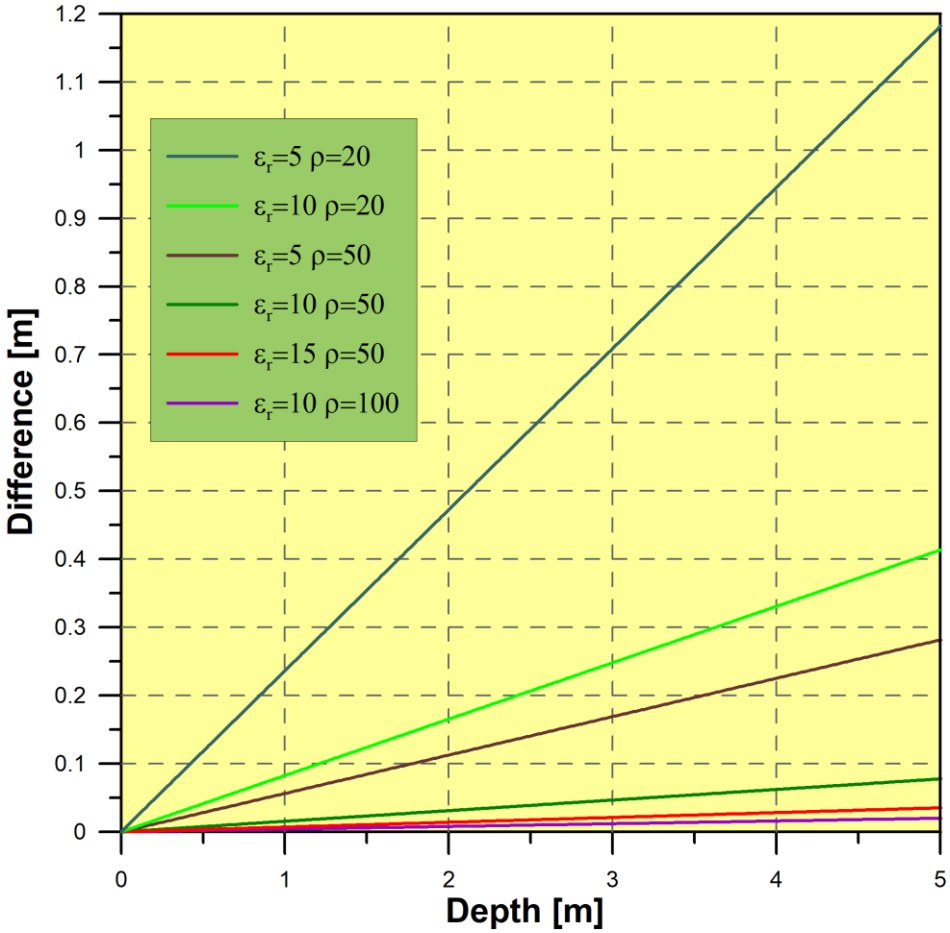

Figure 36. Absolute difference between reflections depths of the two model, with various relative dielectric constant and resistivity values, in the function of true depth (f=100 MHz).

6.1.7. Magnetic permeability changes

Assuming either dielectrics or lossy media, the wave propagation velocity decreases very rapidly with increasing relative magnetic permeability.

Figure 37 shows the characteristics of this decreasing velocity trend. The highest permeability value on the figure (μ_r=200) is still very far from realistic ferromagnetic values (μ_r>1000). In ferromagnetic materials, the velocity will be at least one order of magnitude lower.

DOI: 10.14750/ME.2022.008

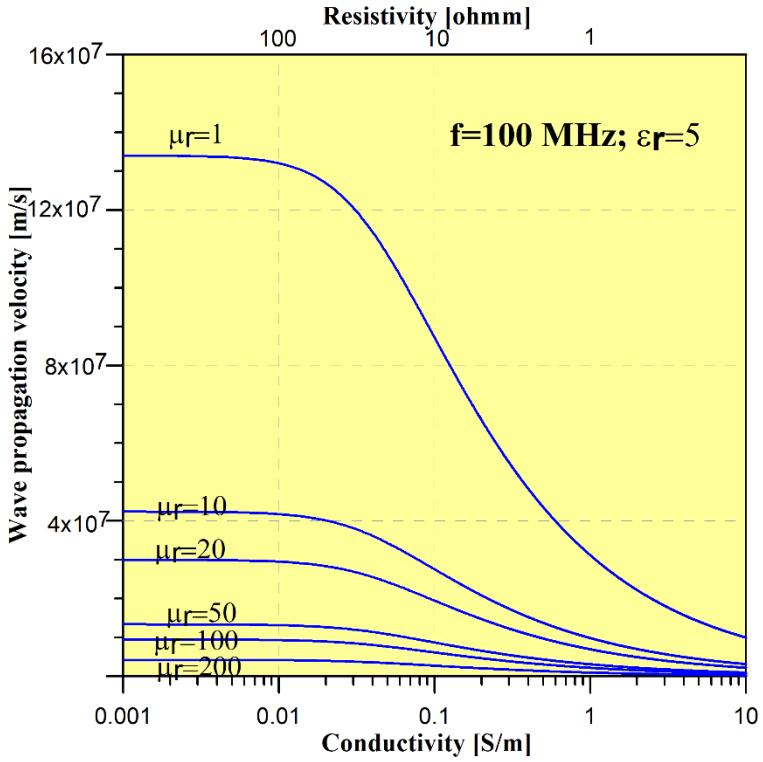

Figure 37. The EM wave propagation velocity as a function of conductivity, in case of increasing relative magnetic permeability, 100 MHz frequency and ε_r= 5 relative permittivity.

6.1.8. Conclusion

The presented theoretical curves show the values of some important GPR parameters in easily readable form. This can be useful in georadar practice for survey design.

The results show the characteristics of the wavelength differences clearly. It can be noticed that the relatively low resistivity range (10–100 Ωm) can be significant in terms of GPR practice. Under these conditions, in the case of ε_r=5-10 values and 100 MHz frequency, the relative difference between the wavelength calculated for dielectric and lossy medium can be 25-50%. This can significantly influence the accurate estimation of resolution. The graphs connected with skin depth can be a helpful tool for GPR users to decide whether the method can be applied successfully in the exploration area.

Furthermore, the application of the equations for lossy media can be beneficial in GPR modeling or in mapping the dielectric constant of soils. It can help in furthering a clear understanding of the loss mechanism associated with soils and allows users to predict the depth of penetration and the depth at which different materials can be detected. This is especially important in utility mapping.

The introduction of the equations of lossy media can be relevant to the dielectric-constant mixing models existing in the literature and in GPR full waveform inversion.

DOI: 10.14750/ME.2022.008

Thesis 5

The relative differences between different GPR parameters (wave propagation velocity, wavelength, resolution, reflection depth) calculated from lossy medium or dielectrics were systematically investigated and characterized. The relative error between the two calculations was given and visualized in the function of conductivity.

Thesis 5.a wave propagation velocity: I found that in case of the wave propagation velocities that our medium has an average dielectric constant of at least ε_r = 5 and a resistivity above 100 Ωm, the relative error is below 2%. But examining the high conductivities (σ> 0.05 S/m), it can be stated that the relative error can be several hundred percent.

Thesis 5.b vertical resolution: I showed that while in a medium with a measuring frequency of 100 MHz with a relative dielectric constant ε_r = 5 and a resistivity of 1000 Ωm, only reflecting surfaces larger than a vertical distance of 34 cm can be separated, at a frequency of 1.2 GHz objects with a depth difference of more than 3 cm can be separated. For media with a resistivity of 10 Ωm and a relative dielectric constant of ε_r = 5, the limits for vertical resolution are 21 cm at 100 MHz, 6 cm at 500 MHz and 2.7 cm at 1.2 GHz.

Thesis 5.c wavelength: I showed that if the relative dielectric constant is at least five ($\varepsilon_r \geq 5$), the maximum wavelength at 100 MHz is 1.3 m, at 500 MHz it is 27 cm, and at 1.2 GHz it is 12 cm. These values start to decrease with decreasing resistivity, at 100 MHz from 100 Ωm, at 500 MHz from 30 Ωm, at 1.2 GHz from 10 Ωm.

Thesis 5.d horizontal resolution: I found that with increasing depth, the horizontal resolution is lower (expressed by number, it is higher). In a medium with a dielectric constant of 10 (ε_r=10) and a resistivity of 100 Ωm, for a 100 MHz antenna, at a depth of 3 m, the horizontal resolution is 1.75 m .

Thesis 5.e skin depth: I showed that if relative dielectric constant is not higher than twenty ($\varepsilon_r \leq 20$) and the resistivity is under 100 Ωm, the skin depth cannot be higher than 2.4 m. As the specific conductivity increases, the skin depth decreases significantly. With a constant increase in relative dielectric, with constant specific conductivity, the skin depth increases.

Thesis 5.f reflection depth: I showed that while ε_r=10 and ρ=20 Ωm the depth difference is bigger than 15 cm even in 2 m depth. This is almost 10% error. It could increase up to 20% if the ε_r would decrease to 5 beside the same resistivity.

DOI: 10.14750/ME.2022.008

6.2. PARAMETER SENSITIVITIES

Parameter sensitivities express the amount of change of a given parameter when another quantity is varying in the system. They are used for example when calibrating systems with large number of parameters and the sensitive ones have to be highlighted. Sensitivity analysis has applications in many fields of science (physics, medicine, economics, etc.). It has also various use in the field of geophysics (seismics, geoelectrics). Different geophysical methods have a specific sensitivity to geological formations. In inversion theory, the so-called sensitivity matrix is used which relates the model parameters to the observed data (Zhdanov 2002). The sensitivity of geophysical data can be increased within a specific target area of a geologic formation. This is the concept of the focusing controlled sensitivity which is a general mathematical formulation and can be applied to a wide variety of geophysical data (Zhdanov 2013). In case of GPR, some studies deal with different types of sensitivities (Saintenoy and Hopmans 2013, Kowalsky et al. 2007).

The slight changes of the EM parameters affect the GPR parameters in a complex manner. These can be characterized by the so-called parameter sensitivities. They can be defined in different ways. The wave propagation velocity is one of the key GPR parameters which is directly related to the reflection depth. Based on analogies from DC geoelectrics (Gyulai, 1989), the velocity and conductivity sensitivities can be defined as follows:

$$\psi = \frac{\partial v_l}{\partial \sigma}\frac{1}{v_l} = \frac{\partial(\ln v_l)}{\partial \sigma}, \tag{39}$$

or

$$\psi^* = \frac{\partial v_l}{\partial \sigma}\frac{\sigma}{v_l} = \frac{\partial(\ln v_l)}{\partial(\ln \sigma)}. \tag{40}$$

The velocity and permittivity sensitivities can be calculated similarly:

$$\psi = \frac{\partial v_l}{\partial \varepsilon_r}\frac{1}{v_l} = \frac{\partial(\ln v_l)}{\partial \varepsilon_r}, \tag{41}$$

or

DOI: 10.14750/ME.2022.008

$$\psi^* = \frac{\partial v_l}{\partial \varepsilon_r}\frac{\varepsilon_r}{v_l} = \frac{\partial(\ln v_l)}{\partial(\ln \varepsilon_r)}. \quad (42)$$

The partial differentiation of the wave propagation velocity can be performed analytically, the chain rule has to be applied. For plotting the sensitivity curves, I used numerical derivation in MATLAB. The sensitivity function is negative in this case (Figure 38) because the velocity decreases if the conductivity increases.

In this case, the wave propagation velocity is the one assuming lossy medium (v_l). The velocity for dielectrics (v_d) would not be sensitive to the conductivity, only the relative dielectric constant.

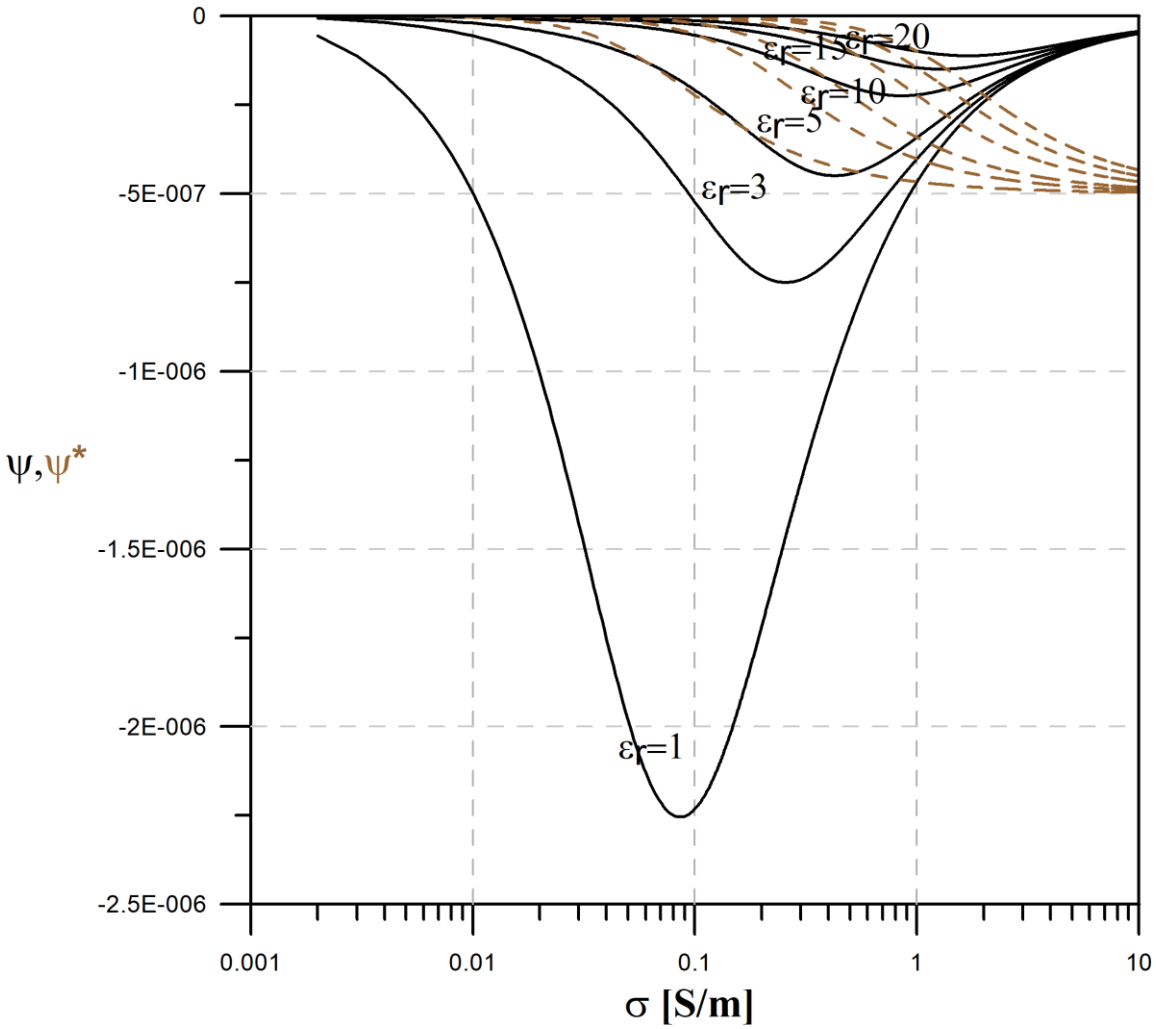

Figure 38. Wave propagation velocity-conductivity sensitivity curves assuming lossy medium. Black lines indicate ψ, brown dashed lines indicate ψ^*.

DOI: 10.14750/ME.2022.008

The wave propagation-conductivity sensitivity (based on Equation 39) clearly has an absolute maximum value. In case of ε_r=1 this extreme value is bigger than 10 Ωm. With increasing dielectric constant, it decreases below 10 Ωm. Ψ^* (40) can be produced from Ψ with a simple multiplication of conductivity.

The lower is the relative permittivity the more sensitive is the velocity to the conductivity changes (Figure 39). If ε_r is between 1 and 10 the sensitivity is dependent from the resistivity but above 10 it is independent from it.

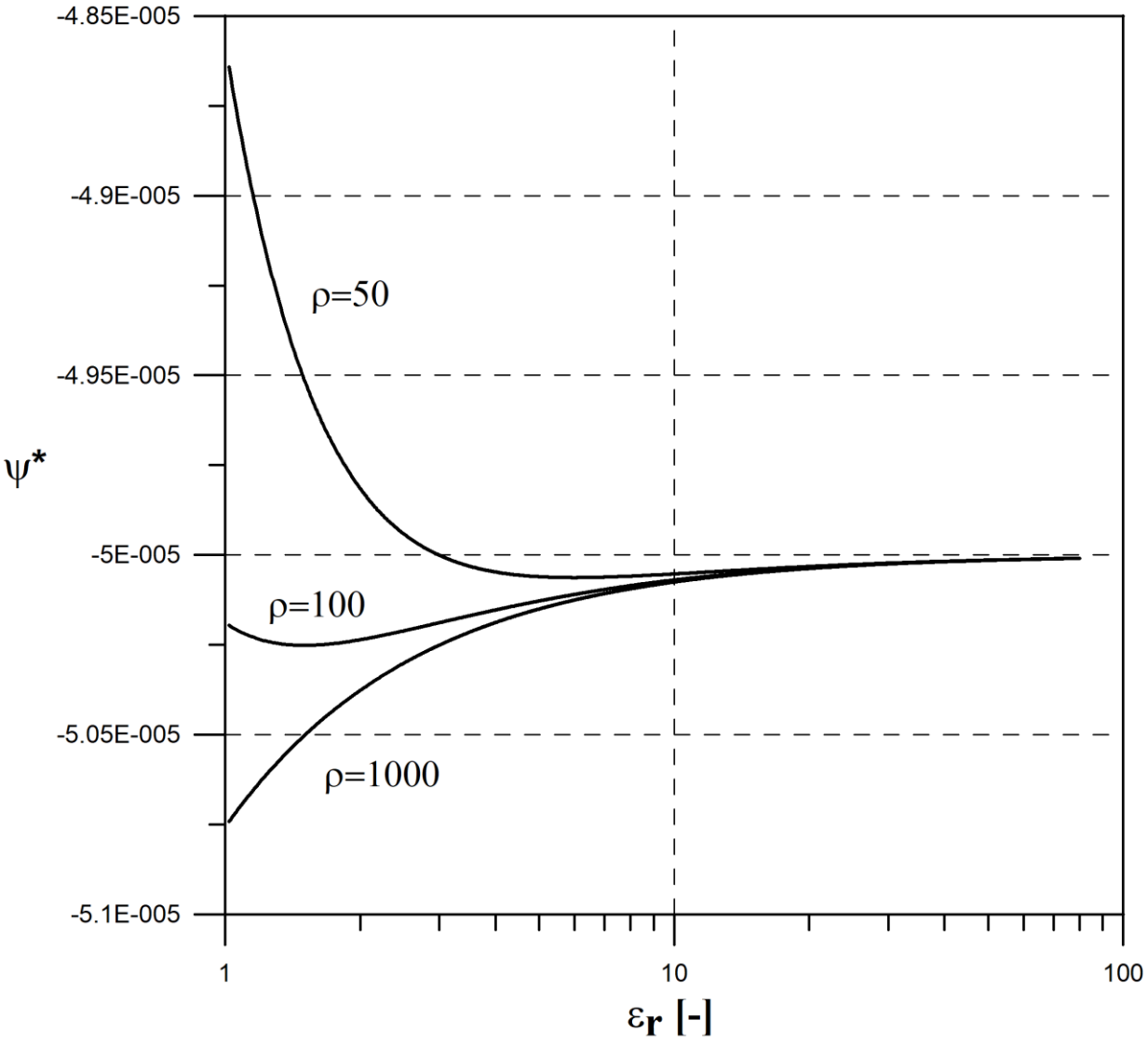

Figure 39. Wave propagation velocity-relative permittivity sensitivity (Ψ^*) curves assuming lossy medium. Three resistivity values are presented.

DOI: 10.14750/ME.2022.008

Thesis 6

I have shown by parameter sensitivity calculations that the conductivity sensitivity of the propagation velocity is the highest for the medium with 1 relative dielectric constant and 0.08 S/m conductivity, and this sensitivity decreases with increasing relative dielectric constant and conductivity.

DOI: 10.14750/ME.2022.008

6.3. MODELING EXAMPLES

In order to model the effect of resistivity change, MATGPR (Tzanis, 2010) modeling software was used. It can generate synthetic GPR B-scans with the Split-step methods of Bitri and Grandjean (1998). 2D EM models were created. The geometry and the EM parameter values need to be set up. Choosing the appropriate grid size is also an important step before forward modeling. The model dimensions and sampling rate are specified as well.

In the presented models (Figure 40) the anomalous body is a rectangle shaped cavity with ε_r=1 and ρ=10000 Ωm. The differences between the three simple models are the background resistivity values (10^4, 50 and 20 Ωm). The relative permittivity equals 10 in all three cases (ε_r=10). The relative magnetic permeability (μ_r=1) and the antenna frequency (100 MHz) are also the same (Nádasi and Turai 2020).

Because of the lower resistivity of the background (model) on the right side (and in the middle), the image of the radargram is quite blurred. The bottom of the anomalous rectangle cannot be seen very clearly as it can be on the left side. The edges are not sharp at all in the lower resistivity backgrounds. The top of the rectangle looks thicker and a dark patch spreads towards the surface. A full hyperbola can be observed in the middle radargram. However, the B-scan on the left side has better quality, the middle (Figure 40.b) one still contains the necessary information. Only the bottom of the cavity is uncertain, because definite reflection is not received and the image itself is quite blurred. Figure 40.c radargram contains the least information and has the lowest resolution. Under real circumstances the quality and the information content of the B-scan could be even worse because of the noise and other reflection interferences.

The first break can be read out at about 42 nsec on the left image, and at about 35 nsec in the middle and at about 28 nsec on the right side. Besides the two-way-traveltime there is an obvious difference between the resolution.

DOI: 10.14750/ME.2022.008

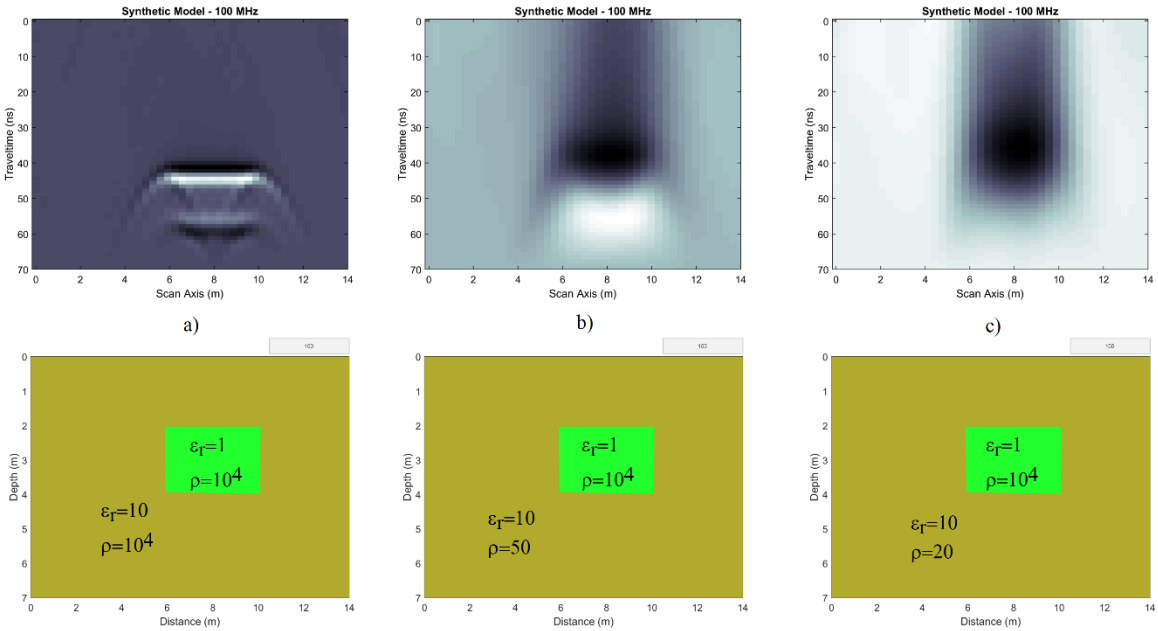

Figure 40. Split-step modeling results of one simple rectangle shaped cavity in 2–4 meters depth in case of a very resistive ($\rho_a=10^4$ Ωm) background (a) and two lower resistivity ($\rho_b=50$ Ωm and $\rho_c=20$ Ωm) backgrounds (b-c). True models are below and the synthetic B-scans can be seen above. The relative magnetic permeability equals 1 ($u_r=1$) in every part of the three model.

6.3.1. FORWARD MODELING OF REINFORCEMENT BAR STRUCTURES

For forward modeling the MATGPR system (Tzanis 2010) was used. The synthetic GPR sections were calculated with the method of Bitri and Grandjaen (1998).

In the first example (in Figure 41) the background was set to the following EM parameters: $\rho=1000$ Ωm; $\varepsilon_r=9$; $\mu_r=1$. The rebars were set to the same sizes (10 mm diameter), their parameters: $\rho=1$ Ωm; $\varepsilon_r=2$; $\mu_r=20$ (Nádasi 2020).

DOI: 10.14750/ME.2022.008

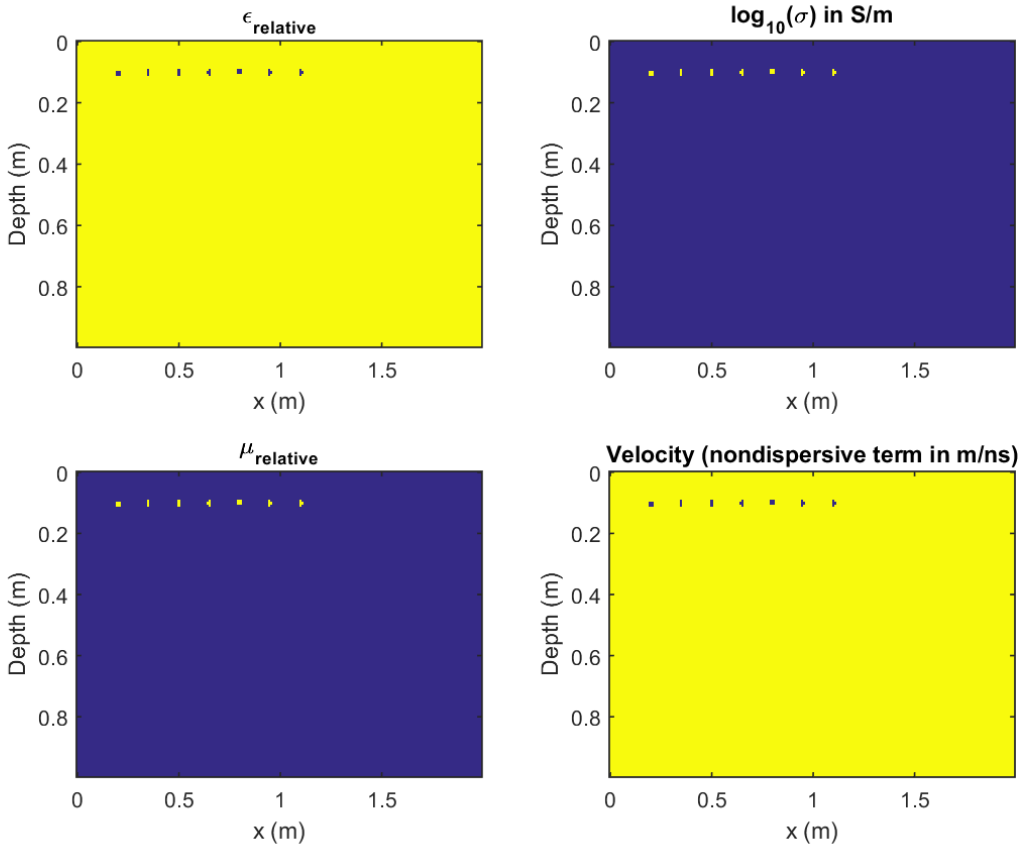

Figure 41. Simple 2D model with 10 cm rebars. Yellow color indicates higher value compared to the blue one.

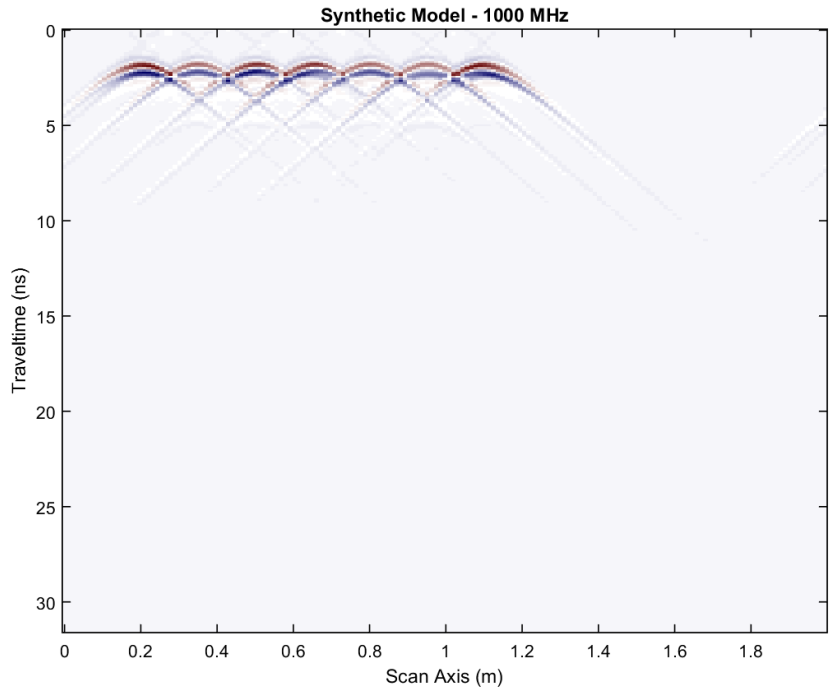

DOI: 10.14750/ME.2022.008

Figure 42. Synthetic radargram of the simple 2D rebar model. Each rebar produced one separable hyperbole, applying 1000 MHz frequency.

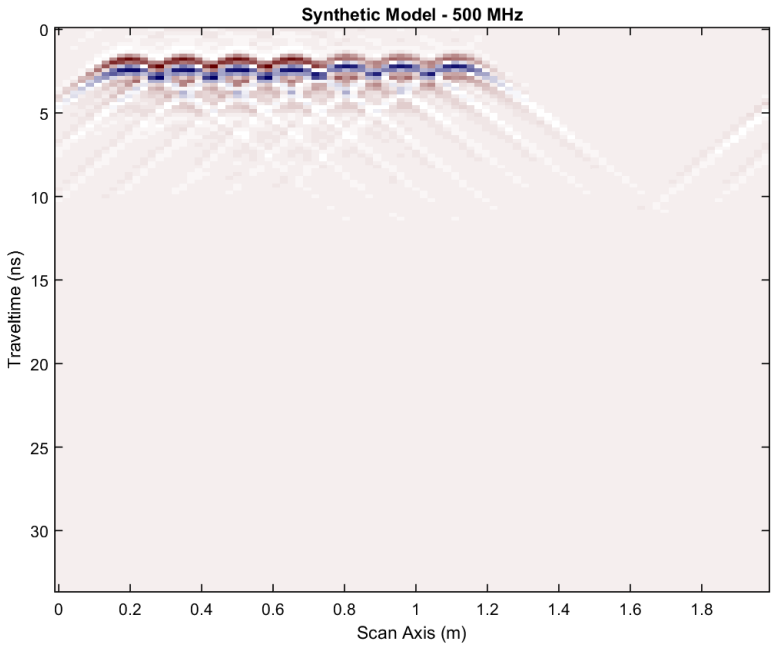

Figure 43. Synthetic radargram of the simple 2D rebar model. The hyperboles cannot be separated clearly in case of 500 MHz frequency.

The synthetic data show that the rebars appear with strong reflections, so they can be detected easily in a concrete structure. In the presented case (Figure 42), a 1 GHz antenna can produce optimal resolution, the rebars are only in 10 cm depth. Figure 43 shows another synthetic radargram on the same 2D rebar model but with 500 MHz frequency. Here, the hyperboles cannot be separated clearly.

The rebar can overshadow an anomaly underneath. However, cavities can be detected even below the rebar, as Figure 44 shows.

DOI: 10.14750/ME.2022.008

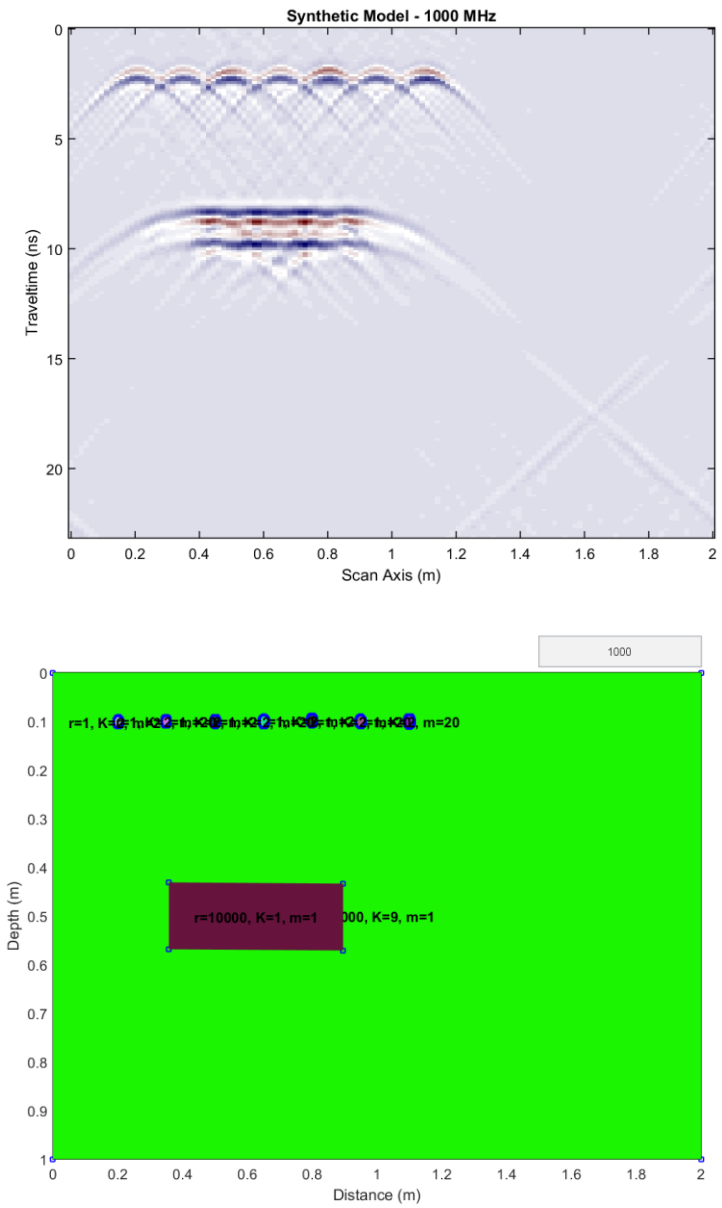

Figure 44. Model with rebars (d=10 cm) and a cavity (on the bottom), synthetic radargram (on top).

The GPR measurement of rebar structures is a challenging task. The antenna frequency has to be chosen carefully in order to get good resolution images. Because the EM waves attenuate intensively and their velocity decreases significantly in ferromagnetic materials, good resolution is hopeless under a rebar structure. However, the rebar structure itself can be monitored accurately, if the measurement is well prepared. The forward modeling of the expected structure will increase the possibility of a successful GPR measurement.

DOI: 10.14750/ME.2022.008

Detecting additional anomalies around the rebar structure is an interesting and complex modeling problem. Since weak and normal anomalies can stay hidden under the rebar system, strong anomalies can be still recognized in this environment.

Thesis 7

I have shown that the rebar structure at a depth of 0.1 m can be well detected using a GPR antenna with a frequency of 1 GHz, however, using the 500 MHz antenna, the resolution is significantly worse.

DOI: 10.14750/ME.2022.008

Summary

My PhD dissertation summarizes electromagnetic geophysical research carried out at the Department of Geophysics of the University of Miskolc and at the Consortium for Electromagnetic Modeling and Inversion (CEMI) of the University of Utah. The aim of my research was to test, develop and compare modern evaluation methods that are related to current research directions in the case of magnetotelluric (MT) and ground penetrating radar (GPR) methods. The calculations and inversion runs presented in the dissertation were realized in MATLAB environment.

Firstly, I performed statistical analyzes in connection with a Hungarian MT dataset before the inversion runs. The mean probing curves discussed in classical statistical methods could be used well as a start model for 3D inversion. Based on the correlation maps, I drew conclusions about the dimensionality of the geological structure. Among the modern, multivariate statistical methods, I used cluster analysis. By interpolating (kriging) based on city-block distance (or Manhattan distance) clustering, a WSW-ENE direction structure emerged, which coincides with the previously described structures.

After that, I presented the 2D and 3D inversion evaluation of the Hungarian MT dataset. 2D inversion evaluation was performed according to the method of nonlinear conjugated gradient by Rodi and Mackie (2001). The 3D inversion run was implemented based on the regularized Gaussian-Newton algorithm in the data space (Gribenko and Zhdanov 2017). In both cases, it was possible to identify the conductive zones in the knowledge of the previously known geological model.

Most of the North American MT data falls on Canadian territory and is related to the Lithoprobe project. A smaller half of the data belongs to the EarthScope project measured in the United States. The data from an area of about 1000 x 1000 km also contain signals with extremely long periods, so they are suitable for deep depth structural analysis. The Western Superior region, part of the Canadian Shield, is an area with complex tectonics where several microcontinental blocks have previously been identified. Along these, seismic V_p (primary wave propagation velocity) anisotropy has already been described, but conductivity anisotropy also seemed likely. Anisotropic modeling as well as analysis and inversion of MT data found further evidence for the occurrence of conductivity anisotropy in the field. Using the regularized Gaussian-Newton inversion in the data space, additional conductive zones were identified in relation to each geological unit.

DOI: 10.14750/ME.2022.008

Chapter 6 summarizes my research related to the ground penetrating radar. Here, I compared the physical models for the dielectric and the lossy medium in terms of how different the GPR parameters (wavelength, wavelength, resolution, scan depth, penetration depth, etc.) calculated from them differed. Based on the comparison, I constructed theoretical curves that show the values of the most important GPR parameters as a function of conductivity for the two cases. The curves show that the large differences occur in the range of good conductors in the case of media with high specific conductivity. The range between 10 and 100 Ωm can be of theoretical and practical significance for dielectric constants close to $\varepsilon r = 5\text{-}10$, especially when using lower GPR frequencies (e.g. 100 MHz). Under such conditions, an error of up to 25-50% can be made by estimating the individual parameters (velocity, resolution, penetration depth) from a simplified relation for the dielectric. Using the formula for the insulator, the resolution is underestimated (beyond the numerical value) in each case. This should be taken into account for underground objects to be explored when deciding on detectability or selecting the applicable frequency.

In connection with the GPR method, I examined the parameter sensitivities based on the analogy taken from geoelectric practice. Propagation velocity - conductivity and propagation velocity - relative permittivity sensitivities were calculated and plotted. Furthermore, I performed synthetic modeling for the comparison of the lossy medium versus dielectric as well as for the increase in magnetic permeability. The latter has practical significance in the examination of reinforced concrete structures.

The theses in the dissertation - related to either MT or GPR methods - are related to important research directions, mainly in the field of forward modeling and inversion.

The results related to MT contributed to the refinement of the geophysical-geological model of the two presented target areas in terms of practice. In Hungary, the geometry of the well-conducting zones related to the ore indication has been clarified. The results presented from the North American area are mainly of geodynamic relevance and serve to understand the deep structure.

Theses related to GPR are important for measurement design as well as for deciding applicability, and the examination of parameter sensitivities can be useful in the field of forward modeling. The dielectric model cannot be used for georadar survey on relatively low resistivity and complex structures (e.g., certain soils). The comparative analyzes and models presented here should be considered.

DOI: 10.14750/ME.2022.008

Összefoglalás

A PhD dolgozatom a Miskolci Egyetem Geofizikai Tanszékén, valamint a Utah Egyetem CEMI (Consortium for Electromagnetic Modeling and Inversion) intézetében elvégzett elektromágneses geofizikai kutatásokat foglalja össze. Kutatómunkám célja olyan modern kiértékelési eljárások alkalmazása, fejlesztése, összehasonlítása volt, melyek a magnetotellurika (MT) és a földradar (GPR) módszerek esetében aktuális kutatási irányokhoz kapcsolódnak. Az értekezésben bemutatott számítások, inverziós futtatások MATLAB környezetben történtek.

Elsőként egy magyarországi MT adatrendszerhez kapcsolódva statisztikai vizsgálatokat végeztem az inverziós futtatásokat megelőzően. A klasszikus statisztikai módszereknél tárgyalt átlag szondázási görbék jól használhatónak bizonyultak a 3D inverzió start modelljeként. A korrelációs térképek alapján a földtani szerkezet dimenzionalitására vonatkozóan vontam le következtetéseket. A modern, többváltozós statisztikai módszerek közül a klaszter analízist alkalmaztam. A city-block távolság (v. Manhattan-távolság) alapú klaszterezés interpolásával (krigelés) egy NyDNy-KÉK irányú szerkezet rajzolódott ki, mely egybevág korábban leírt struktúrákkal.

Ezt követően a magyarországi MT adatrendszer 2D és 3D inverziós kiértékelését mutattam be. A 2D inverziós kiértékelés Rodi és Mackie nemlineáris konjugált gradiens eljárása szerint történt. A 3D inverziós futtatás az adattérbeli regularizált Gauss-Newton algoritmus (Gribenko és Zhdanov 2017) alapján valósult meg. Mindkét esetben sikerült a vezetőképes zónák azonosítása az addig ismert földtani modell ismeretében.

Az észak-amerikai MT adatok nagyobbik része kanadai területre esik és a Lithoprobe projekthez kapcsolódik. Az adatok kisebbik fele az Egyesült Államokban lemért EarthScope projekthez tartozik. A mintegy 1000 x 1000 km-es területről származó adatok rendkívül hosszú periódusú jeleket is tartalmaznak, így alkalmasak nagy mélységű szerkezetvizsgálatra. A kanadai pajzs részét képező Western Superior régió komplex tektonikával rendelkező terület, ahol korábban számos mikrokontinentális blokkot azonosítottak. Ezek mentén már leírtak szeizmikus V_p (primer hullámterjedési sebesség) anizotrópiát, ám a vezetőképesség anizotrópia is valószínűnek tűnt. Anizotóp modellezés, valamint az MT adatok elemzésével és inverziójával további bizonyítékokat sikerült találni a vezetőképesség anizotrópia előfordulására a területen. Az adattérbeli regularziált Gauss-Newton inverzió segítségével további vezetőképes zónákat sikerült azonosítani az egyes földtani egységekhez kapcsolódóan.

DOI: 10.14750/ME.2022.008

A hatodik fejezet a földradarhoz kapcsolódó kutatásaimat foglalja össze. Itt a dielektrikumra, illetve veszteséges közegre vonatkozó fizikai modelleket hasonlítottam össze abból a szempontból, hogy az ezek alapján számított GPR paraméterek (hullámterjedési sebesség, hullámhossz, felbontóképesség, szkin-mélység, behatolási mélység stb.) mennyire térnek el egymástól. Az összehasonlítás alapján elméleti görbéket szerkesztettem, melyek a vezetőképesség függvényében mutatják a legfontosabb GPR paraméterek értékeit a két esetre. A görbéken látható, hogy a nagy eltérések a jó vezetők tartományában, a nagy fajlagos vezetőképességű közegek esetén jelentkeznek. Elméleti és gyakorlati jelentősége a 10–100 Ωm közötti tartománynak lehet az ε_r=5-10 értékhez közeli dielektromos állandók esetében, különösen az alacsonyabb GPR frekvenciák (pl. 100 MHz) alkalmazásakor. Ilyen körülmények között akár 25-50 %-os hibát is véthetünk, ha az egyes paramétereket (sebesség, felbontóképesség, behatolási mélység) a dielektrikumra vonatkozó egyszerűsített összefüggésből becsüljük. A szigetelőre érvényes formula alkalmazásával a felbontóképességet minden esetben alul becsüljük (számértékben túl). Ezt a megkutatni kívánt földalatti objektumok esetében érdemes figyelembe venni a kimutathatóság eldöntésénél, vagy az alkalmazandó frekvencia kiválasztásánál.

A GPR módszerhez kapcsolódóan vizsgáltam a paraméter érzékenységeket a geoelektromos gyakorlatból vett analógia alapján. Terjedési sebesség – vezetőképesség és terjedési sebesség – relatív permittivitás érzékenységeket számítottam és ábrázoltam. Továbbá szintetikus modellezéseket végeztem a veszteséges közeg kontra dielektrikum összehasonlítása, valamint a mágneses permeabilitás megnövekedésének esetére. Utóbbinak a vasbeton szerkezetek vizsgálatánál van gyakorlati jelentősége.

Az értekezésben szereplő tézisek – akár az MT, akár a GPR módszerekhez kapcsolódóan – fontos kutatási irányokhoz kapcsolódnak elsősorban az előre modellezés és az inverzió területén.

Az MT-hez kapcsolódó eredmények a gyakorlat szempontjából hozzájárultak a két bemutatott célterület geofizikai-földtani modelljének pontosításához. A hazai területen az ércindikációhoz kapcsolódó jól vezető zónák geometriáját sikerült pontosítani. Az észak-amerikai területről bemutatott eredmények elsősorban geodinamikai vonatkozásúak és a mélyszerkezet megismerését szolgálják.

A GPR-hoz kapcsolódó tézisek a méréstervezés, valamint az alkalmazhatóság eldöntése szempontjából fontosak, továbbá a paraméter érzékenységek vizsgálata az előre modellezés területén lehet hasznos. A relatíve alacsony fajlagos ellenállású és komplex struktúrák (pl.

DOI: 10.14750/ME.2022.008

bizonyos talajok) földradar kutatásánál a dielektrikum modell nem használható. Itt figyelembe kell venni a bemutatott összehasonlító elemzéseket és modelleket.

DOI: 10.14750/ME.2022.008

ACKNOWLEDGEMENT

Firstly, I owe my greatest gratitude to my supervisor, Dr. Endre Turai, for guiding my work, giving me useful advices and sharing his professional experience with me.

I am thankful to Prof. Dr. Michael S. Zhdanov, Distinguished Professor of Geophysics, Director of the Consortium for Electromagnetic Modeling and Inversion (CEMI) at the University of Utah, for being my scientific leader during my pre-doctoral scholarship in Salt Lake City.

I would like to thank Dr. Alexander V. Gribenko, Research Professor of CEMI for strengthening my coding skills, discussing and analyzing with me practical issues of MT forward modeling and inversion.

I would also like to thank Dr. Viktor Wesztergom, the GGI director of the Hungarian Academy of Sciences, for admitting me to their institute in Sopron, where excellent conditions ensured my professional development.

I would like to acknowledge Prof. Dr. László Szarka for useful discussions in EM geophysics.

I also thank Prof. Dr. Norbert Péter Szabó, Head of Department, Vice-dean of the Faculty for encouraging me and supporting my research.

As a member of Department of Geophysics, I also want to express my gratitude to all of my colleagues.

I am grateful to my wife and my whole family for their continuous love and support.

For providing the data used in this PhD thesis, I am thankful to:

The main volume of North American MT data was collected by the Lithoprobe project, supported by the Natural Sciences and Engineering Research Council, Canada. Some other stations were acquired by the Incorporated Research Institution for Seismology as part of the Earth Scope project. These data were made available through Earth-Scope (www.earthscope.org; EAR-0323309), supported by the National Science Foundation.

The research was carried out in the framework of the GINOP-2.3.2-15-2016- 00010 "Development of enhanced engineering methods with the aim at utilization of subterranean energy resources" project of the Research Institute of Applied Earth Sciences of the University of Miskolc in the framework of the Széchenyi 2020 Plan, funded by the European Union, co-financed by the European Structural and Investment Funds.

REFERENCES

Ádám A. (1956): Ein neues tellurisches Messinstrument. Bányamérnöki és Földmérőmérnöki Karok Közleményei 19: pp. 1–7.

Ádám A. (1958): Über ein modifiziertes tellurisches Schurfgerat und dessen Verwendung zu tellurischen Untersuchungen grosses Ausmasses. Freiberger Forschungshefte. Reihe C, Geowissenschaften, Paleontologie 45: pp. 52–61.

Ádám A. és Bencze P. (1961): Kísérletek a magnetotellurikus módszerrel. Magyar Geofizika II: pp. 57–59.

Árkai, P. (1977): Low-grade metamorphism of Paleozoic sedimentary formations of the Szendrő Mountains (NE-Hungary). Acta Geol. Acad. Sci. Hung., 1977, 21/1-3, 53-80.

Avdeeva, A., Moorkamp, M., Avdeev, D., Jegen, M., & Miensopust, M. (2015): Three dimensional inversion of magnetotelluric impedance tensor data and full distortion matrix. Geophysical Journal International, 202 (1), 461—481.

Bedard, J. H., and L. B. Harris (2014): Neoarchean disaggregation and reassembly of the Superior craton, Geology 42 (11), 951—954.

Bitri, A., Grandjean, G. (1998): Frequency - wavenumber modelling and migration of 2D GPR data in moderately heterogeneous dispersive media. Geophysical Prospecting, 46, pp. 287–301.

Cagniard, L. (1953): Basic theory of the magnetotelluric method of geophysical prospecting. Geophysics, 1953, 18, 605-635.

Cai H., B. Xiong, M. Han, and M. S. Zhdanov (2014): 3D controlled-source electromagnetic modeling in anisotropic medium using edge-based finite element method: Computers & Geosciences, 73, 164-176.

Cantwell, T. (1960): Detection and Analysis of Low-Frequency Magnetotelluric Signals. Ph.D. Thesis, Massachusetts Institute of Technology, Cambridge, Massachusetts.

Chave, A. D. and A. G, Jones (2012): The Magnetotelluric Method: Theory and Practice: Cambridge University Press.

Constable, S. C., R. L. Parker, and C. G. Constable (1987): Occam's inversion: A practical algorithm for generating smooth models from electromagnetic sounding data: Geophysics, 52, 289-300.

Cox, L.H., Wilson, G.A., and M.S. Zhdanov (2010): 3D inversion of airborne electromagnetic data using a moving footprint: Exploration Geophysics, 41, 250-259.

Craven, J. A., T. T. Skulski, and D. W. White (2004): Lateral and vertical growth of cratons: seismic and magnetotelluric evidence from the western Superior transect, In Lithoprobe Celebratory Conference, Lithoprobe Report 86.

Csáki, F. (1976): Complex geological investigation of the Paleozoic formations in the Cserehát. Doctoral thesis in Hungarian, 1976.

Csókás J. és Takács E. (1964): Magnetotellurikus mérések a Magyar Alföldön. Bányászati Lapok 10: pp. 713–717.

Čuma, M, A Gribenko, and M. S. Zhdanov (2017): Inversion of magnetotelluric data using integral equation approach with variable sensitivity domain: application to EarthScope MT data: Physics of the Earth and Planetary Interiors, 270, 113-127

Czeglédi, B. (2013): Joint evaluation of the exploration data, geochemical and geophysical relationship of the Gadna-Irota area. MSc Thesis, University of Miskolc.

Ferguson, I. J., J. A. Craven, R. D. Kurtz, D. E. Boerner, R. C. Bailey, X.Wu, M. R. Orellana, J. Spratt, G. Wennberg, and A. Norton (2005): Geoelectric response of Archean lithosphere in the western Superior Province, central Canada. Physics of the Earth and Planetary Interiors, 150, 123—143.

Földessy, J. (2014): Basic research of the strategic raw materials in Hungary. CriticEl Monography series 10, Miskolc.

Gribenko, A. and M. S. Zhdanov (2007): Rigorous 3D inversion of marine CSEM data based on integral equation method: Geophysics, 72 (2), WA73-WA84.

Gribenko, A. V., and M. S. Zhdanov (2017): Regularized Gauss-Newton method of nonlinear geophysical inversion in the data space: Applications to 3D magnetotelluric inversion: In Expanded Abstracts, Proceedings of the 87th SEG International Exposition and Annual Meeting; Society of Exploration Geophysicists: Tulsa, OK, USA, 1052-3812.

Gribenko, A. V., Nádasi, E., Zhdanov, M. S. (2021): Regularized Gauss-Newton method in the data space: applications to 3D inversion of the Lithoprobe and EarthScope magnetotelluric data. Proceedings of Annual Meeting of Consortium for Electromagnetic Modeling and Inversion, University of Utah, Salt Lake City, UT, U.S.A., June, 2021, pp. 35-66.

Groom, R. W., and R. C. Bailey (1989): Decomposition of magnetotelluric impedance tensors in the presence of local three-dimensional galvanic distortion, Journal of Geophysical Research, 94, 1913-1925.

Gyulai, Á. (1989): Parameter sensitivity of underground DC measurements. Geophysical Transactions, 35 (3) pp. 209–225.

Hursán, G., and M. S. Zhdanov (2002): Contraction integral equation method in three-dimensional electromagnetic modeling: Radio Science, 37 (6), 1-13.

Jol, H. M. (2008): Ground Penetrating Radar Theory and Applications. Elsevier.

Kelbert, A., N. Meqbel, G. D. Egbert, and K. Tandon (2014): ModEM: A modular system for inversion of electromagnetic geophysical data: Computers and Geosciences, 66, 40—53, doi: 10.1016/j.cageo.2014.01.010

Kendall J-M, S. Sol, C. J. Thomson, D. J. White, I. Asudeh, C. S. Snell, F. H. Sutherland, (2002): Seismic heterogeneity and anisotropy in the Western Superior Province, Canada: insights into the evolution of an Archaean craton: Geological Society, London, Special Publications, 199, 27-44.

Kowalsky, M.B. & Birkholzer, Jens & Peterson, J. & Finsterle, Stefan & Mukhopadhyay, Sumit & Tsang, Y. (2008): Sensitivity Analysis for Joint Inversion of Ground-Penetrating Radar and Thermal-Hydrological Data from a Large-Scale Underground Heater Test. Nuclear Technology. 164. 169-179. 10.13182/NT08-A4017.

Lyu, Y., Wang, H., Gong, J. (2020): GPR Detection of Tunnel Lining Cavities and Reverse-time Migration Imaging. Applied Geophysics, Vol. 17, No. 1. pp. 1-7.

MacQueen, J. B. (1967): *Some Methods for classification and Analysis of Multivariate Observations,* Proceedings of 5-th Berkeley Symposium on Mathematical Statistics and Probability, Berkeley, University of California Press, 1967, 1:281-297.

Martinez A., Byrnes A. P. (2001): Modeling Dielectric-constant values of Geologic Materials: An Aid to Ground-Penetrating Radar Data Collection and Interpretation. Current Research in Earth Sciences, Bulletin 247, Part 1.

Musacchio G., D. J. White, I. Asudeh, and C. J. Thomson (2004): Lithospheric structure and composition of the Archean western Superior Province from seismic refraction/wide-angle reflection and gravity modeling, Journal of Geophysical Research, 109, B03304.

Nádasi E. (2020): GPR forward modeling for reinforcement bar structures in civil engineering. Műszaki Földtudományi Közlemények, 89 (1), pp. 383-388.

Nádasi E., Madarasi, A., Turai E. (2015): Magnetotelluric exploration in the vicinity of Irota and Gadna, Geosciences and Engineering. A Publication of the University of Miskolc 4:6, pp. 105-115. 2015.

Nádasi, E. (2021): The complex geophysical interpretation of the conductivity anomaly near Irota (in Hungarian). Multidisciplinary Sciences A Publication of the University of Miskolc. 11 (1) pp. 98-103, 6 p.

Nádasi, E., Dobos, E., Pecsmány, P., Turai, E (2020).: Ground Penetrating Radar (GPR) soil suitability map of Hungary based on physical and pedological parameters (in Hungarian). Magyar Geofizika 61: 4 pp. 191-198., 8 p.

Nádasi, E., Turai E., Szabó N. P. (2017): Statistical investigation of magnetotelluric data. In: Bodzás, Sándor (szerk.) Műszaki Tudomány az Észak-Kelet Magyarországi Régióban 2017 konferencia előadásai. Debrecen, Magyarország: Debreceni Akadémiai Bizottság Műszaki Szakbizottság (2017) 630 p. pp. 318-324. , 7 p.

Nádasi, E., Turai, E. (2017): Analysis of electromagnetic petrophysical parameters in GPR survey (in Hungarian). Magyar Geofizika, 58/4, pp. 253–258.

Nádasi, E., Turai, E. (2018). Increasing the accuracy of GPR measurements. Geosciences and Engineering: A Publication of the University of Miskolc, 6 (9), pp. 142–150.

Nádasi, E., Turai, E. (2020): The accuracy of depth estimation in GPR surveys. Geosciences and Engineering: A Publication of the University of Miskolc, 8 (13), pp. 108-115. , 8 p.

Nagy, Z. (2003): Aspects of magnetotelluric interpretation in the case of resistivity frequency-dispersion (IP). (In Hungarian) Magyar Geofizika, 44/2, pp. 58-90.

Németh, N. (2012): Geological observation in the Cserehat between Irota and Gadna. Geosciences and Enginnering, 1(1), 261-269.

Newman, G. A., and D. L. Alumbaugh (2000): Three-dimensional magnetotelluric inversion using non-linear conjugate gradients: Geophysical Journal International, 140, 410—424, doi: 10.1046/j.1365-246x.2000.00007.x.

Novák Attila (2010): Elektromágneses geofizikai leképezés tenzor invariánsokkal: a felszínközeltől a dunántúli mélyszerkezetig. Doktori (PhD) Értekezés.

Olhoeft, G. R. (1989): Electrical properties of rocks; in, Physical Properties of Rocks and Minerals, Y. S. Touloukian, W. R. Judd, and R. F. Roy, eds.: New York, New York, Hemisphere Publishing Corporation, p. 257–329.

Pajewski, L., Dérobert, X., Benedetto, A., Giannopoulos, A. (2013): Applications of Ground Penetrating Radar in civil engineering – COST action TU1208. 7th International Workshop on Advanced Ground Penetrating Radar (IWAGPR 2013).

Parker, R. L. (1994): Geophysical Inverse Theory: Princeton University Press.

Percival, J. A., M. Sanborn-Barrie, T. Skulski, G.M. Stott, H. Helmstaedt, and D. J. White (2006): Tectonic evolution of the western Superior Province from NATMAP and Lithoprobe studies: Canadian Journal of Earth Sciences, 43 (7), 1085-1117.

Percival, J., T. Skulski, M. Sanborn-Barrie, G. Stott, A. D. Leclair, T. Corkery, and M. Boily, (2012): Geology and tectonic evolution of the Superior Province, Canada. Chapter 6. In: Percival, J.A., Cook, F.A., Clowes, R.M. (Eds.) The Lithoprobe Perspective: Geological Association of Canada, Special Paper, 49, 512.

Pethő, G. (2009): Theoretical basics for frequency domain EM methods. Lecture notes, University of Miskolc.

Rial F., Pereira M., Lorenzo H., Arias P., Novo A. (2009): Resolution of GPR bowtie antennas: An experimental approach. Journal of Applied Geophysics 67 (4):367-373.

Rodi, W., Mackie, R.L. (2001): Nonlinear conjugate gradients algorithm for 2-D magnetotelluric inversion. Geophysics, 66, 174-187.

Roots. E. and J. A. Craven (2017): 3D modelling of magnetotelluric data from the Abitibi and Pontiac subprovinces of the Superior Province, Ontario and Quebec: Geological Survey of Canada, Open File 8233, 26 p. https:// doi.org/10.4095/300666.

Saintenoy A., Hopmans J. W. (2011): Ground Penetrating Radar: Water Table Detection Sensitivity to Soil Water Retention Properties. IEEE Journal of Selected Topics in Applied Earth Observations and Remote Sensing, IEEE, 2011, 4, pp.748-753.

Sasaki, Y. (2001): Full 3-D inversion of electromagnetic data on PC: Journal of Applied Geophysics, 46, 45—54, doi: 10.1016/S0926-9851(00)00038-0.

Simpson, F., Bahr, K. (2005): Practical Magnetotellurics. University Press, Cambridge.

Sims, W.E., Bostick, F.X., Smith, H.W. (1971): The estimation of magnetotelluric impedance tensor elements from measured data. Geophysics, 36, 938-942.

Siripunvaraporn,W., G. Egbert, Y. Lenbury, and M. Uyeshima (2005): Three-dimensional magnetotelluric inversion: data-space method: Physics of the Earth and Planetary Interiors, 150, 3-14, doi: 10.1016/j.pepi.2004.08.023.

Szalai, I., Braun L., Petrovics I., Schőnvinszky L. és Zalai P. (1987): Észak-Magyarország geofizikai előkutatása – Szendrői-hegység előkutatása, MÁELGI Évi Jel. 1987. pp. 35-39.

Szarka L. and Menvielle M. (1997): Analysis of rotational invariants of the magnetotelluric impedance tensor. Geophysical Journal International 129, 133–142.

Szarka L., Menvielle M. and Spichak V.V. (2000): Imaging properties of apparent resistivities based on rotational invariants of the magnetotelluric impedance tensor. Acta Geodaetica et Geophysica Hungarica 35, 149–175.

Szarka, L. (1990): About relationships among gravity, magnetism and electricity, from point of view of geophysics. (In Hungarian) Magyar Geofizika, 43/2, pp. 74-79.

Takács E. (1957): Geofizikai kutatás tellurikus áramokkal. In: Szurovy Géza (szerk.): A kőolajkutatás és feltárás módszerei Magyarországon. Budapest, Akadémiai Kiadó, 1957. pp. 89–91.

Takács E. (1960): Eljárás tellurikus mérések adatainak feldolgozására a totális változások alapján. Shiyou Diqiu Wuli Kantan (Zhuozhou - China) – Oil geophysical prospecting 5: pp. 20–23.

Takács E. (1968): Anomalous conductivity of the upper crust in the NW foreground of the Bakony mountains. Acta Geod. Geoph. Mont. Hung., 3, 155–160.

Thomas A.M., Metje N., Rogers C.D.F. and Chapman D.N. (2006): Ground Penetrating Radar Interpretation as a Function of Soil Response Complexity in Utility Mapping. Proc. of 11th International Conference on Ground Penetrating Radar, Columbus, Ohio, USA, June 19-22.

Tikhonov, A. N., and V. Y. Arsenin (1977): Solution of ill-posed problems: Winston and Sons.

Tikhonov, A.N. (1950): On determining electrical characteristics of the deep layers of the Earth's crust. Doklady, 73, 295-297.

Trinks, I., Kucera, M., Hinterleitner, A., Löcker, K., Nau, E., Neubauer, W., Zitz, T. (2012): Large-Scale, High-Definition Ground Penetrating Radar Prospection in Archaeology. Geophysical Research Abstracts, vol. 14, p. 13447, EGU General Assembly, April 2012.

Tzanis, A. (2010): matGPR Release 2: A freeware MATLAB® package for the analysis & interpretation of common and single offset GPR data. FastTimes, 15 (1), pp. 17–43.

Varılsüha, D. (2020): 3D inversion of magnetotelluric data by using a hybrid forward-modeling approach and mesh decoupling: Geophysics, 85 (5), E191, doi:10.1190/geo2019-0202.1.

Vozoff, K. (1972): The magnetotelluric method in the exploration of sedimentary basins: Geophysics, 37, 98-141.

Wannamaker, P. E., (2005): Anisotropy versus heterogeneinity in continental solid Earth electromagnetic studies: fundamental response characteristics and implications for physiochemical state. Surveys in Geophysics, 26, 733—765.

Whalen, J. B., J. A. Percival, V.McNicoll, F. J. Longstaffe (2003): Intra-oceanic production of continental crust in a Th-depleted ca. 3.0 Ga arc complex, western Superior Province, Canada: Contributions to Mineralogy and Petrology, 156, 78-99.

Zhdanov, M. S. (2002): Geophysical inverse theory and regularization problems: Elsevier.

Zhdanov, M. S. (2009): Geophysical electromagnetic theory and methods: Elsevier.

Zhdanov, M. S. (2015): Inverse theory and applications in geophysics: Elsevier.

Zhdanov, M.S., L. Wan, A. Gribenko, M. Čuma, K. Key, and S. Constable (2011b): Large-scale 3D inversion of marine magnetotelluric data: Case study from the Gemini prospect, Gulf of Mexico: Geophysics, 76 (1), F77-F87.

Zhdanov, M.S., R. B. Smith, A. Gribenko, M. Čuma, and M. Green, (2011a): Three-dimensional inversion of large-scale EarthScope magnetotelluric data based on the integral equation method: geoelectrical imaging of the Yellowstone conductive mantle plume: Geophysical Research Letters, 38 (8), L08307.

Zhdanov, M.S. (2013): Focusing Controlled Sensitivity of Geophysical Data. Journal of Geology & Geosciences. 02. 10.4172/2329-6755.S10-001.